

AALBORG UNIVERSITY

MASTER THESIS

-Long thesis-

Department of Energy Technology



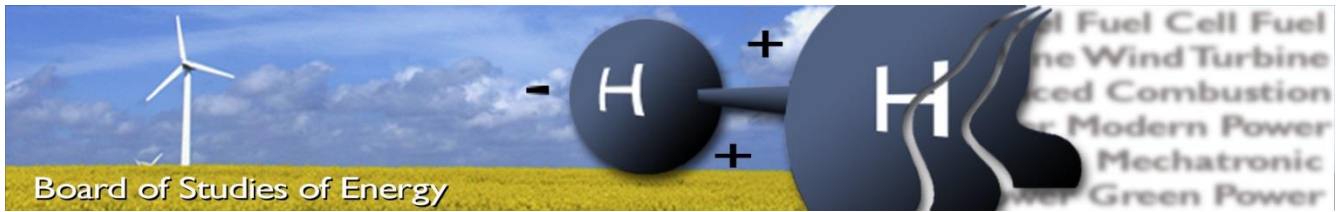
DESIGN AND CONTROL OF HIGH
EFFICIENCY WIND TURBINE BASED
HYDROGEN PRODUCTION SYSTEM

Aalborg University

Department of Energy Technology

Group: WPS3-952

Date: 24 May 2016



Title:	Design and control of high efficiency wind turbine based hydrogen production system
Semester:	9 th and 10 th
Project period:	2 nd September 2015 – 25 th May 2016
ECTS:	50
Supervisor:	Cristian Busca, Frede Blaabjerg
Project group:	Vasile-Simion Sularea

Vasile-Simion Sularea

SYNOPSIS:

In this project a wind powered hydrogen production system is presented. The aim of the presented thesis is to design and study a 250 kW wind powered hydrogen production system and also to design the hardware and control of a power supply for an electrolysis stack at this power.

At first, different types of turbines, generators, converters and electrolysis systems are presented, from which the most efficient are selected for modeling. Furthermore, simulations are performed under different test conditions In order to verify the functionality of the system and the controllers' performance.

In the end, in order to validate the simulations, a small scale prototype for the power electronics conversion stage is built and tested in the laboratory. This includes an AC-DC converter and the designed power supply with the adapted control for the laboratory setup.

Pages, total: [116]
 Appendix: [2]

By accepting the request from the fellow student who uploads the study group's project report in Digital Exam System, you confirm that all group members have participated in the project work, and thereby all members are collectively liable for the contents of the report. Furthermore, all group members confirm that the report does not include plagiarism.

CONTENTS

Nomenclature and Abbreviations	5
Preface	7
Chapter 1. Introduction	8
1.1. Background	8
1.2. System description.....	10
1.3. Objectives	12
1.4. Limitations.....	12
1.5. Outline.....	13
Chapter 2. Overall system analysis.....	14
2.1. Wind turbine and generator types	14
2.2. Converter topologies	16
2.2.1. AC-DC converters	16
2.2.2. DC-DC converters.....	18
2.3. Control strategies.....	19
2.4. Electrolyzer models	21
2.5. Selection of solution.....	24
Chapter 3. System modeling and design.....	25
3.1. Wind turbine modeling	25
3.2. Generator modeling.....	27
3.3. AC/DC converter modeling.....	29
3.4. DC/DC converter model.....	31
3.5. Modeling of Electrolysis system	33
3.6. Design of control for AC/DC converter.....	36
3.7. Design of control of DC/DC converter.....	39
3.8. Design of power electronics for DC/DC converter.....	42
3.9. Diode selection of the rectifier part.....	45
3.10. Transformer design.....	46
3.11. Output filter Inductor design	52
3.12. Summary.....	56
Chapter 4. Simulation results	57
4.1. Overview.....	57
4.2. Generator and field oriented control strategy simulations.....	59

4.3.	Wind turbine – generator – AC-DC converter system simulation	64
4.4.	DC-DC converter simulation.....	67
4.5.	Summary	75
Chapter 5.	Experimental prototype	76
5.1.	Description of experimental setup	76
5.2.	AC/DC converter testing.....	76
5.2.1.	PLL design and testing.....	77
5.2.2.	Current control of the grid connected converter.....	81
5.2.3.	DC voltage and reactive power control.....	93
5.3.	DC/DC converter testing.....	101
5.4.	System experimental results.....	107
5.5.	Summary	109
Chapter 6.	Conclusions and future work.....	110
6.1.	Summary and conclusions	110
6.2.	Future work.....	111
Appendixes.....	112
Appendix A	DC-DC converter test setup	112
Appendix B	AC-DC converter implemented control strategy	113
Bibliography.....	114

NOMENCLATURE AND ABBREVIATIONS

Abbreviations

Alternating current	AC
Back electromotive force	BEMF
Backward Euler	BE
Digital signal processor	DSP
Direct current	DC
Doubly fed induction generator	DFIG
Electrolyzer	EZ
European Wind Energy Association	EWEA
Field oriented control	FOC
Horizontal axis wind turbine	HAWT
Maximum power point tracker	MPPT
Mean length turn	MLT
Permanent magnet synchronous generator	PMSG
Phase locked loop	PLL
Polymer electrolyte membrane	PEM
Proportional-integrator	PI
Pulse width modulation	PWM
Second order generalized integrator	SOGI
Solid oxide electrolysis cell	SOEC
Tip speed ratio	TSR
Vertical axis wind turbine	VAWT
Wind turbine	WT

Symbols

Angular speed	ω
Core induction	B_m
Core window area	W_a
Cross-sectional area	A_c
Current	I
Current density	J
Density	ρ
Duty-cycle	D
Efficiency	η
Moment of inertia	J
Number of turns	N
Pole pairs number	p
Rated power of wind turbine	P_{wn}
Rotor flux linkage	λ_{PM}
Skin depth	ε
Tip speed ratio	λ

Torque	T
Transformer ratio	n
Transformer utilization factor	K_u
Transformer voltage regulation	α
Voltage	V
Wind speed	v
Wind turbine blade pitch angle	β
Wind turbine blade radius	R
Wind turbine power coefficient	C_P

Subscripts

Capacitor	cap
Copper	cu
Electrical	el
Input	in
Mechanical	m
Natural frame	a,b,c
Output	o
Primary	p
Rotational frame	d,q
Secondary	S
Stationary frame	α,β
Stator	s
Switching	sw
Wire	w

Preface

The present report entitled “Design and control of high efficiency wind turbine based hydrogen production system” is prepared by Vasile-Simion Sularea, student in 4th Semester, at Wind Power Systems as long master thesis. In the project the main idea is to model and analyze the behavior of a wind powered hydrogen production system and to design a 250 kW power supply for an electrolysis system as part of the Power-to-Electrolyzer project between Aalborg University and Green Hydrogen in order to be able to produce hydrogen from wind power in an efficient manner.

The report is divided into six chapters, consisting in Introduction, Overall system analysis, System modeling and design, Simulation results, Experimental prototype and Conclusions and future work. There is also an appendix where part of the built converter is presented and the control strategy block diagram for the other. For modeling and simulation PLECS was used, whereas for practical implementation two DSPs from Texas instruments were used.

The project duration was approx. 9 months. I would like to thank my supervisors, Frede Blaabjerg and Cristian Busca for all their support in helping me with the problems that I confronted all this time.

The author

CHAPTER 1. INTRODUCTION

1.1.BACKGROUND

Given the climate and environmental problems in respect to the CO₂ emissions due to the fossil fuels usage, the European Union decided in 2014 that until 2030 more than a quarter (27%) of the final energy consumption must come from renewable energy sources. According to European Commission, this target can be achieved if 46-49% of the electricity is produced by renewables. In this case, wind is supposed to have 21% of the electricity generation [1].

According to European Wind Energy Association (EWEA) the annual wind power installations is on a continuous rise, having 11.79 GW installed in 2014, compared with the 3.21 GW installed in 2000. The 2000-2014 evolution in annual installations can be seen in Figure 1 [2].

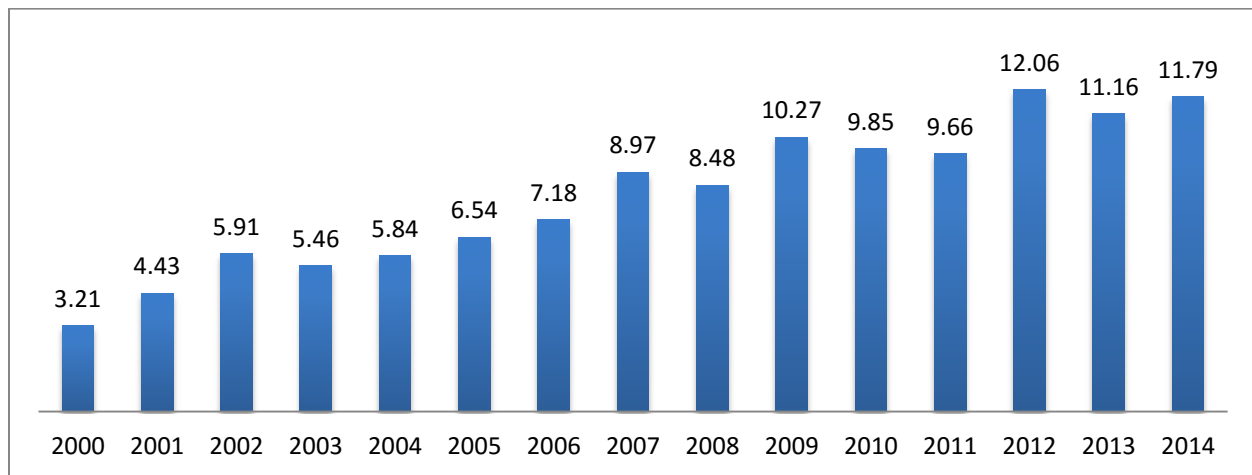


FIGURE 1: ANNUAL WIND POWER INSTALLATIONS IN EU (GW) [2]

Due to the fluctuating character of the energy produced from wind or solar power it is necessary to use a storage system. Having larger wind power systems installed implies large scale energy storage systems. The major industrialized countries use pumped hydropower as a storage system, but this is not available in most geographical areas. An alternative could be storage of compressed air or converted to hydrogen [3].

For hydrogen production multiple technologies can be used, including coal gasification, partial oxidation of natural gas or steam reforming, but these generate greenhouse gases and they are dependent on fossil fuels. The most common way with no environmental repercussions is water electrolysis, because besides heat, the only byproduct in this process is water. This technology has also the advantage that the hydrogen has a high purity [4].

Generating hydrogen from renewable energies is a clean way also to store energy in order to reduce the fluctuations in power production caused by wind speed variation. When the wind is generating more energy than there is consumed, this is transformed into hydrogen and when the energy demand is greater than the wind produced energy, the hydrogen can be converted back into electricity using fuel cells.

The actual wind turbine powered electrolysis systems may be divided into 2 major categories: grid connected [5] (Figure 2) and stand-alone [6] (Figure 3). There are also variations of the presented layouts including DC loads and fuel cells, but they are not presented here due to the focus of the project being on the hydrogen production system.

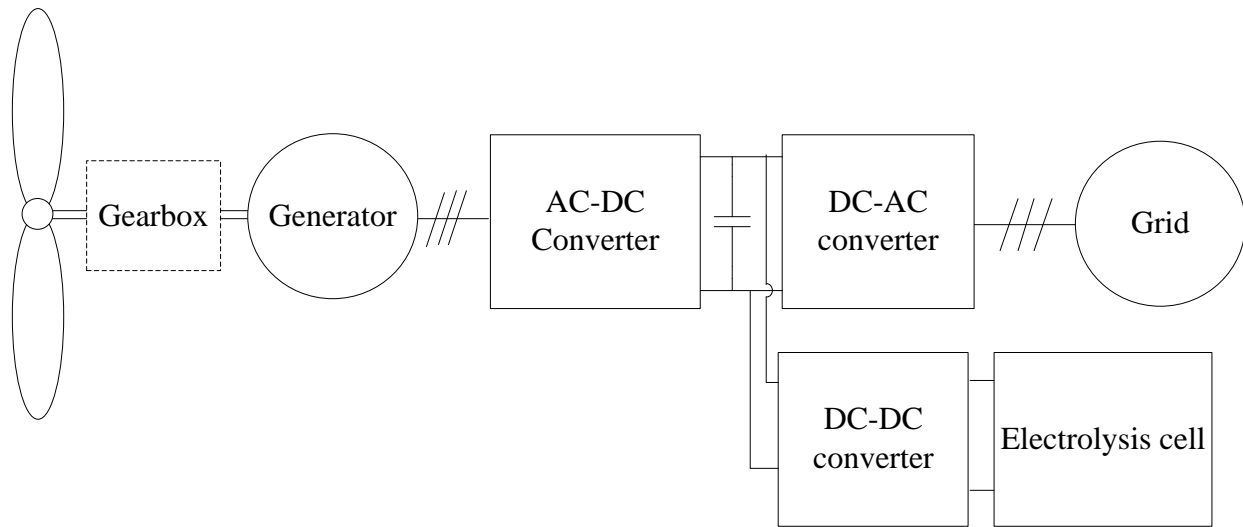


FIGURE 2: GRID CONNECTED WIND TURBINE POWERED ELECTROLYSIS SYSTEM

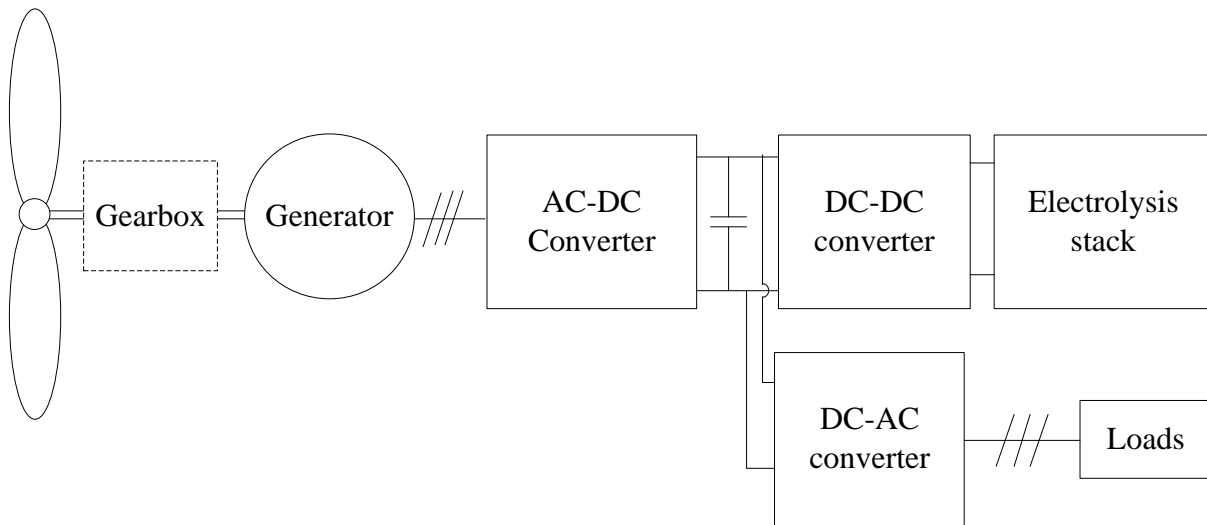


FIGURE 3: STAND ALONE WIND TURBINE POWERED ELECTROLYSIS SYSTEM

In the case where the grid connection is not available, the produced energy is consumed by the loads and all the rest is transformed into hydrogen. The hydrogen can then be reconverted into electrical energy using a fuel cell in periods with low wind or maintenance of the turbine [6].

For the grid connected topology the energy produced by the wind turbine is divided between the grid and the electrolysis cell. Depending on the mode of operation of the system, the main task can be to feed into the grid a desired amount of power and the rest can be transformed into hydrogen as a storage solution, or it can be that a specific amount of hydrogen is desired to be made and the rest of the energy is fed into the grid [5]. This type of system can also generate hydrogen when there is no wind by taking energy from the grid and based on the control strategy adopted it can also control the reactive power flow into the grid.

The variety of wind turbines, generators, converters and electrolysis systems will be presented in the subsequent chapter, where the most used ones are presented in more detail.

This thesis will explore such a system, analyzing the behavior under different circumstances, with the main focus on the power electronics stages. This includes designing the control for the AC-DC converter and designing the power electronics and control for a DC-DC converter.

1.2. SYSTEM DESCRIPTION

The overall project idea is to design a high efficiency hydrogen production system based on wind power generation. In order to achieve this it is needed to model and simulate the whole wind turbine generation system and to design the power source for the electrolysis system. Because the main focus is on the power electronics side, this part will be modelled in more detail, and for the rest simplified models are used. The proposed system for simulations is composed of a wind turbine, a two stage power electronics interface and an electrolysis system, as it is presented in Figure 4.

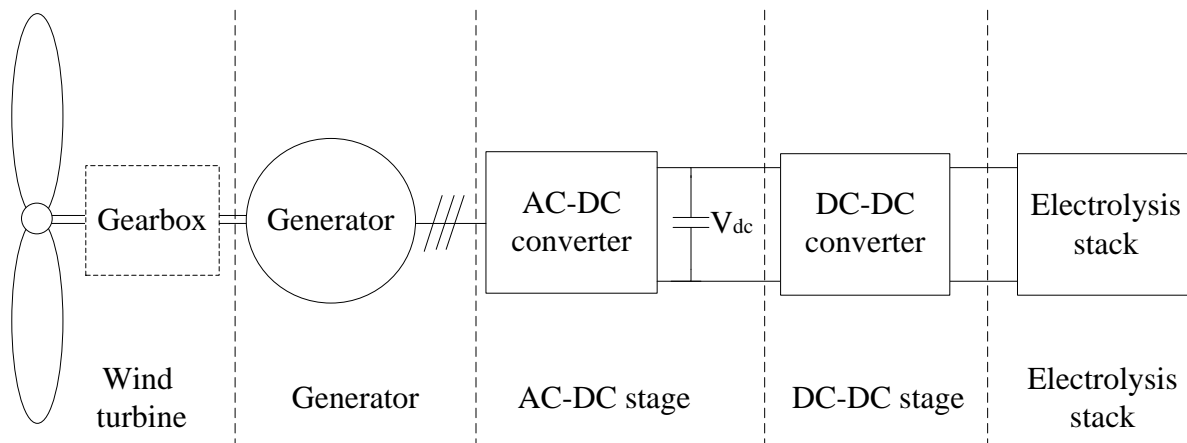


FIGURE 4: SYSTEM OVERVIEW FOR WIND POWER TO HYDROGEN CONVERSION

The wind turbine is used to transform the wind energy into the electrical energy through the blades and generator. The gearbox is used to increase the rotational speed of the generator in order to be able to reduce the number of its pole pairs.

Connected with the generator is an AC-DC converter which works as a voltage rectifier. It controls the generator rotational speed by managing the amount of power transmitted to the DC link and in this way ensuring an optimal power coefficient by changing the rotational speed of the shaft.

A DC-DC converter has the role of taking the energy from the DC link and controls the current through the electrolysis stack. This current is dependent of the energy produced by the generator. The topology chosen for the converter could also provide a galvanic isolation through a transformer.

The electrolysis cell generates hydrogen proportional with the current absorbed, based on the Faraday’s law [7].

Depending on the system layout multiple types of wind turbines, generators, converters and electrolysis cells can be used, each one having its own advantages and disadvantages considering factors as initial cost, efficiency, maintenance, reliability and functionality. These options are presented in the following chapter and an optimum is chosen for the presented system.

In order to verify the design of the system, a small scale prototype is built in the laboratory. For the prototype testing, the system presented in Figure 5 is used, where the wind turbine – generator system is replaced by the grid. In this way the controller design, the power electronics and magnetics design can be evaluated.

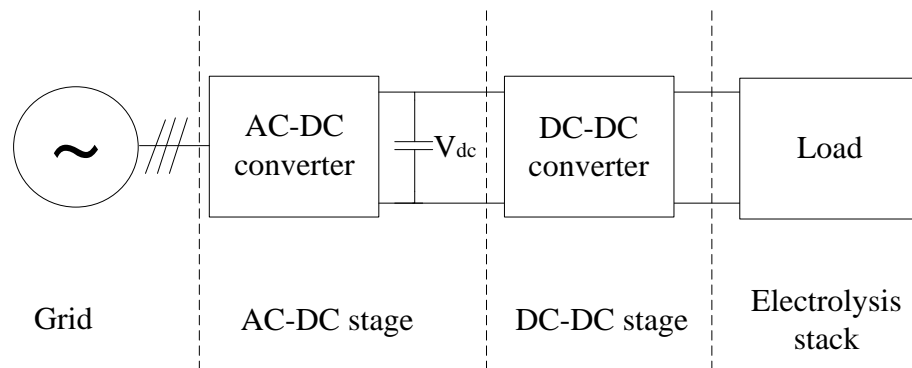


FIGURE 5: SYSTEM PROPOSED FOR PROTOTYPE TESTING IN ORDER TO VERIFY THE SYSTEM DESIGN

1.3. OBJECTIVES

The objective of this project is to design a 250 kW wind turbine powered electrolysis system with a high efficiency and analyze its performance under various conditions. This involves selection of system topologies, modeling of the whole system from the wind turbine to the power electronic components and control strategies in order to verify the functionality under different cases. This includes designing the control strategies for both AC-DC and DC-DC converters and designing a 250 kW power supply for an electrolysis system which should be able to be operated with a grid connected AC-DC converter. The AC-DC current controllers' specifications are: a response time of maximum 5 *ms* and an overshoot of maximum 10%; the speed controller: a response time of maximum 5 *s* and an overshoot of maximum 20%; the DC-link Voltage controller: a response time of maximum 80 *ms* and an overshoot of maximum 10%; for the DC-DC current controllers response time should be less than 5 *ms* with an overshoot of less than 10%.

In order to validate the simulation results and the power electronics converter design a small scale (10 kW) test stand will be built including an AC-DC and a DC-DC converter. The AC-DC current controllers' specifications are the same as presented before, with the only modification that instead of the speed controller a reactive power controller will be introduced with a desired response time of maximum 80 *ms* and an overshoot of maximum 20%.

1.4. LIMITATIONS

The modeling of the wind turbine (mechanical part and generator) and electrolysis system is simplified and because of this some of the transients may be overlooked. This is due to the fact that the main focus is on the designing of the DC-DC converter prototype and the AC/DC converter control.

The electrolysis system model does not take into account the temperature and pressure of the stack, which affects the quantity of hydrogen generated and the voltage of the stack. This simplification will result in a difference between the quantity of hydrogen calculated and the one which would have been produced in the same conditions.

For testing purposes, the AC-DC converter is connected to the grid due to the absence of the physical wind turbine. Because of this, the variation of input power caused by the change in the wind speed can only be observed in simulation. Also due to the power restrictions in the laboratory, the maximum test power is 10 kW.

1.5. OUTLINE

The work reported in this thesis is divided into 6 chapters, presenting a step by step approach of modeling and validating the model of the system.

In Chapter 2 the state of the art regarding the system components is presented, discussing the major types of wind turbines, most used types of generators, converter topologies and electrolysis system models.

In Chapter 3 modeling of the system is presented taking into consideration all the components. For the wind turbine and generator simplified models are used and for the power electronics side more complex modeling is employed, including thermal behavior for the DC-DC stage. Also power electronics design for the DC-DC converter and controllers design is performed in this chapter.

The results of the simulations are discussed in Chapter 4, which presents different test cases for system operation. These ones will show the response of the system under change in wind speed, change in load and step responses for the controllers designed.

Chapter 5 describes the experimental part, verifying and validating the models developed in the previous chapter. The two converters are tested separately and also as a system. The tests include testing of the current controllers, power controllers, phase locked loop system and also the functionality of the system.

In Chapter 6 the conclusions are presented and also future work regarding the project.

CHAPTER 2. OVERALL SYSTEM ANALYSIS

2.1.WIND TURBINE AND GENERATOR TYPES

The structure of a wind energy conversion system, as shown in Figure 6, includes a turbine, a gearbox (in some of the structures the gearbox is not needed) and an electrical generator.

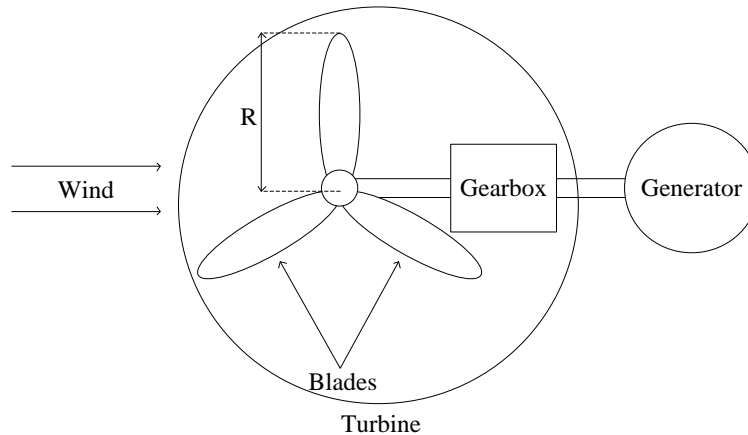


FIGURE 6: WIND ENERGY CONVERSION SYSTEM COMPOSED FROM WIND TURBINE, GEARBOX AND GENERATOR [8]

The Wind Turbine (WT) can have two different construction types depending on the direction of the axis: Horizontal Axis Wind Turbine (HAWT), Figure 7 (a) and Vertical Axis Wind Turbine (VAWT) Figure 7 (b) and (c). The most used is the HAWT due to the high efficiency and low cost/power ratio. The largest disadvantage of this structure is that it has to be mounted on a tower, making the design more complex and increase the maintenance cost. For the VAWT the maintenance is easier and it also has the advantage that it can receive wind from any direction. This one has the disadvantage that is not self-starting, requiring the generator to rotate the wind turbine at start, and also the aerodynamic torque has a lower and a more oscillatory component [8].

The power taken from the wind is transformed into a shaft rotation, being a mechanical torque. The mechanical gearbox is the interface between the electric generator rotor and the wind turbine shaft with the role of changing the rotational speed of the blades to the speed of the generator. In direct drive systems a gearbox is not used and the turbine shaft is connected directly to the rotor of the generator. It is a case in which a generator with a high number of pole pairs is necessary [8].

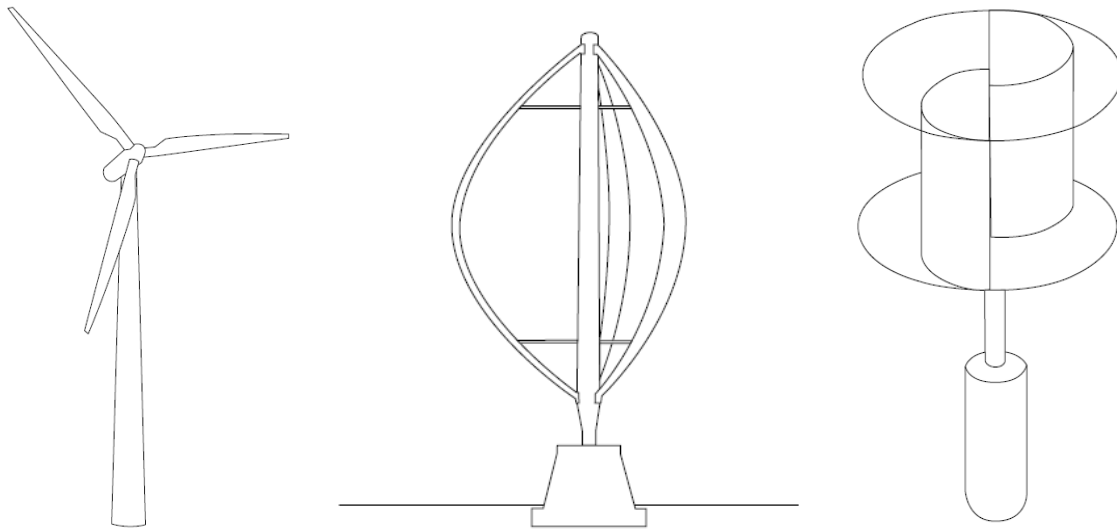


FIGURE 7: (A) HORIZONTAL AXIS WIND TURBINE (B) VERTICAL AXIS WIND TURBINE (DARIUS) (C) VERTICAL AXIS WIND TURBINE (SAVONIUS) [8]

To quantify the energy taken from the wind and transformed into electricity the power coefficient of the wind turbine is defined. This one is dependent on the wind turbine axis and it can be defined in terms of axial induction factor or in terms of Tip Speed Ratio (TSR) and the pitch angle β . Knowing the power coefficient and the power generated by the wind, the output power of the turbine can be expressed [8].

Developed for the generator side, there exist many options, depending on the wind turbine concept. For the first wind turbines, induction generators directly connected to the grid were used, the turbines having a fixed-speed controlled by pitch angle of the blades. For the newer grid connected wind turbines, two major types of machines are used: Permanent Magnet Synchronous Generator (PMSG, Figure 8) and Doubly Fed Induction Generator (DFIG) [8].

In the case of DFIG, the operation principle is the same as for a synchronous motor, with the difference that the synchronous speed can be varied by modifying the AC currents frequency, which are fed into the rotor windings and the stator is connected directly to the grid. The advantage of this topology is that the converter needs to transfer only a part of the generated energy and thus having the converter rating power smaller than the generator, but it has to be connected to the grid. For the PMSG a full scale converter is needed in order to transfer the energy from the wind turbine to the grid or the converter connected to the DC link. This can be unidirectional (diode rectifier + inverter) or bidirectional (full scale converter) [8].

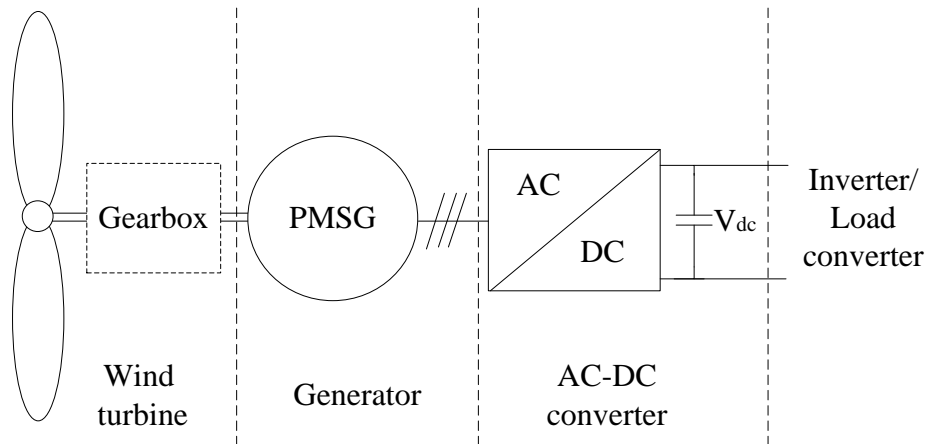


FIGURE 8: PERMANENT MAGNET SYNCHRONOUS GENERATOR CONFIGURATION FOR WIND TURBINE APPLICATIONS

There are also other types of generators to be used (switched reluctance generator, synchronous generator with external field excitation, dual stator winding machine, etc.) but they are not discussed due to the fact that the main focus is on the power electronics part of the overall system [8].

2.2.CONVERTER TOPOLOGIES

The power electronics part can be separated in to two different stages: AC-DC and DC-DC, and each one require a different converter topology for a different functionality. The AC-DC converter has to transform the AC voltage generated by the WT to DC voltage. Due to the low voltage drop on one electrolysis cell, usually the voltage has to be reduced, operation for which the DC-DC converter is used. The most used topologies are presented as in the next paragraphs.

2.2.1. AC-DC CONVERTERS

The cheap solutions for AC to DC conversion of energy are unidirectional power converters (Figure 9), two level power converters (Figure 10) or multilevel power converters. The simplest and the same time the cheapest one is the unidirectional power converter, which consists in a three phase diode rectifier. The main disadvantage is that it is not able to provide reactive or active power flow control and also the output voltage has a low frequency ripple. In order to reduce this ripple and achieve stable DC voltage even in various wind speed conditions a boost converter would be needed to be cascaded with the rectifier. Also the diode rectifiers introduce pulsations with low frequency due to the harmonics which can cause shaft resonance [9].

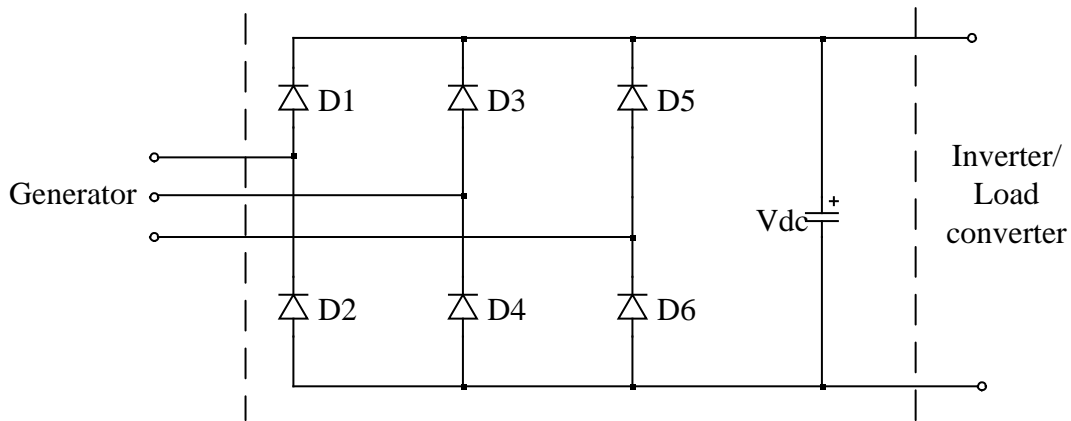


FIGURE 9: DIODE RECTIFIER USED FOR AC TO DC CONVERSION

The drawbacks of the diode rectifier are not present in the two level power converters based on transistors. These ones are able to control the active/reactive power flow from the wind turbine, maintain a steady DC link voltage and the low frequency harmonics present in the diode rectifier will be cancelled in this case. The two-level PWM voltage source converter from Figure 10 is the most used three phase topology in wind power systems, due to the fact that the technology is well-established, the structure is relatively simple with a few components, contributing to a robust and reliable design. A disadvantage of the topology would be that for high power levels of MW range the switching losses may increase in a way that a different topology would have to be used, like Multi-Modular Converters (MMC) or multiple interleaved two level voltage source converters. In this way the stress on the switching devices is distributed on multiple devices. For the available switching devices, in order to achieve the desired power levels, they will need to be placed in parallel or series connections which would reduce the simplicity and robustness of the system [9].

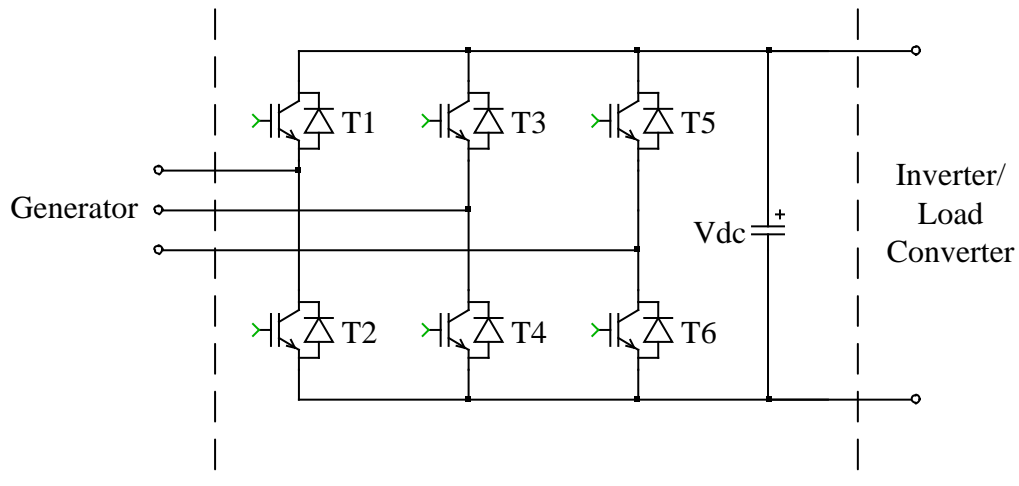


FIGURE 10: ACTIVE RECTIFIER TO BE USED IN MODELING AND SIMULATION

2.2.2. DC-DC CONVERTERS

The output of the AC-DC side has to have a value of at least the peak of the generator line to line voltage in order to be able to control the generator currents. Due to the low voltage drop over an electrolysis cell, although multiple cells are used in series, the DC voltage is too large to be used directly. Due to this, a DC-DC converter is used in order to be able to control the current through the electrolysis cell by varying the voltage across the system. Two basic topologies are available for this purpose based on the property of providing or not providing galvanic isolation: transformer-less or having galvanic isolation. If a galvanic isolation is required the most used topology is the full bridge with a diode rectifier, which can have multiple topologies depending on the system [10] and if there is no need for isolation then a buck converter can be used [11].

For a transformer-less configuration, a simple buck is acceptable at low power, but with the increase in power a solution would be an interleaved buck converter, as shown in Figure 11 [12]. In this way the power rating of the switching devices decreases and the current ripple is smaller. The control of such a converter is relatively simple, by being just a modified version of the simple buck control strategy. For this topology it is also a problem reducing the voltage with a large ratio, so for a large ratio between the input and output voltage a transformer isolated topology is desired [10].

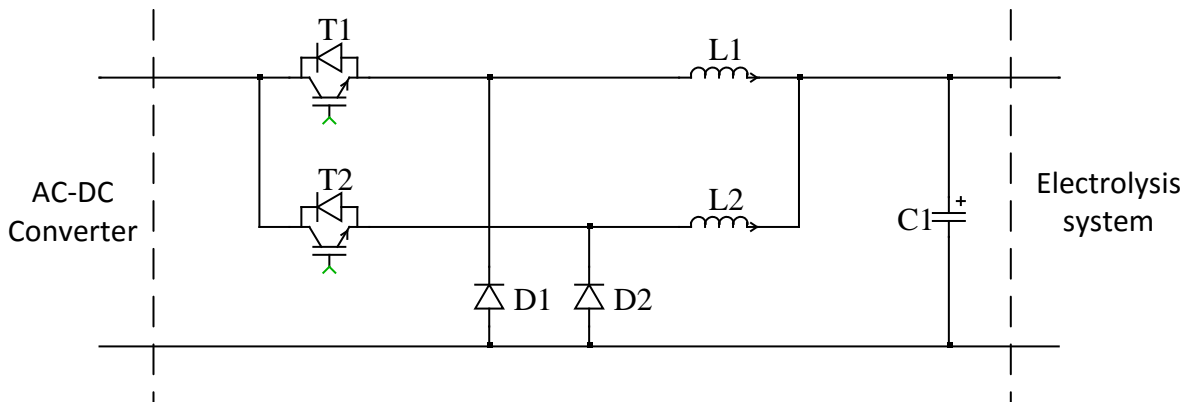


FIGURE 11: INTERLEAVED BUCK WITH 2 PHASES USED FOR STEPPING DOWN THE VOLTAGE

For the galvanic isolated topology, at small powers up to a few kW, flyback and forward converters can be used [13]. But as the power increases, full bridge converters are used in order to convert the DC voltage into a high frequency AC voltage, which is passed through a high frequency transformer in order to reduce size. A diode rectifier, as shown in Figure 12, is afterwards used in order to transform the voltage back into DC. The rectifier is composed of two diodes if the transformer secondary winding has a center tap or it is composed of 4 diodes if the transformer secondary winding does not have a center tap [14].

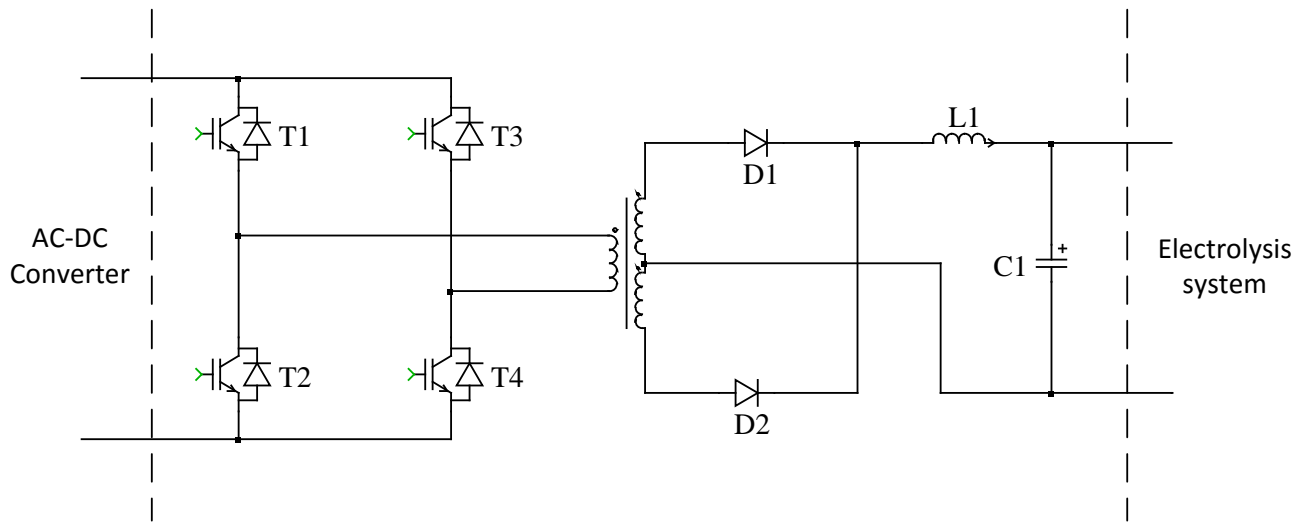


FIGURE 12: FULL BRIDGE GALVANIC ISOLATED CONVERTER USED FOR STEPPING DOWN THE VOLTAGE

For high power ratings more interleaved full bridge converters are used in order to reduce the stress on the switches. This will also increase the frequency of the pulses on the output filter, leading to a further reduction of its size.

2.3. CONTROL STRATEGIES

In order to be able to extract maximum power for the topology presented in Figure 13 from the wind turbine, the generator torque has to be controlled to ensure an optimum rotational speed of the blades. Due to this, one of the converter stages will have as power reference the optimum power given by the wind turbine Maximum Power Point Tracker (MPPT). To ensure a constant DC-link voltage, the other converter has to transfer the same amount of power as the first one. This results in two possible cases, either the AC-DC converter's power reference is given by the MPPT, with the DC-DC converter working with DC-link voltage control having the sole purpose of transferring the input power, or vice versa, case in which the DC-DC converter has the power reference set by the MPPT and the AC-DC just controls the wind generator currents to ensure a constant DC-link [15].

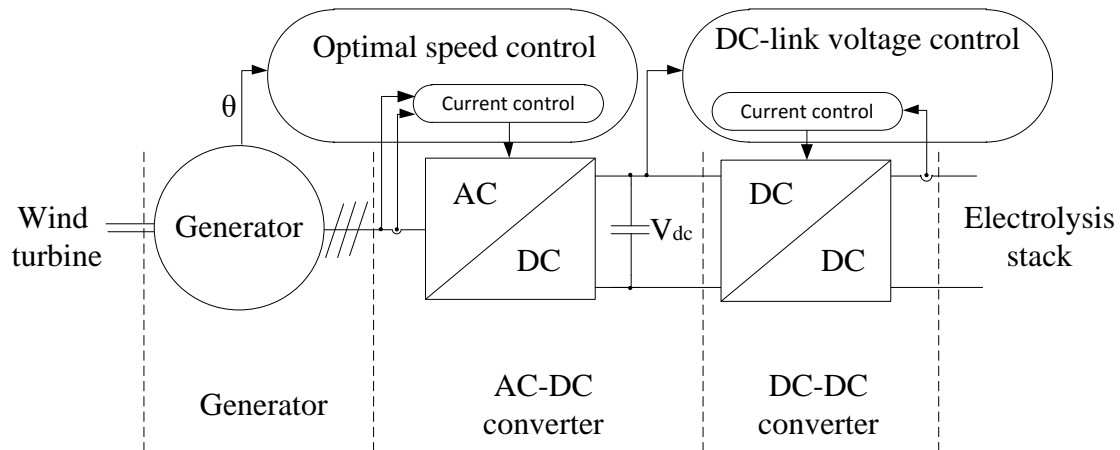


FIGURE 13: OVERALL CONTROL STRATEGY DIAGRAM FOR A WIND TURBINE POWERED ELECTROLYSIS SYSTEM

Depending on the hardware configuration, two major control strategies are used for the AC-DC converter. In the case where the generator is connected with a rectifier bridge and a boost converter, the generator control is ensured by the boost converter current. The disadvantage is that the phase of the current with respect to the generator electromotive force cannot be controlled and also it is not possible to control the harmonics in the current. Due to this fact filters are used for 5th and 7th harmonics on the generator side. For the case when the converter is fully controllable, usually a Field Oriented Control (FOC) strategy is employed, as shown in Figure 14. In this way the phase of the current can be controlled and also the current harmonics compensation can be achieved [16].

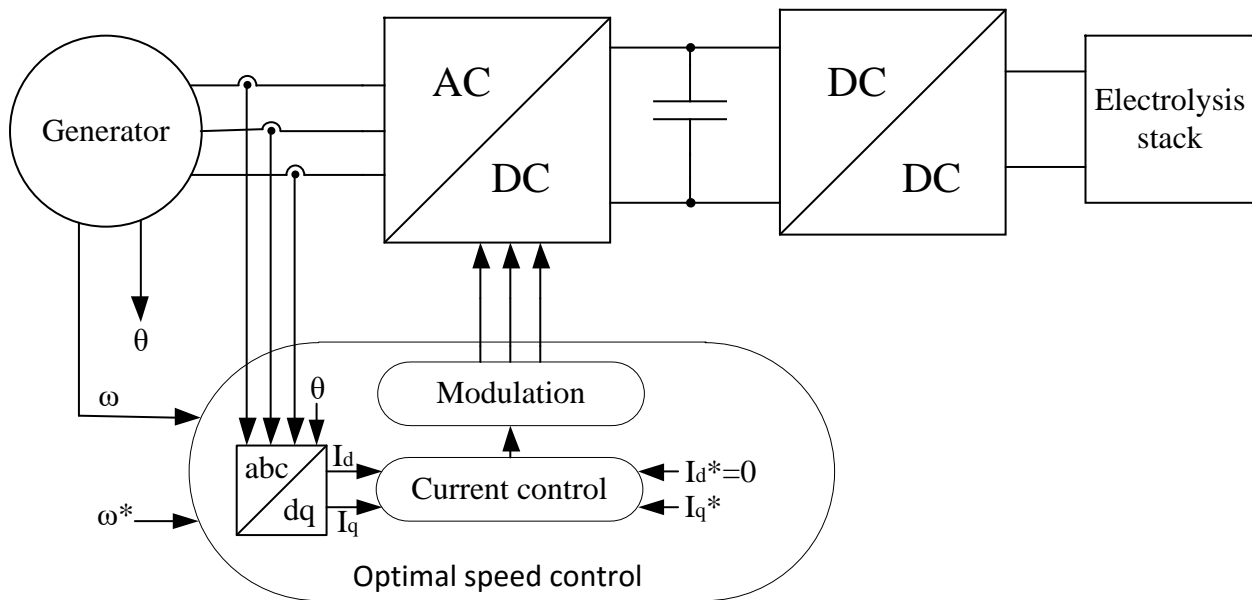


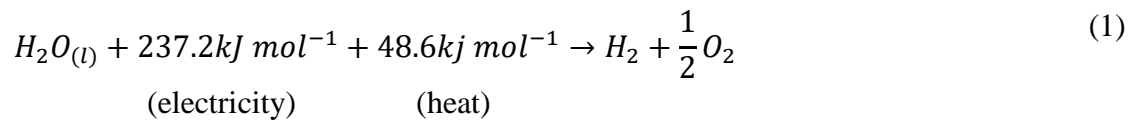
FIGURE 14: FIELD ORIENTED CONTROL FOR GENERATOR SIDE CONVERTER

In the proposed control scheme the both I_d and I_q current components can be controlled independently, each one being controlled through a PI regulator. The I_d reference is set to zero in order to maximize the torque generated by the generator and I_q reference is given by the speed controller [16].

For the DC-DC converter a simple current control is used with a PI regulator in order to ensure zero steady state error. The reference for the current is given by an outer loop, which can be DC voltage or the power control loop, depending on the chosen control strategy.

2.4. ELECTROLYZER MODELS

Due to the fact that hydrogen does not exist in nature in its molecular form, it can be only produced by means of new energy input, and the most used methods to date are by steam reforming of natural gas or other fossil fuels [17]. In this method water vapors at approximately 700-1000 °C are reacted with a fossil fuel in the presence of a catalyst (commonly nickel) in a reformer. The purity of the produced hydrogen in this case is usually low, the gas having in composition a high composition of carbonaceous species, and one of them being carbon monoxide. Another bigger disadvantage is that the method is still depending on fossil fuels. High purity hydrogen can be created by electrolysis, the electrochemical process of water conversion to the two composing elements, hydrogen and oxygen [18]. The reaction is presented in (1).



Although the electrolysis phenomenon was discovered in 1789 (by Troostwijk and Diemann), the production of hydrogen based on this method was hindered by the price of electricity. This has changed due to the need of storing energy where hydrogen is a suitable option. The three most common methods for hydrogen production are alkaline water electrolysis, solid oxide electrolysis (SOEC) and polymer electrolyte membrane electrolysis [18].

The most mature technology is the alkaline water electrolysis and, at the commercial level, is the most extended electrolytic technology worldwide. The simplified process is presented in Figure 15(a) and it is based on two electrodes immersed in a caustic potash solution (alkaline electrolyte) with a 20-30% Potassium hydroxide (KOH) level. The diaphragm separates the two electrodes and separates the two resulting gases for safety and efficiency reasons. An advantage of this technology is that it can achieve megawatt power range and the cost is relatively low compared with the others. But it has also three important drawbacks: low partial load range, limited current density and low operating pressure, which makes the stack design configuration bulky [18].

The solid oxide electrolysis system was first used in the 1980s. After Donitz and Erdle, who were the first to report results, this topology became of great interest. SOECs convert the electrical energy into chemical energy directly, and having a high efficiency in hydrogen production, 100% of Faraday efficiency is achievable at voltages as low as 1.07 V. Now, the SOEC is currently under development and the research has increased in the last decade. Due to the operating principle and conditions, the SOEC can be used also for electrolysis of CO₂ in CO and co-electrolysis of H₂O/CO₂ to H₂/CO (syngas). If the issues with the durability of ceramic materials at high temperatures and long term utilization are solved, the SOEC can become a solution for mass production of hydrogen [18].

In order to overcome the disadvantages of alkaline electrolysis systems General Electric developed the first water electrolysis system concept based on a solid polymer electrolyte in the 1960s, also known as Proton Exchange Membrane or Polymer Electrolyte Membrane (PEM) water electrolysis. The PEM has low gas crossover, a compact system and design, a high proton conductivity and high pressure operation. They can work with a much higher current density compared to the alkaline electrolysis reducing the operational cost, the maximum current density being limited by the ohmic losses. The PEM can work under a wide range of input power do to the low gas crossover rate (this providing high purity hydrogen). The solid electrolyte will make it possible to go to high pressures, up to 350 bar, and because the hydrogen is at high pressure requires less energy to further compress it for storage purposes. High pressure, although it has advantages, comes with a cost and it requires thicker membranes in order to avoid a cross-permeation phenomenon, and thicker membranes mean higher resistive losses.

Due to the corrosive acidic regime, the PEM requires materials to resist to low pH conditions and sustain high voltage (~2 V) applied over them at high current densities. These properties are found as noble catalysts (platinum group metals) which are expensive and rare, and titanium based current collectors and separator plates as shown in Figure 15 (b). The number of papers related to PEM is low, but there is still research done in order to overcome the use of scarce elements [18]. A characteristic of a PEM electrolysis cell at a temperature of 80 degrees Celsius provided by Green Hydrogen is presented in Figure 16.

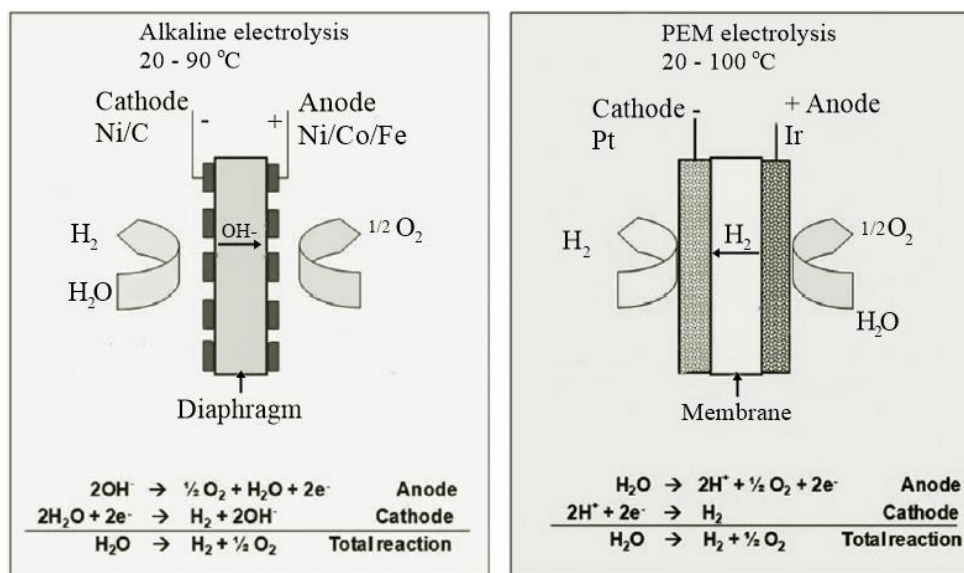


FIGURE 15: ELECTROLYSIS PROCESS FOR TWO DIFFERENT ELECTROLYSIS SYSTEMS: ALKALINE ELECTROLYSIS (A). PEM ELECTROLYSIS (B) [18]

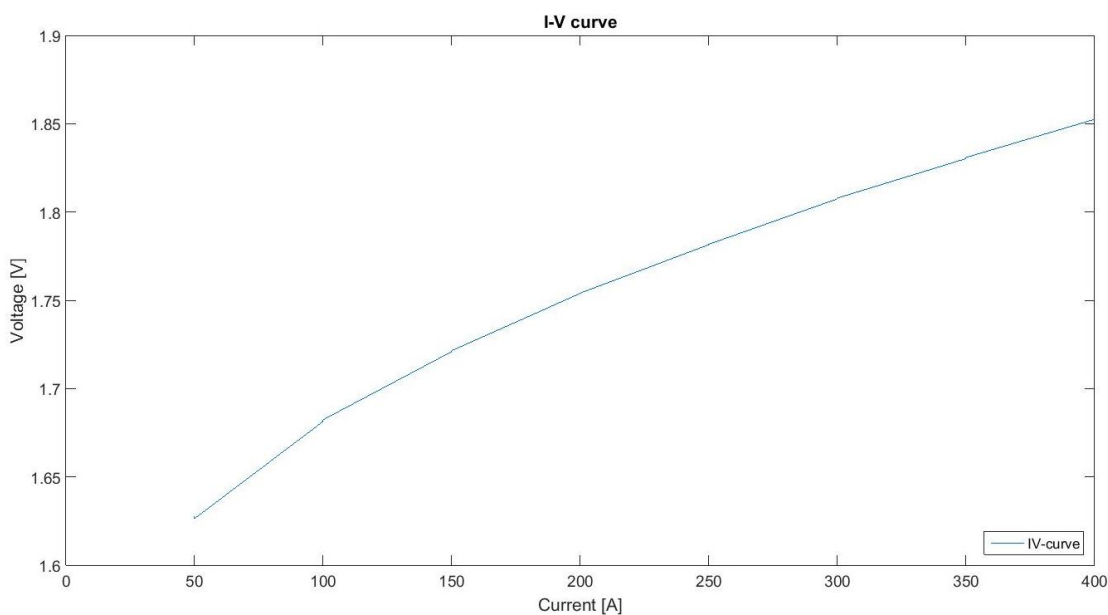


FIGURE 16: POLYMER ELECTROLYTE MEMBRANE CURRENT VS VOLTAGE CHARACTERISTIC AT 80 DEGREES CELSIUS

2.5. SELECTION OF SOLUTION

Due to a large diversity of options for modeling different parts of the system, a selection of topologies was made based on various factors.

For the wind turbine type, a horizontal wind turbine with PMSG was chosen to be modelled because is the most used one at the moment. It has a higher efficiency compared with the vertical axis turbine and it is self-starting. A direct drive system is used in order to avoid using a mechanical gearbox, which would include a higher maintenance cost and would also lower the reliability of the system. As for the generator, the PMSG is chosen due to its high efficiency and reliability.

In the case of the AC-DC converter, a two level active rectifier is used in order to be able to fully control the currents through the generator, providing a steady DC voltage at the output.

For the DC-DC converter topology both were chosen to be modeled in order to establish which one would perform better. Based on initial simulations one of the topologies will be used also for thermal modeling of the switching devices.

As for the overall control strategy, the AC-DC converter is chosen to control the speed of the wind turbine by controlling the currents in the generator and the DC-DC converter to control the DC-link voltage and thus feeding to the load all the power given by the wind turbine.

For the electrolysis system, a PEM electrolysis system was modeled due to the fact that a I-V curve for a PEM system was known from experimental results.

As mentioned, for the WT and the electrolyzer, simplified models are used as the main focus is on the power electronics converters and their control.

CHAPTER 3. SYSTEM MODELING AND DESIGN

In order to study the behavior and design the system shown in Figure 17 as a single unit, all the components have to be modeled for simulation purposes. This includes modeling of the wind turbine, generator, power electronic energy conversion stages and electrolysis system. In this chapter the modeling of the components and design of the control strategy is presented, starting from the generation part to the load.

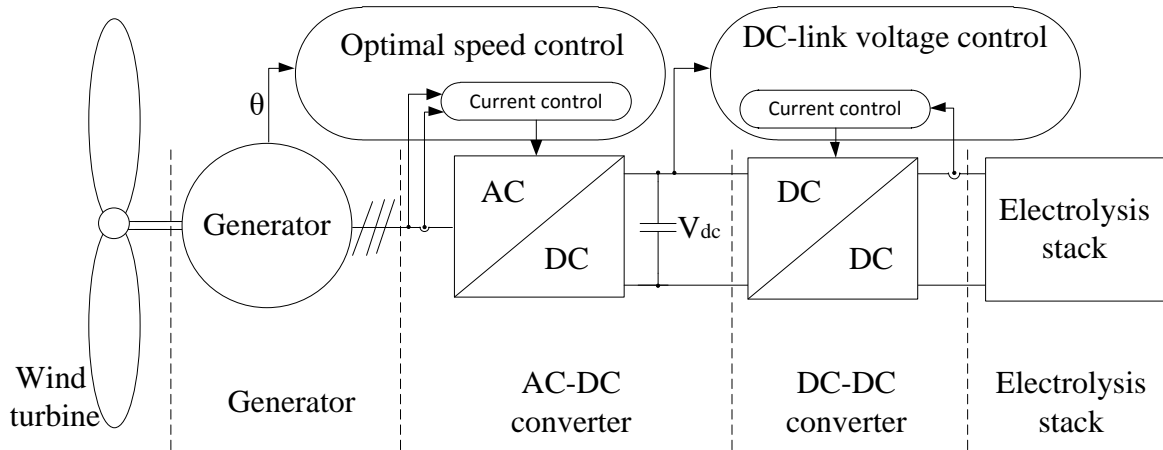


FIGURE 17: SYSTEM TO BE MODELLED OVERVIEW, INCLUDING THE CONTROL STRATEGY

After the modeling and control part, the design of the power electronics for the DC-DC converter and magnetic components are presented.

3.1. WIND TURBINE MODELING

The parameters for the modeled wind turbine are presented in Table 1, which were taken from [6]:

TABLE 1: MODELED WIND TURBINE PARAMETERS

Rated power P_{wn}	250 [kW]
Rated rotational speed	23.33 [rpm]
Rated wind speed	12.205 [m/s]
Radius of wind turbine R	36 [m]
Maximum power coefficient C_{pmax}	0.441

The model for the horizontal axis wind turbine can be expressed by equations (2),(3) and (4) [6].

$$P_w = \frac{1}{2} C_p(\beta, \lambda) \rho v^3 \pi R^2 \quad (2)$$

$$C_p(\beta, \lambda) = c_1 \left(\frac{c_2}{\lambda_i} - c_3 \beta c_5 - c_6 \right) \exp\left(-\frac{c_7}{\lambda_i}\right) \quad (3)$$

$$\lambda = \frac{\omega R}{v} \quad , \quad \frac{1}{\lambda_i} = \frac{1}{\lambda + c_8 \beta} - \frac{c_9}{\beta^3 + 1} \quad (4)$$

Where P_w is the produced power by the wind turbine [W], β is the blade pitch angle [degrees], λ is the tip speed ratio, ρ is the air density (considered as $1.225[kg/m^3]$), v is the wind speed, R is the rotor blade radius [m] and $c_1 - c_9$ are constants of this wind turbine ($c_1 = 0.091$, $c_2 = 151$, $c_3 = 0.58$, $c_4 = 0.002$, $c_5 = 2.14$, $c_6 = 13.2$, $c_7 = 18.4$, $c_8 = -0.02$ and $c_9 = -0.003$) [6].

In order to achieve maximum efficiency below rated power, the angular speed of the turbine must be controlled to obtain the maximum power coefficient corresponding to the wind speed. As it can be observed in Figure 18, the optimum angular speed varies according to the wind speed. Due to the fact that wind speed is difficult to measure accurately, usually, the MPPT operation is done without measuring the wind speed, just based on the angular speed and the optimal value of λ , like is presented in (5) [6].

$$P_{MPPT} = \frac{1}{2} C_{p_max} \rho \left(\frac{\omega R}{\lambda_{opt}} \right)^3 \pi R^2 \quad (5)$$

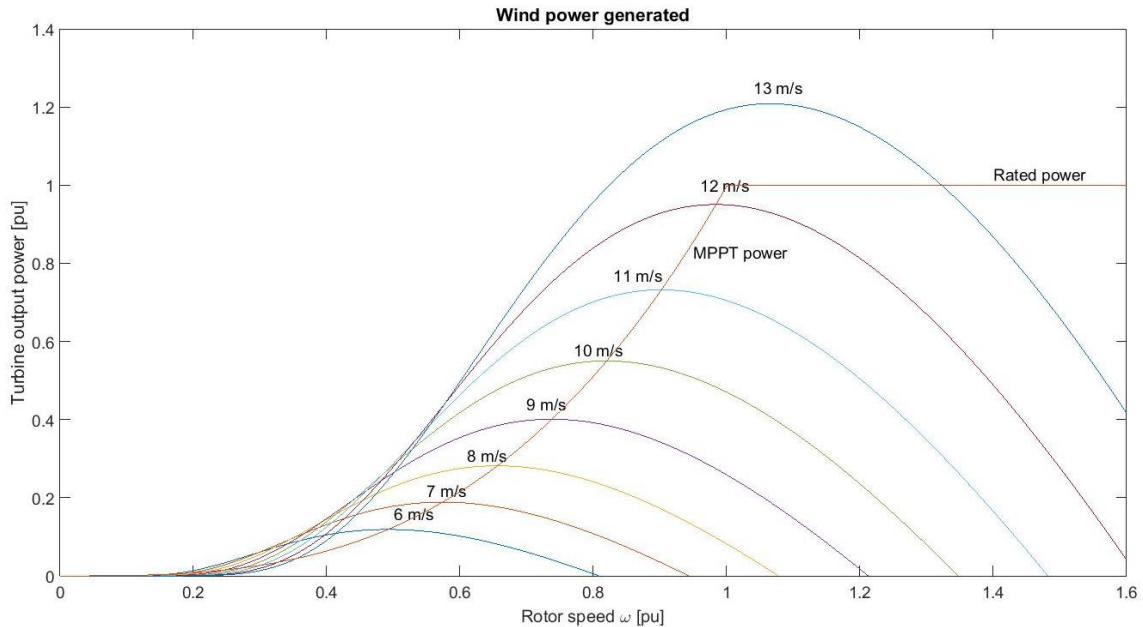


FIGURE 18: MODELED WIND TURBINE OUTPUT POWER FOR DIFFERENT WIND SPEEDS AND THE MPPT POWER [6]

The output power of the MPPT operation is also presented in Figure 18, where it can be observed that it crosses the maximum power point for each of the presented wind speeds. It is limited by the rated power of the generator, which in this case is same with the rated power of the turbine. For simplification, the MPPT is based on a look-up table, where the desired rotor speed is a function of the wind speed and the pitch control for limiting the output power to the rated power is implemented in the same way.

3.2. GENERATOR MODELING

As for the generator, the PMSG is modelled based on the mathematical equations in the dq/rotational reference frame for a synchronous machine with a salient rotor ($R_{sd} = R_{sq} = R_s$ and $L_{sd} = L_{sq} = L_s$). The electrical and mechanical equations are presented in (6) to (11), where u_{sd} , u_{sq} , i_{sd} and i_{sq} are the d, respectively q axis voltages and currents; R_s and L_s are the statoric resistance and inductance; λ_{pm} is the rotor flux linkage; ω_e and ω_m are the electrical and mechanical speeds of the machine; T_m and T_{el} are the mechanical and electrical torque of the generator; p is the number of pole pairs; J is the moment of inertia of the system reduced to the generator shaft and θ_{el} is the electrical angle of the rotor [19] [20].

The voltage equations are derived from the equivalent circuit of the machine presented in Figure 19 by using Kirchhoff's voltage law [20].

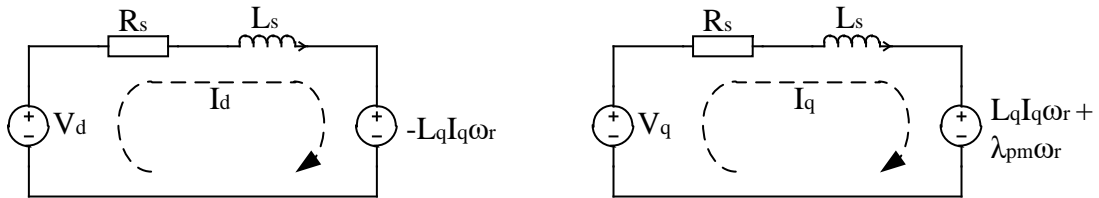


FIGURE 19: PMSG EQUIVALENT CIRCUIT FOR DQ REFERENCE FRAME

$$u_{sd} = R_s i_{sd} + L_s \frac{di_{sd}}{dt} - \omega_e L_s i_{sq} \quad (6)$$

$$u_{sq} = R_s i_{sq} + L_s \frac{di_{sq}}{dt} + \omega_e L_s i_{sd} + \omega_e \lambda_{pm} \quad (7)$$

The electrical torque the generator is producing can be described as [16]:

$$T_{el} = \frac{3}{2} p \lambda_{pm} i_{sq} \quad (8)$$

The simplified relationship between the mechanical and electrical torque can be expressed as [16]:

$$T_m - T_{el} = J \frac{d}{dt} \omega_m \quad (9)$$

Based on the electrical angular position of the rotor, the electrical angular speed can be calculated [16]:

$$\omega_{el} = \frac{d}{dt} \theta_{el} \quad (10)$$

The relationship between electrical and mechanical angular speed is given by the number of pole pairs [16]:

$$\omega_{el} = p \omega_m \quad (11)$$

The parameters used for the generator model are presented in Table 2.

TABLE 2: RATED PARAMETERS FOR THE MODELED GENERATOR

Rated mechanical power P_s	250 [kW]
Rated stator phase voltage U_s	270 [V]
Rated stator current I_s	330 [A]
Number of pole pairs	8
Rated rotor flux linkage λ_{pm}	5.826 [Wb]
Stator winding resistance R_s	8.21 [m Ω]
Stator winding inductance L_s	15.73 [mH]

3.3.AC/DC CONVERTER MODELING

The AC-DC stage consists of a 3 phase voltage source inverter which interfaces the wind turbine generator and the DC link, with the hardware configuration presented in Figure 20. The role of this converter is to control the generator by absorbing active power from it as much is needed in order to keep the speed of the wind turbine at an optimal point, given by the MPPT.

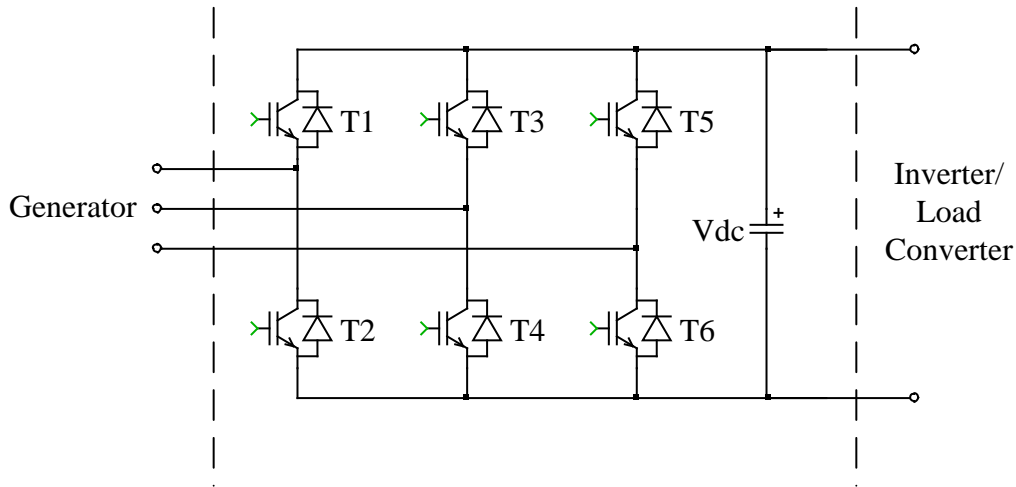


FIGURE 20: THREE-PHASE VOLTAGE SOURCE INVERTER USED FOR INTERFACING THE GENERATOR WITH THE DC-LINK

The control of the converter is based on two loops, an inner loop for the current and an outer loop for the speed control. The most used current control is the synchronous reference frame control, with the block diagram presented in Figure 21.

Due to the fact that the PI controllers have an infinite gain at zero frequency, the steady state error can be canceled for the d and q components of the current, I_d and I_q . The performance is similar with the one of resonant controllers used in the natural reference frame. For the abc to dq transformations, the rotor angle is used [21]. In order to simplify the model, it is assumed that the generator has an encoder, which gives the rotor position with high accuracy.

Besides the PI controllers two extra decoupling terms have to be used in order to have independent control over I_d and I_q . The accuracy of these terms is based on the accuracy of the filter inductor and the generator leakage inductance values. The other feed forward component ($\omega\lambda_{PM}$) is used to reduce the effort of the controllers, thus increasing the dynamics of the response [21].

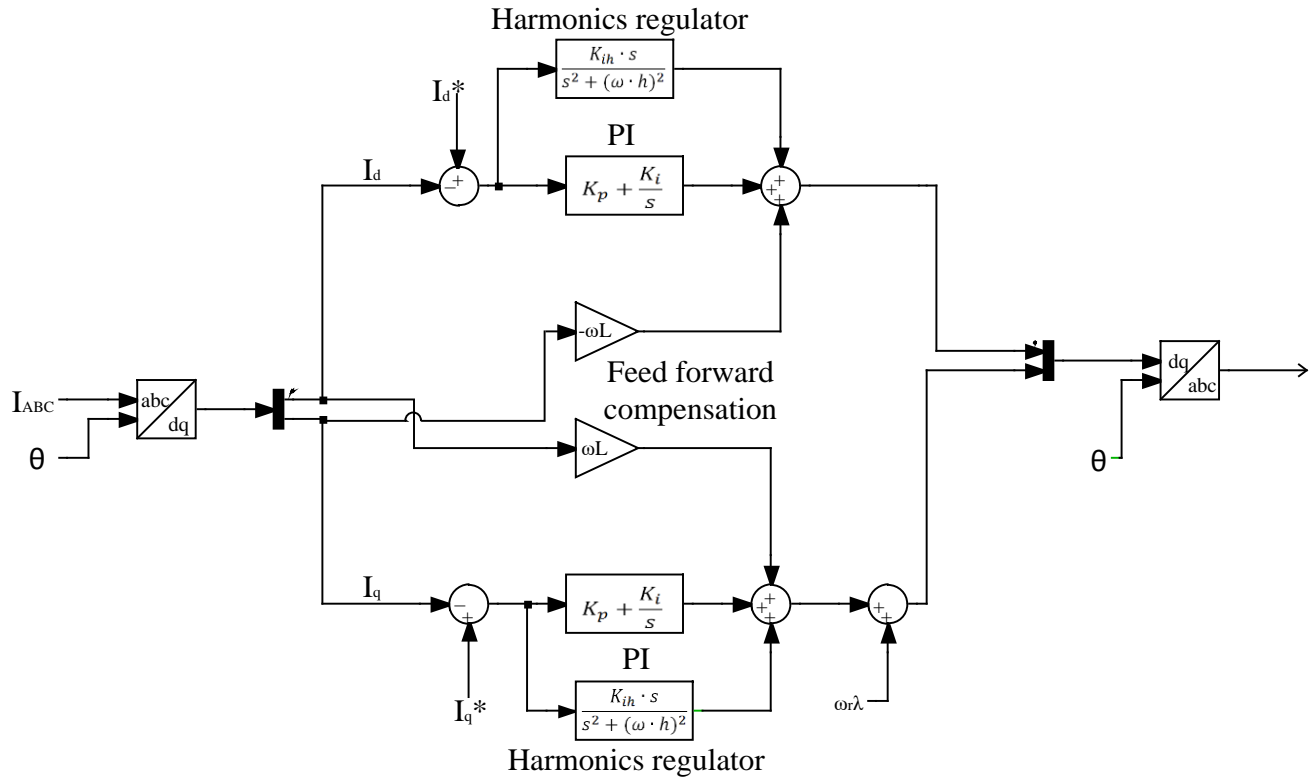


FIGURE 21: CURRENT CONTROL IN DQ REFERENCE FRAME AS PART OF THE FIELD ORIENTED CONTROL

For additional harmonic compensation, resonate controllers are used. Due to the Park transformation by rotating the reference frame with ω the 5th harmonic in negative sequence and the 7th harmonic in positive sequence become the 6th harmonic in positive and negative sequence. Having this into consideration, the number of resonant converters needed for implementation can be reduced [21].

The references for the two axes components of the current, I_d and I_q , come from the outer control loop, the speed controller and the reactive power controller. In order to maximize the torque generated by the turbine with respect to the current, the I_d reference component is set to zero.

The speed controller is generating the reference for I_q , in order to maintain the speed of the wind turbine as needed. The DC-link voltage control is done by the DC-DC converter because if the generated power is larger than the absorbed one, the DC-link voltage would raise and increase the losses or even destroy the DC-link capacitor if increased to the maximum tolerated value [22]. In a real system a braking chopper is maybe needed too for low voltage ride through and safety reasons in standalone operation.

Because the speed loop is an external loop for the control of the generator and the internal one is the current loop, this should be designed for optimum regulation, while the main focus for the internal is on short settling times (approx. 10 ms) with acceptable overshoot given by the current limitations. Because of the large difference in the response time for the two loops, they can be considered decoupled and the internal one is treated as a unity gain by the external one when designed. Linearization of the control problem is done in this way [22].

3.4. DC/DC CONVERTER MODEL

For the DC-DC converter both previously presented topologies (interleaved buck converter - Figure 22 and full bridge with high frequency transformer and rectifier - Figure 23) were modeled in order to observe the current waveforms through transistors and to evaluate them.

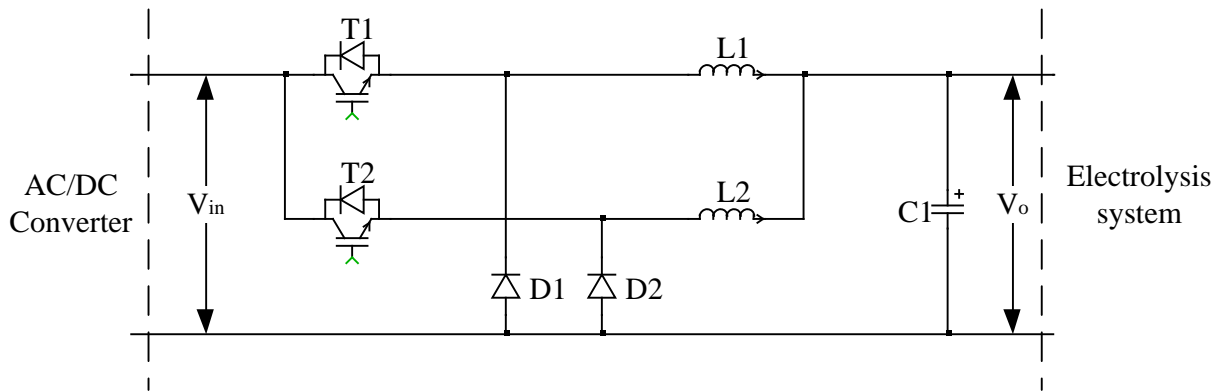


FIGURE 22: INTERLEAVED BUCK CONVERTER WITHOUT GALVANIC ISOLATION

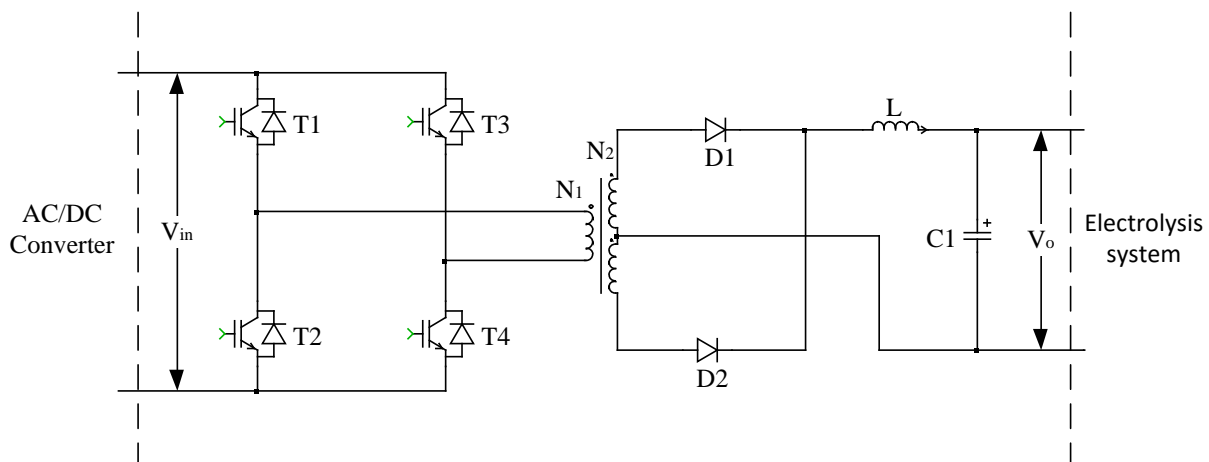


FIGURE 23: FULL BRIDGE WITH HIGH FREQUENCY TRANSFORMER AND RECTIFIER

Due to the similarity of the waveforms between the full bridge isolated converter and the non-isolated buck converter, the model is the same. The only difference that appears between the two topologies is the step-down ratio of the transformer. In steady state, for the buck converter the output voltage (V_o) to input voltage (V_i) ratio is defined by the duty-cycle (D), as in equation (12), and for the full bridge topology is the product between the duty-cycle and transformer ratio (n), as in equation (13) [23].

$$\frac{V_o}{V_i} = D \quad (12)$$

$$\frac{V_o}{V_i} = n \cdot D \quad (13)$$

In this way the model for the converter can be expressed as the ratio between output and input voltage in series with the output filter. For simplicity, only the equation for the full bridge will be presented. The case of the buck converter is the particular case when the transformer ratio is 1. The control (duty-cycle) to output voltage transfer function is presented in (14) [23].

$$\frac{V_o}{D} = \frac{nV_i R}{R + sL + s^2 LCR} \quad (14)$$

In order for this model to be valid, the converter has to be working in continuous conduction mode (CCM). In order to achieve this, the inductor values has to be greater than a minimum value found for boundary conduction mode operation, case in which the inductor current varies from zero to peak in each period. For the inductor size calculation, the full bridge topology can be seen as a buck converter, where the duty-cycle is split in half for the two pairs of transistors. The frequency is double in this case and the source is scaled with the transformer ratio [13]. Based on equation (15), taken from [13] and by knowing the switching time (T_{sw}), the minimum inductor (L_{min}) is calculated as:

$$L_{min} = \frac{nT_{sw}V_{dc}}{2I_{min}} D(1 - D) \quad (15)$$

The rated values for the converter are presented in Table 3.

TABLE 3: RATED VALUES FOR THE DC-DC VOLTAGE CONVERTER TRANSFORMER

Input voltage V_i	750 [V]
Output voltage V_o	0-250 [V]
Rated output current I_o	1300 [A]
Transformer ratio n	3:1:1
Switching frequency f_{sw}	>20 [kHz]

If a maximum current ripple through the inductor of 3% is desired, I_{min} is considered 3% of the rated current and for the worst case situation the duty-cycle is $D=0.5$ and the frequency 20 kHz. With the transformer ratio of 3/1, the minimum size of the inductor is $L_{min} = 40.6 \mu H$ for the converter to operate in CCM.

As for the output capacitor C , this one is calculated based on equation (16), taken also from [13] where ΔI_L the inductor current ripple is and ΔV_0 is the desired output voltage ripple. For a desired ripple of 1% of maximum output voltage this yields $C = 78 \mu F$.

$$C = \frac{\Delta I_L T_s}{\Delta V_0} \quad (16)$$

For efficiency evaluation of the converter and analysis of the thermal loading of the converter, a complete thermal model was done for the switching devices, including switching losses, conduction losses and thermal impedance. The models were implemented as lookup tables with data taken from the datasheet of the transistors and data given by the device manufacturers.

The operating frequency for the converter is desired to be higher than 20 kHz, thus implying use of Sic MOSFET switches in order to reduce the weight of the overall system. These have small switching losses compared to traditional IGBTs, but at high currents the conduction losses increase due to the on state resistance. To evaluate which devices to use models of IGBTs and Sic MOSFETs have been implemented and compared.

The voltage level of the DC-link voltage was chosen in order to be able to fully control the phase voltages for the generator presented in the previous sub-chapter even with some safety margins for control.

3.5. MODELING OF ELECTROLYSIS SYSTEM

For modeling the PEM electrolyzer (EZ) there are various solutions presented in literature. The two main parameters taken into consideration for modeling are the polarization curve (voltage variation with respect to current in the EZ) and the quantity of hydrogen produced. The performance of the device is also influenced by temperature and pressure, but these parameters are neglected in some of the cases for simplicity reasons [24].

For the majority of the commercial devices, the relationship between voltage and current can be considered as a linear function for most of the polarization curve. Based on this, a part of the curve can be modelled using a resistor, due to the similar behavior. For the zero current voltage a DC source or a fixed voltage diode is used. The values for the voltage source and resistor are taken from the polarization curve. For this model the temperature and pressure are not taken into account, so some loss

of accuracy is present when the temperature and pressure conditions are not the ones used for the reference polarization curve. If the modeling under different conditions is desired using this topology a new set of values for resistor and source must be used for the different polarization curve. The main advantage of this model is that it is very simple, but it lacks in adaptability for change in temperature and pressure [24].

The hydrogen production for the aforementioned model is calculated based on Faraday's law. The amount of hydrogen generated is proportional with the number of series cells (n_c) and the current through the EZ I_{EZ} , as it can be observed in (17) where F is the Faraday constant and η_F is the Faraday efficiency. The last parameter is used to take into account the deviation of the model compared with the ideal performance. The η_F can be calculated with (18) if the temperature is constant during operation [24].

$$n_{H_2} = \frac{n_c \cdot I_{EZ}}{2 \cdot F} \cdot \eta_F \quad (17)$$

$$\eta_F = 96.5 \cdot \exp\left(\frac{0.09}{I_{EZ}} - \frac{75.5}{I_{EZ}^2}\right) \quad (18)$$

By using equations (17) and (18) and the model with resistor and voltage source or a diode with a fixed voltage drop, the model is complete. For a more complete model, the voltage drop on the EZ can be expressed as two terms, one corresponding to the zero-current voltage and one depending on the current acting like a variable resistor with the values dependent of temperature and pressure, like given in (19) [24].

$$V_{EZ}(T, p) = e_{rev}(T, p) + I_{EZ} \cdot R_i(T, p) \quad (19)$$

The minimum voltage to achieve current flow is defined as reverse voltage e_{rev} and the variation of voltage with the current is defined as internal resistance R_i . This model is more accurate because it takes also into consideration the temperature and pressure in the evaluation of e_{rev} and R_i . The values for these can be expressed as given in (20) and (21) [24].

$$e_{rev}(T, p) = e_{rev0} + \frac{R \cdot T}{2 \cdot F} \ln\left(\frac{p}{p_0}\right) \quad (20)$$

$$R_i(T, p) = R_{i0} + k \cdot \ln\left(\frac{p}{p_0}\right) + dR_t \cdot (T - T_0) \quad (21)$$

In the presented formulas the reference parameters are: e_{rev0} , p_0 , R_{i0} and T_0 , R is the ideal gas constant of $1 \text{ atm K}^{-1} \text{ mol}^{-1}$, and dR_t and k can be taken by curve fitting the polarization curve. As for the hydrogen production, compared with the previous model the only modification is the efficiency, which now is expressed as a function of temperature and pressure in (22) [24].

$$n_{H_2}(T, p) = \frac{n_c \cdot I_{EZ}}{2 \cdot F} \cdot \frac{T \cdot R}{p} \quad (22)$$

Due to the fact that the focus of the project is on the power electronics side of the system, in this project a simple approach of modeling the electrolysis system was adopted and the temperature and pressure were not taken into consideration [24]. This means that the electrolysis system will be modeled by a DC voltage source in series with a resistor based on the I-V curve.

The approximation is done based on the measured characteristic of an electrolysis cell, by approximating the curve with a first order polynomial function in a least-square sense. In Figure 24 it can be observed the original curve and the approximated one. The last one has the characteristic polynomial equation as presented in (23). For the whole electrolysis system, the voltage is multiplied with the number of series electrolysis cells and the relationship between voltage and current becomes (24) because in the electrolysis system is composed of 80 cells.

$$V = 1.621 + 0.0006 * I \quad (23)$$

$$V = 129.6 + 0.048 * I \quad (24)$$

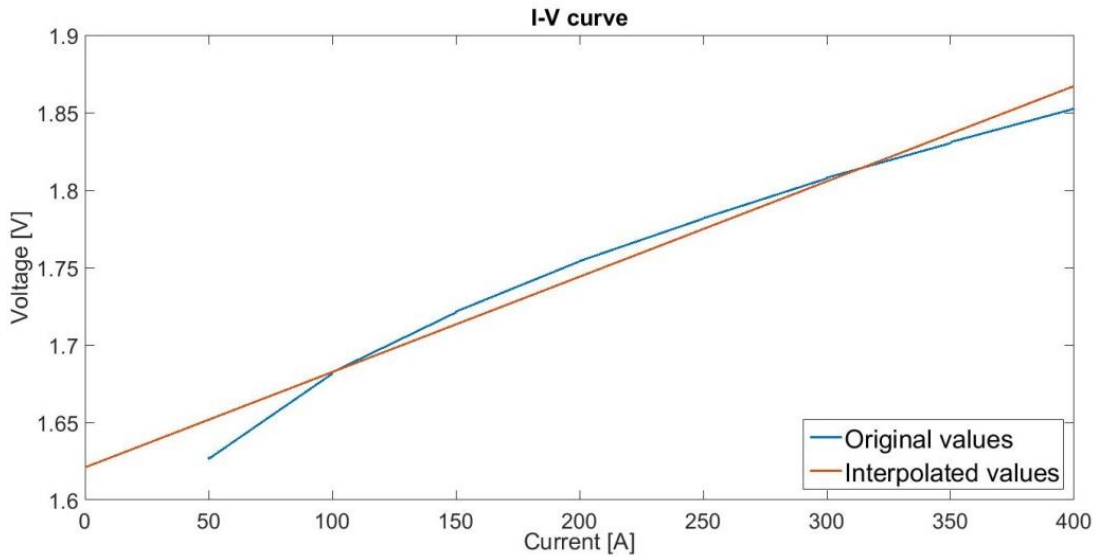


FIGURE 24: I-V CHARACTERISTIC OF AN ELECTROLYSIS CELL AT T=80 DEGREES CELSIUS

3.6. DESIGN OF CONTROL FOR AC/DC CONVERTER

In order to be able to design the current controllers for the Field Oriented Control (FOC) strategy, the back electromotive force (BEMF) needs to be decoupled and this implies a compensation method. This is done based on the voltage equations in Laplace domain (25) and (26). As it can be observed, if the terms with ω are reduced, the equation is reduced to a simple RL circuit. The compensation is done by introducing two feed-forward terms in the control loop, as shown in Figure 25.

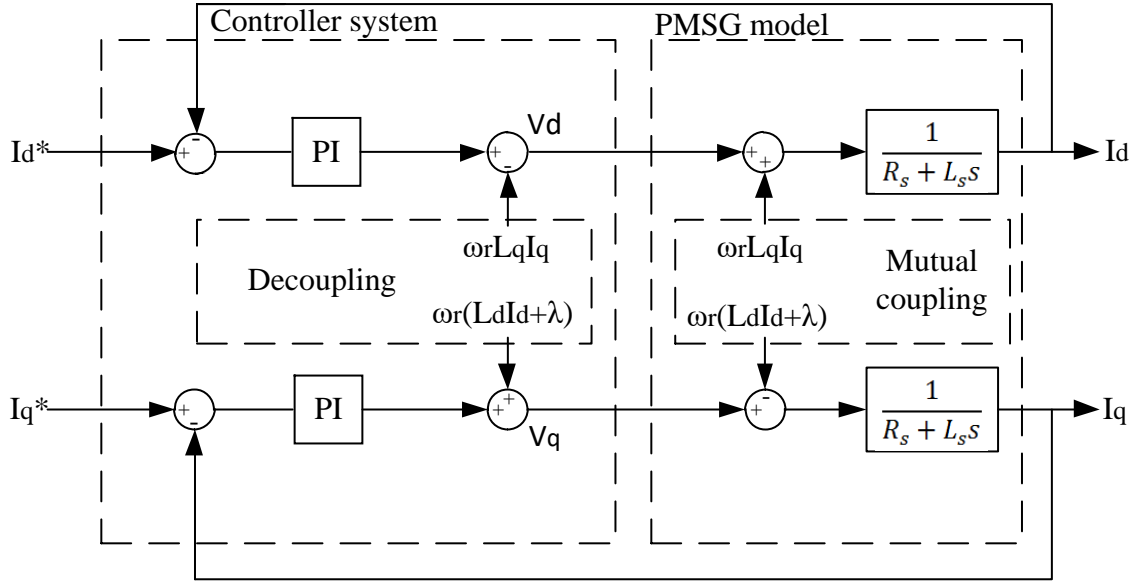


FIGURE 25: DECOUPLING OF THE BACK-EMF IN DQ REFERENCE FRAME FOR GENERATOR CONTROL

$$u_{sd} = R_s i_{sd} + L_s s i_{sd} - \omega_e L_s i_{sq} \quad (25)$$

$$u_{sq} = R_s i_{sq} + L_s s i_{sq} + \omega_e L_s i_{sd} + \omega_e \lambda_{pm} \quad (26)$$

By using the decoupling method and assuming it is complete, the relationship between the voltage and current can be expressed by:

$$\frac{i_{sd}}{u_{sd}} = \frac{i_{sq}}{u_{sq}} = \frac{1}{R_s + L_s s} \quad (27)$$

The control strategy of the generator is presented in Figure 14, where PI controllers are introduced in all 3 control loops (both current control loops and also the speed control loop) to ensure a zero steady state error. Because the two current loops are the same, only one will be analyzed and the same parameters will be used for both.

The reduced control scheme is presented in Figure 26, where a delay of one sample time (T_s) is introduced due to the modulator and sampled system. In order to obtain the parameters for the current PI controller, the root locus for different values of T_i is drawn. After analyzing the results, a T_i value of 0.04 was chosen and based on the root locus a K_p value of 13.5 is used. This gives a 5% overshoot in the current step response and a settling time of 2 ms is obtained shown in Figure 27.

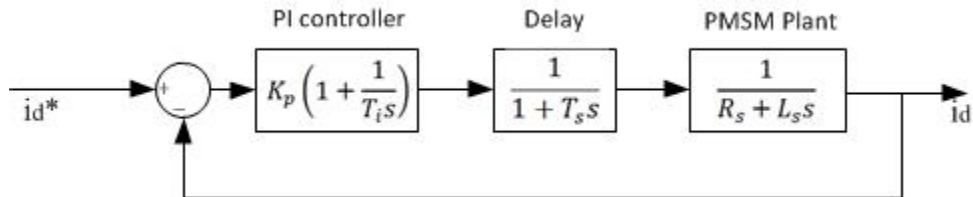


FIGURE 26: SIMPLIFIED CONTROL LOOP OF THE GENERATOR CURRENT CONTROL LOOP

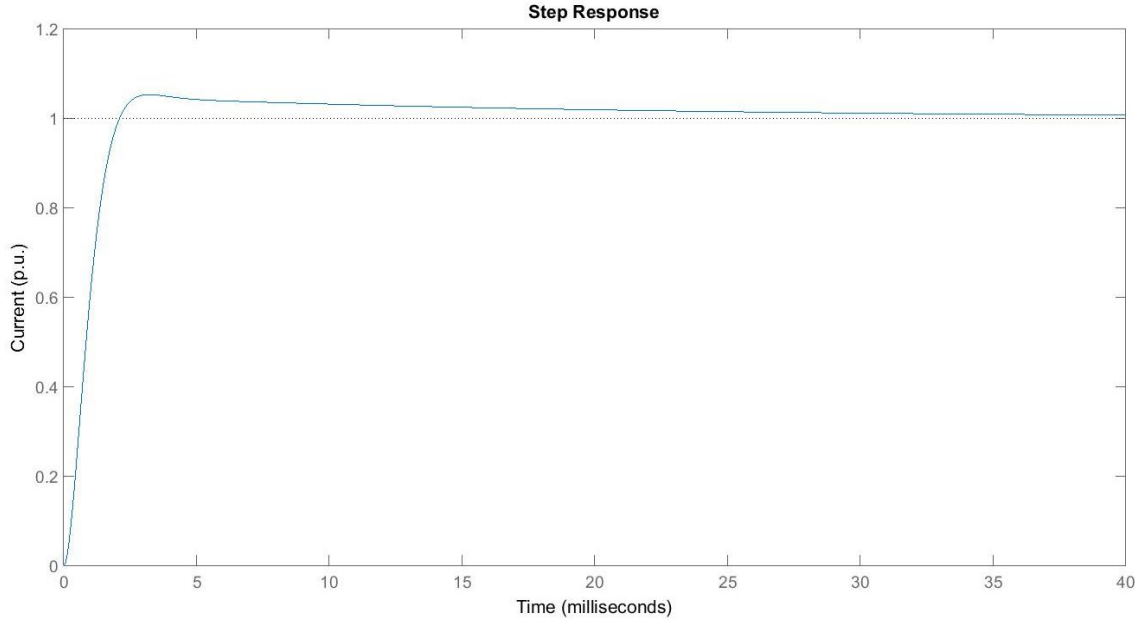


FIGURE 27: STEP RESPONSE OF THE CURRENT CONTROLLER USED FOR GENERATOR CONTROL LOOP

As for the speed controller parameters, the same approach is used. Based on the mechanical equation in the s-domain presented in equation (28) the transfer function between speed and torque is derived as presented in equation (29), where the moment of inertia of the generator-wind turbine ensemble it is considered 100 [kNm]. As the torque is proportional with the current (30), simplified control block diagram can be presented as shown in Figure 28.

$$T_{el} - T_m = Js\omega_m \tag{28}$$

$$G_{\omega}(s) = \left. \frac{\omega_m}{T_{el}} \right|_{T_m=0} = \frac{1}{Js} \quad (29)$$

$$T_{el} = \frac{3}{2} p \lambda_{pm} i_{sq} = K_t i_{sq} \quad (30)$$

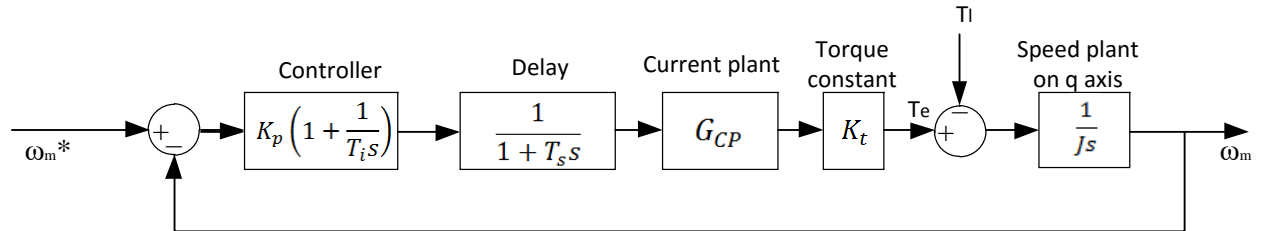


FIGURE 28: SIMPLIFIED BLOCK DIAGRAM FOR GENERATOR SPEED CONTROL LOOP

Due to the fact that the speed loop should be at least ten times slower than the current controller in order to be able to consider them as decoupled, the T_i constant in this case is chosen to be 4, and from the root locus, the value of 5600 is chosen for K_p , which gives a 2 s settling time and 8% overshoot, therefore respecting the demands (settling time of 5 s and 20% overshoot). The step response can be seen in Figure 29.

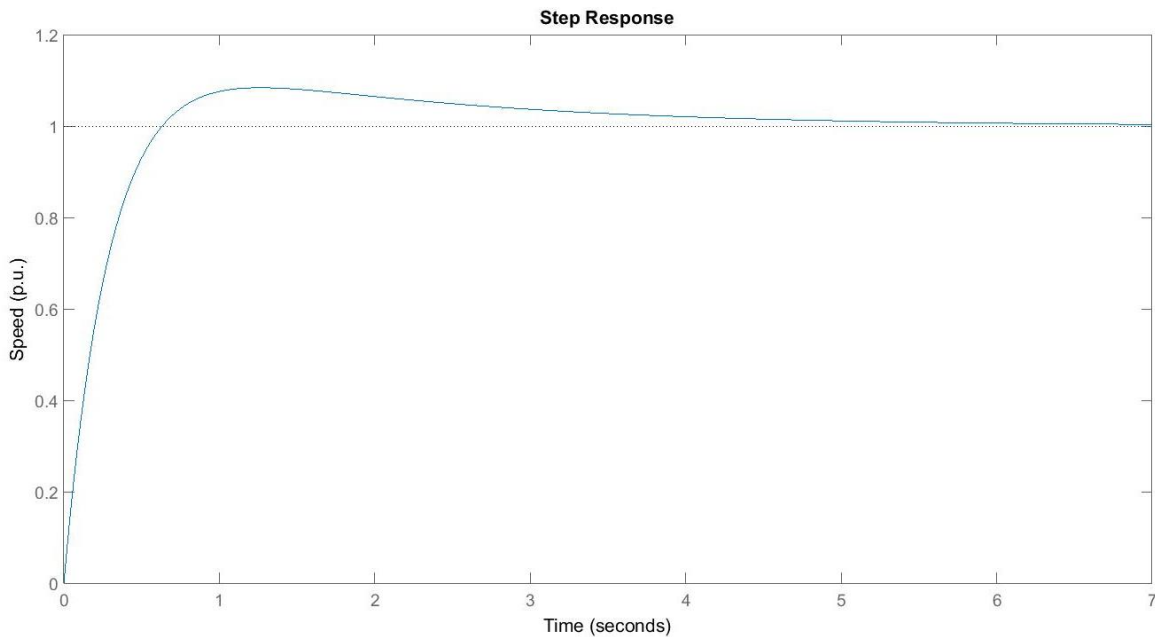


FIGURE 29: STEP RESPONSE OF THE SPEED CONTROLLER FOR THE GENERATOR

3.7. DESIGN OF CONTROL OF DC/DC CONVERTER

Due to the fact that the load of the converter is represented by a diode with a fixed voltage drop (V_f) and resistor (R), the design of the current controller has to take this into account. In this case, the converter transfer function presented in equation (14) becomes (31).

$$\frac{V_o}{D} = \frac{I_o R + V_f}{D} = \frac{nV_i R}{(R + sL + s^2 LCR)} \quad (31)$$

As the voltage drop is assumed constant, the transfer function can be reduced to:

$$\frac{I_o}{D} = \frac{nV_i}{(R + sL + s^2 LCR)} \quad (32)$$

The control block diagram can be represented by Figure 30.

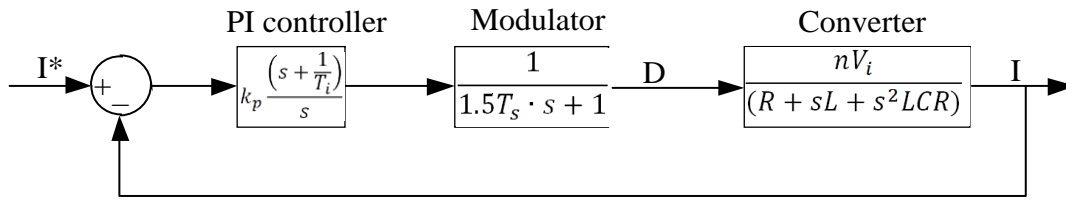


FIGURE 30: BLOCK DIAGRAM OF DC-DC CONVERTER CURRENT CONTROL LOOP

For designing the controller, an integral constant $T_i = 1$ ms was chosen and based on the root locus, a proportional gain of $k_p = 9.1 * 10^{-5}$ has been selected. The step response of the loop can be observed in Figure 31. The rise time is 3 ms and the overshoot is 7%.

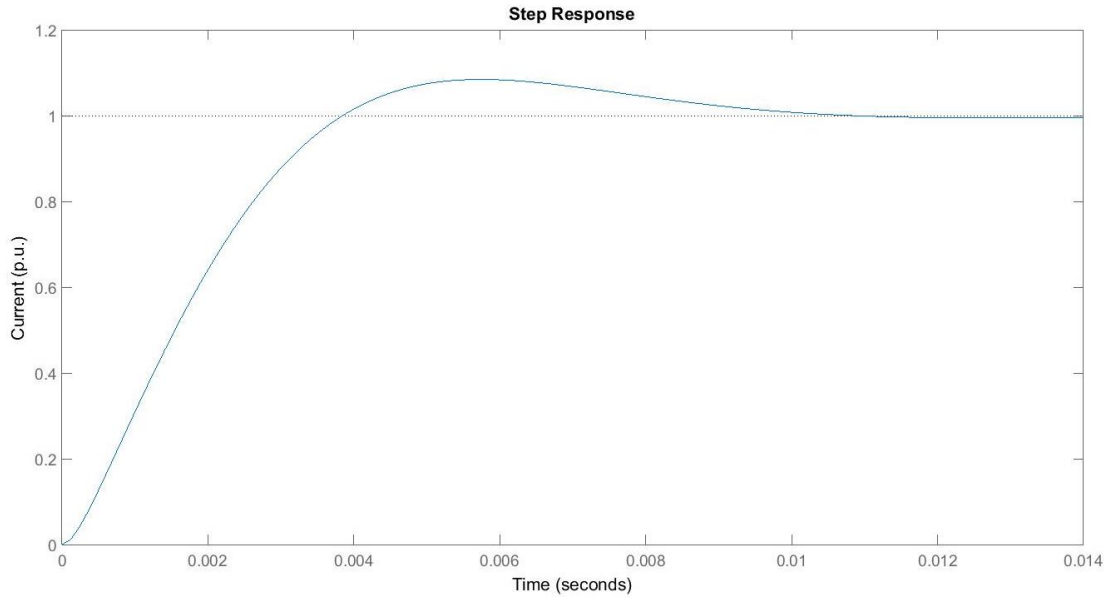


FIGURE 31: STEP RESPONSE OF CURRENT CONTROL LOOP FOR THE DC-DC CONVERTER

For the Dc-link voltage control the equations are derived from the schematic presented in Figure 32.

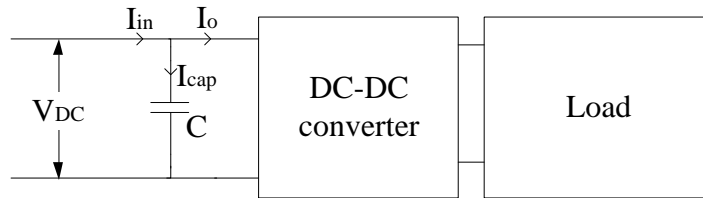


FIGURE 32: SIMPLIFIED SYSTEM SCHEMATIC WITH DC-LINK VOLTAGE CONTROL

Knowing the relation between the DC-link capacitor voltage (V_{dc}) and the capacitor expressed in (33) and the relationship between the converter current (I_o), capacitor current (I_{cap}) the control diagram of the DC-link voltage can be drawn as in Figure 33.

$$\frac{V_{dc}}{I_{cap}} = \frac{1}{Cs} \quad (33)$$

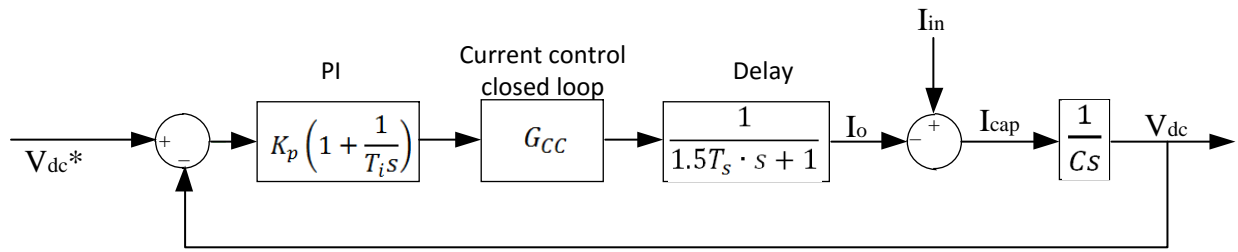


FIGURE 33: CONTROL DIAGRAM OF DC-LINK VOLTAGE CONTROL FOR THE DC-DC CONVERTER

For the DC-link voltage loop the integral constant T_i was chosen 100 times larger than for the current control based on root locus. This is due to the fact that the outer loop needs to be at least 10 times slower compared to the inner loop in order to provide proper decoupling between them. If the inner loop is not at least 10 times faster compared to the external one, it cannot be assumed that they are decoupled and the presented control strategy would not be valid. Based on the root locus, $k_p = 0.27$ value is chosen. The step response can be seen in Figure 34, where the response time is less than 30 ms and the overshoot does not exceed the 10% requirement.

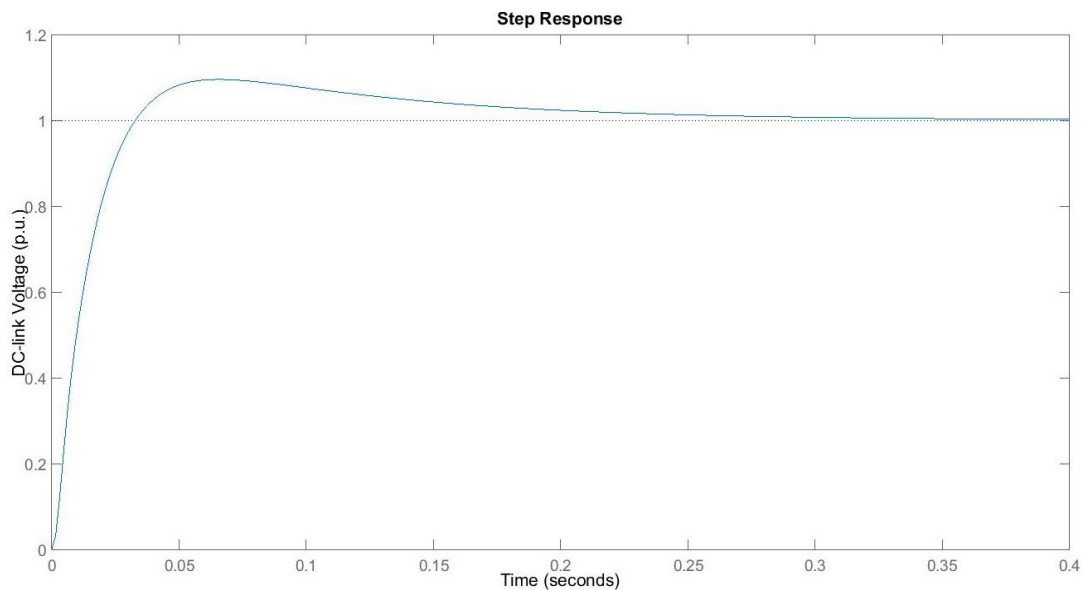


FIGURE 34: DC-LINK VOLTAGE RESPONSE TO A STEP IN REFERENCE VOLTAGE FOR THE DC-DC CONVERTER VOLTAGE CONTROL

3.8. DESIGN OF POWER ELECTRONICS FOR DC/DC CONVERTER

As mentioned in the introduction, one of the objectives of this thesis is to design the DC-DC converter which interfaces the DC-link with the electrolysis system. In the following part of this chapter, the topology selection, selection of power electronic devices and design of magnetic components is performed.

The values for the output filter inductor and capacitor were already calculated due to the fact that the values were needed for modeling purposes. In this subchapter the design of power electronics is made based on thermal simulations of two considered devices.

Based on the performance of the available devices on the market, for thermal simulation two of them were chosen, an IGBT (FF600R12IS4F from Infineon) and a Sic MOSFET (CAS300M12BM2 from Wolfspeed). To have a complete view on the possible topologies, simulations were made using both of them in the topologies presented in Figure 22 and Figure 23: an interleaved buck converter with two switches and full bridge topology with one full bridge in series with a high frequency transformer and rectifier. To be able to compare the losses, the switching frequency was kept at 20 KHz for all simulations and the junction temperature of the devices was considered to be 70 degrees Celsius. The results are presented in Table 4.

TABLE 4: TRANSISTOR LOSSES IN THE DC-DC CONVERTER FOR THE TWO PRESENTED TOPOLOGIES

Topology	No. of transistors	Average current through switch	Device	Conduction losses/device [W]	Switching losses/device [W]	Total Losses [W]
Full bridge topology	4	185	IGBT	380	1940	9280
Buck topology	2	185	IGBT	600	4660	10520
Full bridge topology	4	185	SiC MOSFET	710	360	4280
Buck topology	2	185	SiC MOSFET	1475	1640	6230

As it can be seen from the Table 4, even at 20 kHz, the Sic device proves to have a better performance compared with the IGBT. Increasing the frequency will mean a proportional increase of the switching losses, which in the case of the IGBT are very high compared to the others. Taking this into consideration, a more detailed thermal analysis is made using the Sic devices, which takes into account the Cauer thermal model, like shown in Figure 35 and the thermal resistance of the heat-sink and thermal grease.

The Cauer model describing the junction to case behavior was given by the manufacturer and it consists of a 14-element RC network, presented in Table 5. For the thermal grease used to interface the device with the heatsink it has been calculated a value of 10 K/kW for an ideal plane surface with the size of the module and a 50 μm thickness, but a value of 38 K/kW is used for simulations to take into

consideration the imperfections surface planarity, grease thickness and also to include a safety margin. For the heat-sink, based on the datasheet, a resistance of 30 K/kW is considered.

TABLE 5: JUNCTION TO CASE THERMAL NETWORK FOR SIC MOSFET USED FOR DC-DC CONVERTER

No.	1	2	3	4	5	6	7	8	9
R	1.26e-3	3.38e-3	4.55e-3	6.52e-3	7.21e-3	8.1e-3	7.39e-3	5.34e-3	4.45e-3
C	1.21e-2	4.28e-2	7.88e-2	9.62e-2	1.25e-1	1.73e-1	2.42e-1	4.82e-1	1.18

10	11	12	13	14
6.08e-3	8.9e-3	7.79e-3	2.59e-30	6.49e-3
2.13	2.28	2.64	8.52	249

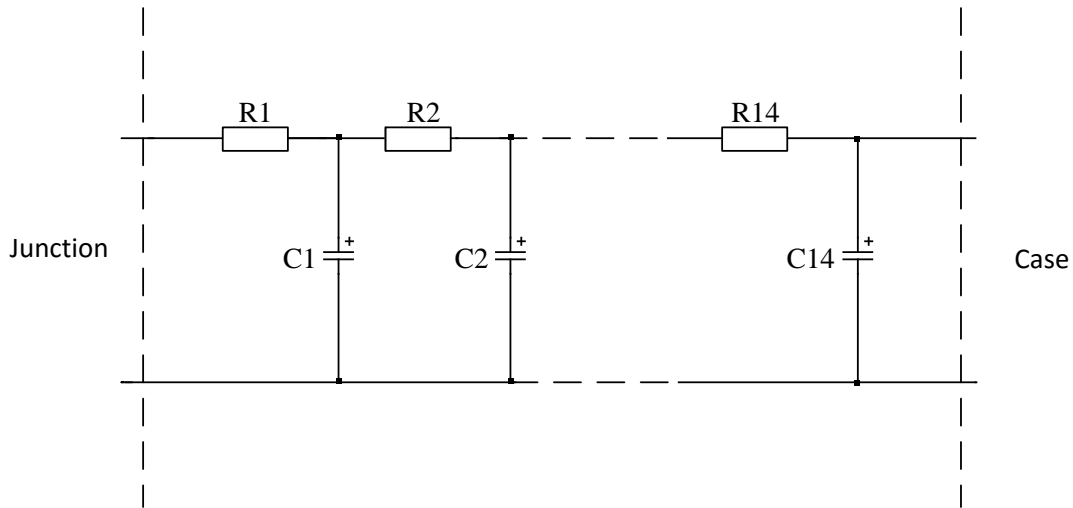


FIGURE 35: CAUER NETWORK USED TO SIMULATE THE THERMAL BEHAVIOR OF THE DEVICE

Taking into consideration that the maximum junction temperature is 150 degrees Celsius; a maximum acceptable value for the junction temperature for simulations is 120°C in order to have a safety margin and to allow a small overload of the system without affecting the robustness margin.

For the galvanic isolated topology it has been calculated the maximum power at which the converter can work having just one full bridge for three different frequencies and reach a junction temperature of MOSFETS of 120 degrees Celsius. This was done because in order to increase the output power, more can be put in parallel and interleaved. The results can be seen in Table 6, where the efficiency was calculated by considering the transformer having 99.8% efficiency. The diode losses were not taken into consideration neither for the galvanic isolation calculation, nor for the non-isolated one.

TABLE 6: MAXIMUM ALLOWED POWER FOR DIFFERENT SWITCHING FREQUENCIES FOR GALVANIC ISOLATED SYSTEM (SEE FIGURE 23)

Frequency [kHz]	Conduction losses [W]	Switching losses [W]	Power [kW]	Efficiency [%]
25	170	155	116	98.7
50	109	225	90	98.3
75	75	258	74	98

For the non-galvanic isolated topology the same approach was taken, verifying what is the maximum power that can be transferred by the proposed converter in order to keep the junction temperature at a maximum of 120 degrees. The results are presented in Table 7. As for the galvanic isolated topology calculations, the diode losses were not taken into account for efficiency calculation.

TABLE 7: MAXIMUM ADMISSIBLE POWER FOR DIFFERENT SWITCHING FREQUENCIES FOR THE BUCK CONVERTER TOPOLOGY (SEE FIGURE 22)

Frequency [kHz]	Conduction losses [W]	Switching losses [W]	Power [kW]	Efficiency [%]
25	140	346	90	98.9
50	55	437	56	98.2
75	34	515	38	97.1

Based on the simulation results and the fact that for one full bridge 2 SiC modules were needed, the same as for the Buck topology, it can be concluded that for a power of 250 kW the galvanic isolated topology requires a total of 6 modules and the buck converter topology requires 10 modules. Based on this and that at 50 kHz the efficiency is similar for both topologies it was decided to use 3 galvanic isolated converters interleaved, each one working at 50 kHz. Increasing the switching frequency more will result in a need of more converters, and choosing the buck topology at the same frequency will require more modules (4 more). Furthermore the fact that the full bridge topology converter provides galvanic isolation is an advantage. Considering this, each of the three converters will be rated for 85 kW so that when they are interleaved the total power is a bit higher than the required 250 kW in order to include a safety margin.

As the frequency and the rated current of the converter are changed compared to the ones used for designing the inductor and capacitor, these have to be scaled taking into consideration the change in parameters. In this case the inductor size for the same admissible ripple is $L_{min} = 48.7 \mu H$ and the capacitor is $C = 104 \mu F$.

3.9. DIODE SELECTION OF THE RECTIFIER PART

Based on the presented topology of the rectifier with a midpoint secondary transformer and two diodes, the current through one of the diodes can take three values: inductor current value during diode conduction, zero during the conduction period of the other diode and half the load current during freewheeling operation, like is shown in Figure 36. Because of this, the stress on the diode is higher compared to the case when a full rectifier bridge is used. [13]

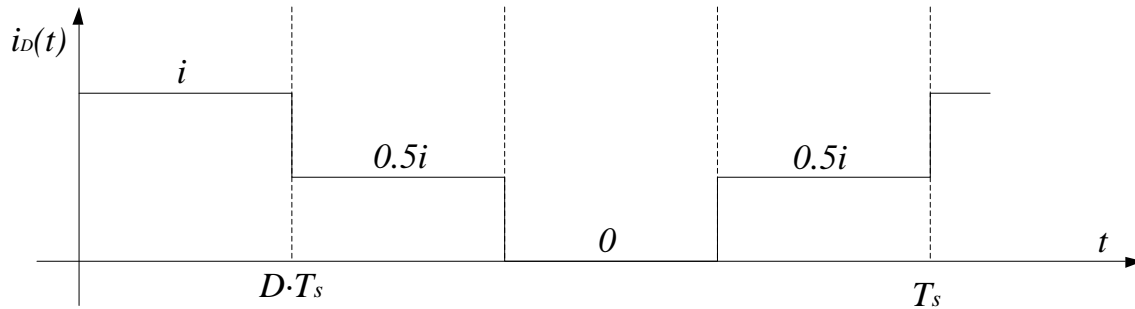


FIGURE 36: DIODE CURRENT WAVEFORM IN THE RECTIFIER SIDE FOR A CENTER TAPPED SECONDARY WINDING AND A TWO DIODE RECTIFIER [14]

Due to the fact that three converters are used in parallel, the rated current for one of the converters is a third of the load current, which is 434 amps, and based from simulations it can be concluded that the average current through a diode in this case is 216.7 amps.

Knowing the necessary current at which the diode has to withstand, based on cost of the diodes a few different types were analyzed. From these, only two were modeled and verified in simulation that they can dissipate the power having a forced cooled heat-sink. The two are: S320Q from GeneSic and VS-301U from Vishay, the others having either a higher voltage drop at the same price range or increased price for the same performance.

For the heat-sink, one from Wakefield-Vette is used which has 200 K/kW thermal resistance and for the thermal paste a value of 80 K/kW is used (the value is specified as thermal resistance in the case of connection of diode to plain surface in the Vishay diode datasheet). For the thermal modeling of the diodes the Cauer network is not provided and only the thermal resistance being specified, which is sufficient for the steady state analysis.

Based on the thermal simulation, the losses on one from Genesic are higher than the dissipation capabilities of the heatsink and the junction temperature would be high over the maximum admissible one. This type of diode could be used if two are put in parallel, case in which the junction temperature decreases to 90 degrees Celsius, maximum of 150 Celsius being the maximum.

In the case of the Vishay diode, due to the reduced on-state voltage drop and thermal resistance, the junction temperature at full load will increase to 130 degrees Celsius. This is below the value for maximum admissible temperature, which in this case is 180 degrees as specified in the diode datasheet.

Although the price for the GeneSic diode is almost half compared to the Vishay ones, the latter is still chosen because it reduces the number of components and also it reduces the number of necessary heatsinks and the overall cost is lowered.

3.10. TRANSFORMER DESIGN

The basic step in designing a transformer is the selection of the core. The material is chosen based on a tradeoff between performance and cost effectiveness. In the presented case, ferrite is chosen as material due to the high switching frequency of the converter in order to reduce size. After the material for the core has been decided, the size of it can be calculated using the core geometry (Kg) approach. Each core has its own Kg, which is related to the voltage regulation and power handling [25].

For a proper core selection, the total apparent power has to be calculated like it is presented in equation (34), where P_t represents the apparent power, which the transformer has to handle, P_o is the output power of the transformer, P_{in} is the input power and η is the efficiency of the transformer [25].

$$P_t = P_{in} + 1.41P_o \quad (34)$$

$$P_o = V_o * I_o \quad (35)$$

$$P_{in} = \frac{P_o}{\eta} \quad (36)$$

The output power has to be multiplied with 1.41 because the secondary windings are center tapped and the current waveform is interrupted. This factor corrects for the RMS value of the current in the winding [25].

As for the voltage regulation α , this one is defined as in equation (37), where $V_o(F.L.)$ represents the output voltage at full load and $V_o(N.L.)$ represents the output voltage at no load [25].

$$\alpha = \frac{V_o(N.L.) - V_o(F.L.)}{V_o(F.L.)} \cdot 100 [\%] \quad (37)$$

Another expression for voltage regulation is presented in equation (38), as the ratio of copper losses (P_{cu}) to output power of the transformer [25].

$$\alpha = \frac{P_{cu}}{P_o} \cdot 100 [\%] \quad (38)$$

The relationship between power regulation and transformer power-handling capability is given by the geometry factor K_g determined by the core dimensions as shown in equation (40), and the electrical constant K_e which is given by equation (41) [25].

$$\alpha = \frac{P_t}{2K_g K_e} [\%] \quad (39)$$

$$K_g = \frac{W_a A_c^2 K_u}{MLT} [cm^5] \quad (40)$$

$$K_e = 0.145 K_f^2 f^2 B_m^2 (10^{-4}) \quad (41)$$

Where the winding area or the transformer is W_a , A_c is the cross-section area of the core, K_u is the window utilization factor, MLT represents the mean length of a turn, K_f is a waveform coefficient ($K_f = 4$ for square wave), f is the switching frequency of the converter and B_m is the maximum induction of the core [25].

Based on the geometry factor, a core can be chosen in order to provide the desired voltage regulation, after which the number of primary (N_p) turns can be calculated using Faraday's Law [25]:

$$N_p = \frac{V_{in}(10^4)}{K_f * B_m * f * A_c} \quad (42)$$

After this, the current density J can be calculated as a function of the window utilization factor K_u , induction B_m , frequency f and cross-sectional area of the core A_c [25].

$$J = \frac{P_t(10^4)}{K_f K_u B_m f A_c W_a}, [amps/cm^2] \quad (43)$$

The primary bare wire area $A_{wp,bare}$ representing the copper area needed is then derived as:

$$A_{wp,bare} = \frac{I_{in,max}}{J}, [cm^2] \quad (44)$$

For a high switching frequency, the skin effect can cause higher losses, so a wire with a diameter of less than double the skin depth is chosen. The skin depth can be calculated as in equation (45). This requires more wires to be used in parallel, and the number of strands determined using equation (46) where $A_{wp,single}$ represents the area of a single strand for the wire [25].

$$\varepsilon = \frac{6.62}{\sqrt{f}}, [cm] \quad (45)$$

$$S_{np} = \frac{A_{wp,bare}}{A_{wp,single}} \quad (46)$$

Based on the number of strands the resistance of the wire can be calculated as in equation (47). The copper resistance (ρ_{Cu}) is temperature dependent, but for initial calculations the value of the resistance at 30 degrees Celsius can be considered [25]:

$$R_p = \frac{\rho_{Cu} * MLT * N_p}{A_{wp, single} * S_{np}}, [amps/cm^2] \quad (47)$$

The number of each secondary winding turns can be calculated as a ratio between the primary and secondary voltages, and also taking into consideration the voltage regulation [25]:

$$N_s = \frac{V_s * N_p}{V_{in}} \left(1 + \frac{\alpha}{100}\right) \quad (48)$$

The rest of the parameters for the secondary windings can be calculated with equations (44), (46) and (47) [25].

By knowing the resistance of all the windings, the copper losses can be easily calculated as in (49) where the secondary winding is seen as two different windings [25]:

$$P_{cu} = R_p * I_p^2 + 2 * R_s * I_s^2 \quad (49)$$

Using equation (38) it can be verified if the current regulation requirement is respected.

The core losses can be obtained from the datasheet of the material or calculated by first determining the milliwatts per gram (mW/g) losses specific to the material and multiplying it with the core weight. As it can be observed, it is dependent on the operating frequency and the ac induction load [25]:

$$\frac{mW}{g} = 0.000318 * f^{1.51} B_{ac}^{2.747} \quad (50)$$

$$P_{fe} = \frac{mW}{g} * W_{tfe} * 10^{-3}, [W] \quad (51)$$

The temperature rise (T_r) can be determined by taking into consideration the losses and the surface area of the transformer (A_t) [25].

$$\psi = \frac{(P_{fe} + P_{cu})}{A_t}, [W/cm^2] \quad (52)$$

$$T_r = 450\psi^{0.826}, [^\circ C] \quad (53)$$

As for the design specifications, like it was previously mentioned, the DC-DC converter will be composed from three interleaved converters, each rated at 85 kW. Considering this, the specifications for the high frequency transformer are specified in Table 11 and the transformer topology can be observed in Figure 37.

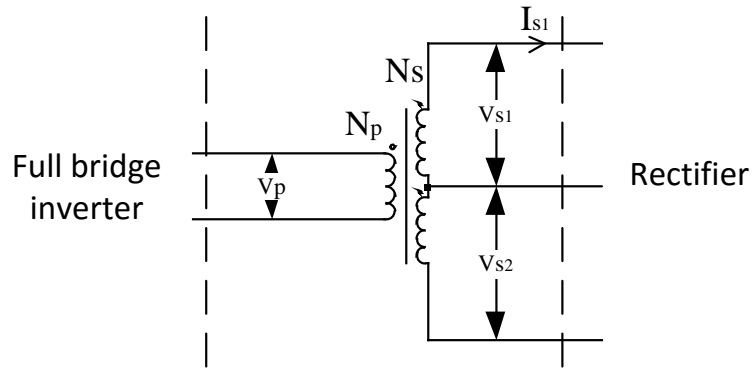


FIGURE 37: TRANSFORMER TOPOLOGY USED FOR THE DC-DC CONVERTER

TABLE 8: 85 KW TRANSFORMER SPECIFICATIONS

Input voltage V_p	750 [V]
Output voltage #1 V_{s1}	250 [V]
Output voltage duty-cycle #1	0.76
Output current #1 I_{s1}	225 [A]
Output voltage #2 V_{s2}	250 [V]
Output voltage duty-cycle #2	0.76
Output current #2 I_{s2}	225 [A]
Frequency f	50 [kHz]
Efficiency η	99 [%]
Regulation α	1 [%]
Operating flux density B_m	0.15 [Wb]
Core material	ferrite
Window utilization factor K_u	0.4

By using the formulas presented before a wire with a diameter of 0.4 mm was chosen and based on the calculations two ferrite E185 cores were chosen with the specifications presented in Table 9. The core was chosen based on the fact that the geometry factor was supposed to be greater than 21.

TABLE 9: CORE SPECIFICATIONS FOR THE 85 KW DC-DC CONVERTER TRANSFORMER

Core number	2 x E185
Manufacturer	NCD
Magnetic material	LP3A
Magnetic path length l_m	37 [cm]
Window height	10 [cm]
Core weight W_{tfe}	5600 [g]
Mean length turn MLT	32 [cm]
Cross-sectional area A_c	14.3 [cm ²]

Area product A_p	536 [cm^4]
Core geometry factor K_g	70
Surface area A_t	1345 [cm^2]

The specifications for the transformer that resulted from the presented formulas are given in Table 10.

TABLE 10: FINAL TRANSFORMER SPECIFICATIONS OF A 85 KW TRANSFORMER

Number of primary windings N_p	18
Number of secondary winding turns N_s	6
Current density J	446 [A/cm^2]
Wire area primary $A_{wp,bare}$	0.25 [cm^2]
Number of strands primary S_{np}	207
Wire area secondary $A_{ws,bare}$	0.5 [cm^2]
Number of strands secondary S_{ns}	401
Primary winding resistance R_p	1.7 [$m\Omega$]
Secondary winding resistance R_s	0.31 [$m\Omega$]
Copper losses P_{cu}	55 [W]
Iron losses P_{fe}	18 [W]
Voltage regulation α	0.06 [%]
Temperature rise	40 [$^{\circ}C$]

In order to verify the design methodology and the functionality of the converter, a small scale transformer is designed for a power of 10 kW. The transformer winding configuration is the same as shown in Figure 37 and the electrical requirements for the transformer are presented in Table 11.

TABLE 11: 10 KW TRANSFORMER SPECIFICATIONS

Input voltage V_p	750 [V]
Output voltage #1 V_{s1}	250 [V]
Output voltage duty-cycle #1	0.4
Output current #1 I_{s1}	50 [A]
Output voltage #2 V_{s2}	250 [V]
Output voltage duty-cycle #2	0.4
Output current #2 I_{s2}	20 [A]
Frequency f	50 [kHz]
Efficiency η	99 [%]
Regulation α	1 [%]
Operating flux density B_m	0.15 [Wb]
Core material	ferrite
Window utilization factor K_u	0.4

By using the formulas presented before a wire with a diameter of 0.4 mm was chosen and based on the calculations two ferrite E70 cores were chosen with the specifications presented in Table 12. The core was chosen based on the fact that the geometry factor was supposed to be greater than 2.6.

TABLE 12: CORE SPECIFICATIONS FOR THE 10 KW DC-DC CONVERTER TRANSFORMER

Core number	2 x E70
Manufacturer	TDK
Magnetic material	N87
Magnetic path length l_m	14.9 [cm]
Window height	4.38 [cm]
Core weight W_{tfe}	514 [g]
Mean length turn MLT	25.4 [cm]
Cross-sectional area A_c	7.04 [cm ²]
Area product A_p	80 [cm ⁴]
Core geometry factor K_g	6.64
Surface area A_t	227 [cm ²]

The specifications for the transformer that resulted from the presented formulas are given in Table 13.

TABLE 13: FINAL TRANSFORMER SPECIFICATIONS OF A 10 KW TRANSFORMER USED FOR PROTOTYPE TESTING

Number of primary windings N_p	27
Number of secondary winding turns N_s	9
Current density J	236 [A/cm ²]
Wire area primary $A_{wp,bare}$	0.0535[cm ²]
Number of strands primary S_{np}	43
Wire area secondary $A_{ws,bare}$	0.1289[cm ²]
Number of strands secondary S_{ns}	103
Primary winding resistance R_p	0.0107[Ω]
Secondary winding resistance R_s	0.0015[Ω]
Copper losses P_{cu}	5.56 [W]
Iron losses P_{fe}	7.29 [W]
Voltage regulation α	0.05 [%]
Temperature rise	42 [°C]

3.11. OUTPUT FILTER INDUCTOR DESIGN

Due to the functionality of the converter, the frequency of the rectified voltage pulses is double than the switching frequency. Having a higher frequency makes it possible for the inductor size to be reduced. The waveform of the voltages and currents seen by the inductor in steady state are presented in Figure 38, where V_L represents the voltage across the inductor and i_L represents the inductor current.

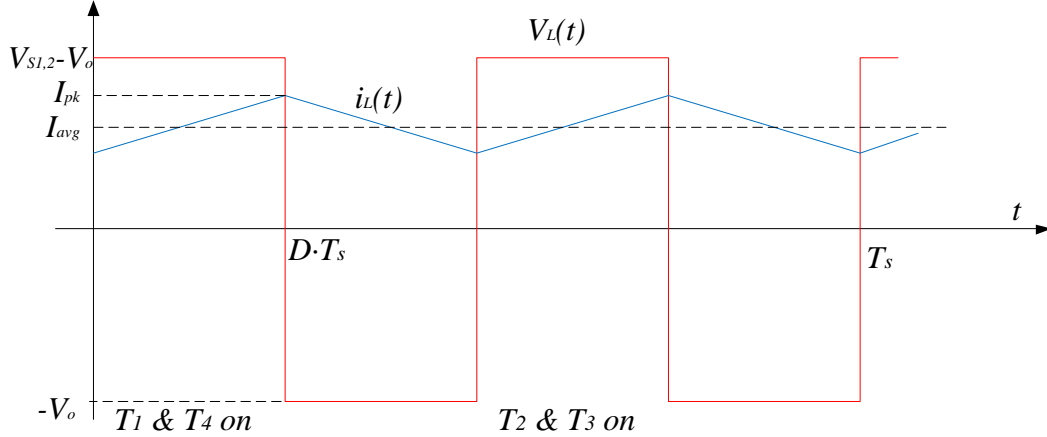


FIGURE 38: CURRENT (BLUE) AND VOLTAGE (RED) ACROSS THE OUTPUT FILTER INDUCTOR (SEE FIGURE 23)

For designing the inductor the material was chosen to be iron powder due to its relatively high saturation level and permeability curve. For selecting the core size each company has a graph from where a core can be selected based on the product of the desired inductivity and maximum current through the inductor. If the core does not meet the necessary requirements, a larger core is selected and the calculations are made again [25].

After selecting the core size, based on the inductance of one turn (A_L), the number of turns (N) can be calculated using equation (37), where L_{req} is the desired inductance which it is taken two times in order to take into consideration the fact that the induction of the core will decrease if the DC current is passed through the inductor [25].

$$N = \sqrt{2 * L_{req} / A_L} \quad (54)$$

In order to verify the inductivity, the DC magnetizing force can be calculated using equation (55) and from the permeability vs. magnetizing force graph of the material new permeability can be seen, thus finding out the induction during full load operation. In the presented equation I_{pk} represents the peak current through the inductor and l_m represents the magnetic path length of the core [25].

$$H = \frac{4\pi * N * I_{pk}}{l_m} [Oer] \quad (55)$$

If for the calculated magnetizing force the initial permeability is more than half of its initial value means that the inductance at rated current is the desired one, due to the fact that a factor of two was taken into account in calculation of number of turns. As for the wire dimension, the RMS value of the current is to be used and a current density (J) of $5 [A/mm^2]$ so the necessary area of the wire can be determined using equation (56) [25].

$$A_{wire} = \frac{I_{rms}}{J}, [mm^2] \quad (56)$$

By using the same procedure as for the transformer windings and in order to avoid the skin effect, the wire is composed by multiple smaller diameter strands (litz wire).

In order to calculate the losses, the magnetizing force is calculated for peak current and minimum current due to ripple below the highest load. This is done with equation (55). Based on flux density vs magnetizing force graph it can be found what the value for flux density variation B is. Based on this, the core losses can be calculated using equation (57) [25].

$$P_{fe} = B^2 f^{1.46} \quad (57)$$

For the copper losses, the resistance can be calculated as for the transformer design, and the dissipated power to be the same. By knowing this, the temperature rise can be calculated as in equation (58), where mW represents the total losses in milliWatts and A_t represents the surface area of the inductor [25].

$$\Delta T = \left[\frac{mW}{A_t} \right]^{0.8333} \quad (58)$$

In the end, the window utilization factor is calculated to verify if the window area is enough to fit the number of turns, by using formula (59), where W_{area} is the window area of the core [25].

$$k_u = \frac{A_{wire}}{W_{area}} \quad (59)$$

Based on the presented formulas, the inductor for the output filter can be calculated. The specifications are given in Table 14

TABLE 14: REQUIREMENTS FOR THE INDUCTOR USED AS OUTPUT FILER FOR THE 85 KW DC-DC CONVERTER

Average current I_{avg}	450 [A]
Ripple current I_{pk-pk}	16 [A]
Inductance L	50 [mH]
Frequency f	100 [kHz]

Based on multiple iterations two E114 cores were selected with the characteristics presented in Table 15.

TABLE 15: CORE SPECIFICATIONS FOR THE OUTPUT FILTER INDUCTOR FOR THE 85 KW DC-DC CONVERTER

Inductance of one turn A_L	235 [nH]
Magnetic path length l_m	22 [cm]
Volume V	262 [cm ³]
Surface area A_t	349 [cm ²]
Permeability μ	26
Window area W_{area}	12.32 [cm ²]

The values for the inductor that resulted from the formulas are presented in Table 16.

TABLE 16: FINAL INDUCTOR CALCULATED VALUES FOR THE 85 KW DC-DC CONVERTER

Number of turns N	21
Inductance at rated current L	49 [μ H]
Number of strands S_n	716
Strand diameter	0.4 [mm]
Copper losses P_{cu}	0.16 [W]
Core losses P_{fe}	6.3 [W]
Temperature rise ΔT	12 [°C]

In order to verify the functionality of the converter topology, an inductor is to be designed for a small scale converter (10 kW). The requirements for the inductor are presented in Table 17.

TABLE 17: REQUIREMENTS FOR THE 10 KW INDUCTOR USED AS OUTPUT FILER FOR THE DC-DC CONVERTER

Average current I_{avg}	73 [A]
Ripple current I_{pk-pk}	16 [A]
Inductance L	50 [mH]
Frequency f	100 [kHz]

Based on multiple iterations two E80 cores were selected with the characteristics presented in Table 18.

TABLE 18: CORE SPECIFICATIONS FOR THE 10 KW OUTPUT FILTER INDUCTOR

Inductance of one turn A_L	190 [nH]
Magnetic path length l_m	20 [cm]
Volume V	72 [cm ³]
Surface area A_t	42 [cm ²]
Permeability μ	60
Window area W_{area}	11.1 [cm ²]

The values for the inductor that resulted from the formulas are presented in Table 19.

TABLE 19: FINAL INDUCTOR CALCULATED VALUES FOR THE 10 KW PROTOTYPE

Number of turns N	23
Inductance at rated current L	48 [μH]
Number of strands S_n	116
Strand diameter	0.4 [mm]
Copper losses P_{cu}	0.014 [W]
Core losses P_{fe}	10.8 [W]
Temperature rise ΔT	9 [$^{\circ}C$]

The designed inductor was measured in the laboratory using an impedance analyzer and it had a value of 110 μH at 2 kHz , but the value decreased to 68 μH for 100 kHz . Future measurements under DC bias will be performed to ensure that the design requirements are respected.

3.12. SUMMARY

In this chapter modeling of all the system components, design of magnetics and design of the controllers were presented, with different levels of detail. For the wind turbine, generator and electrolysis system, simplified models were made so that multiple test cases can be evaluated through simulations.

In the power electronics system, the models were designed in PLECS, using the components in the software's library. In the case of the DC-DC converter, due to the need of designing the power electronics, also thermal modelling is implied. The thermal data for the modules was given by the manufacturers of the devices and it was implemented in PLECS using a look-up table. Two commercially available devices were chosen based on their power capabilities and loss characteristics (on-state resistance, turn-on and turn-off losses), after which their performances were evaluated in a thermal simulation. The evaluation has shown that the SiC transistors from Wolfspeed would be the best option so they were used for further simulations. Based on the number of devices required and the initial efficiency evaluation the optimal topology for the DC-DC converter has proved to be the full bridge with high frequency transformer and rectifier, so this topology is selected to be used further in the simulations.

For the current controller design for AC-DC converter a maximum overshoot of 10% was desired with a settling time of less than 10 *ms* and the speed controller a settling time no greater than 5 s was desired and an overshoot of 10%, requirements which were respected. The feed forward terms ensure the decoupling of the *d* and *q* components of the current and make the control faster.

In case of the DC-DC converter, the control is relatively simple, being the same as for a Buck converter so the 5 *ms* desired settling time was easily achieved for the current control loop while having an overshoot of less than 10%. For the DC-link voltage control loop a settling time of less than 80 *ms* is achieved, which was desired.

The electrolysis system is modeled as a diode with a high on state voltage and a resistor in series. A linear interpolation for the Current-Voltage curve was used to get the values characteristic for the electrolysis cell modeled.

In the next chapter simulation results will be presented in order to verify and validate the modeling of the components and the design of the control loops.

CHAPTER 4. SIMULATION RESULTS

4.1. OVERVIEW

As presented before, the system is composed from a wind turbine connected using a PMSG controlled by a AC-DC converter. This system is designed so it draws from the wind the maximum allowed power. This energy is then taken by a DC-DC converter and fed into an electrolysis system so that the DC-link voltage remains constant in order to ensure also a power balance.

Based on the models presented in the previous chapter, simulations were done in order to validate the models and observe the behavior of the system under different conditions. To ensure that the models are accurate, the simulations were divided in several distinctive parts: the generator - AC-DC converter system is analyzed first, after which the wind turbine is added in order to have the complete wind turbine – generator – rectifier system. As the switching frequency of the DC-DC converter is very high compared to the AC-DC one, introducing this one in the simulation would have increased dramatically the computational time, thus it was simulated separately.

The main values of the components used in simulation are presented in Table 20.

TABLE 20: SIMULATION PARAMETERS

Wind turbine	
Wind turbine rated power	250 [kW]
Wind turbine nominal wind speed	12.2 [m/s]
Generator	
Rated voltage	465 [V]
Rated current	1043 [A]
AC-DC converter	
DC-link voltage	780[V]
Switching frequency	3 [kHz]
Control frequency	6 [kHz]
DC-DC converter	
Inductor size	49 [μ H]
Capacitor size	104[μ F]
Switching frequency	50 [kHz]
Transformer ratio	1:3:3
Paralleled converters	3
Electrolysis system	
Zero current voltage	130 [V]
Resistance	0.048[Ω]

For the controllers, the parameters used are presented in Table 21.

TABLE 21: CONTROLLER PARAMETRS USED IN SIMULATIONS

AC-DC converter current controller	
K_p	13.5
T_i	0.04
AC-DC converter speed controller	
K_p	5600
T_i	4
DC-DC converter current controller	
K_p	9.1e-5
T_i	0.001
DC-DC converter DC-link voltage controller	
K_p	0.27
T_i	0.1

The simulation block diagram is presented in Figure 39 for the first two cases. Due to the fact that the DC-DC converter is supposed to keep the DC-link voltage constant, for simulation purposes a DC voltage power supply was used instead as a model.

The MPPT was designed to provide the reference speed so the maximum output power from the wind turbine is drawn, based on the wind speed, which is assumed to be known in this case. As for the modulator, a simple space vector modulation strategy was used.

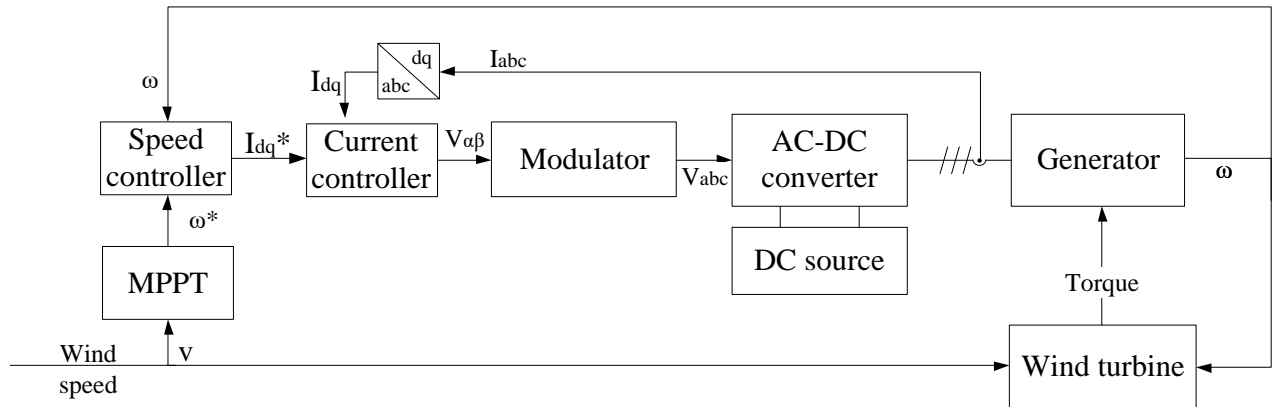


FIGURE 39: OVERALL SIMULATION BLOCK DIAGRAM FOR WIND TURBINE-GENRATOR-AC-DC CONVERTER SIMULATION

4.2.GENERATOR AND FIELD ORIENTED CONTROL STRATEGY SIMULATIONS

For this system verification, the wind turbine was replaced by a constant torque or a variable one depending on the test case. The same is true for the rotational speed reference. Due to the fact that the speed loop is the outer loop for the current control, the latter was tested first in order to ensure a proper design of the controllers. A step response in both current components I_d and I_q is presented in Figure 40. The current settling time is 10 ms and it has an overshoot less than 10%. Due to the decoupling terms, each current component can be controlled individually ensuring that a change in one of the components has a small influence on another if the decoupling terms are properly designed.

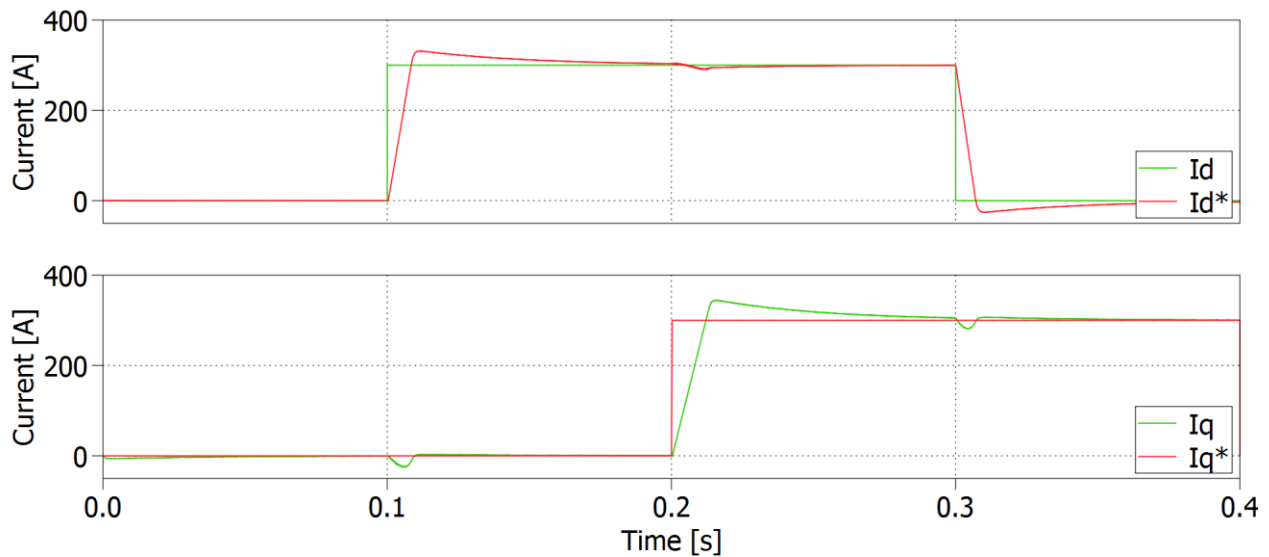


FIGURE 40: CURRENT CONTROLLER RESPONSE FOR GENERATOR CONTROL

In order to verify if the system is stable, the response for a change in reference speed has been analyzed (Figure 41) and also the speed response for a perturbation in the torque applied to the generator (Figure 44). The generator currents and the voltages generated by the AC-DC converter were also analyzed for both cases.

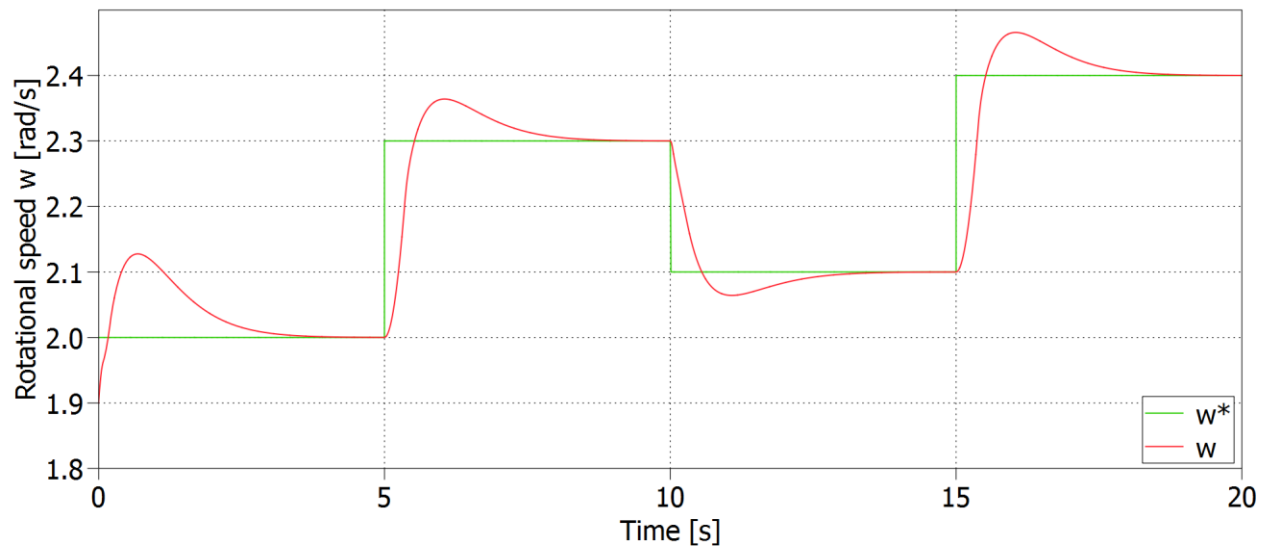


FIGURE 41: STEP RESPONSE IN REFERENCE SPEED OF THE GENERATOR CONTROL FOR A LOAD TORQUE OF HALF THE RATED ONE

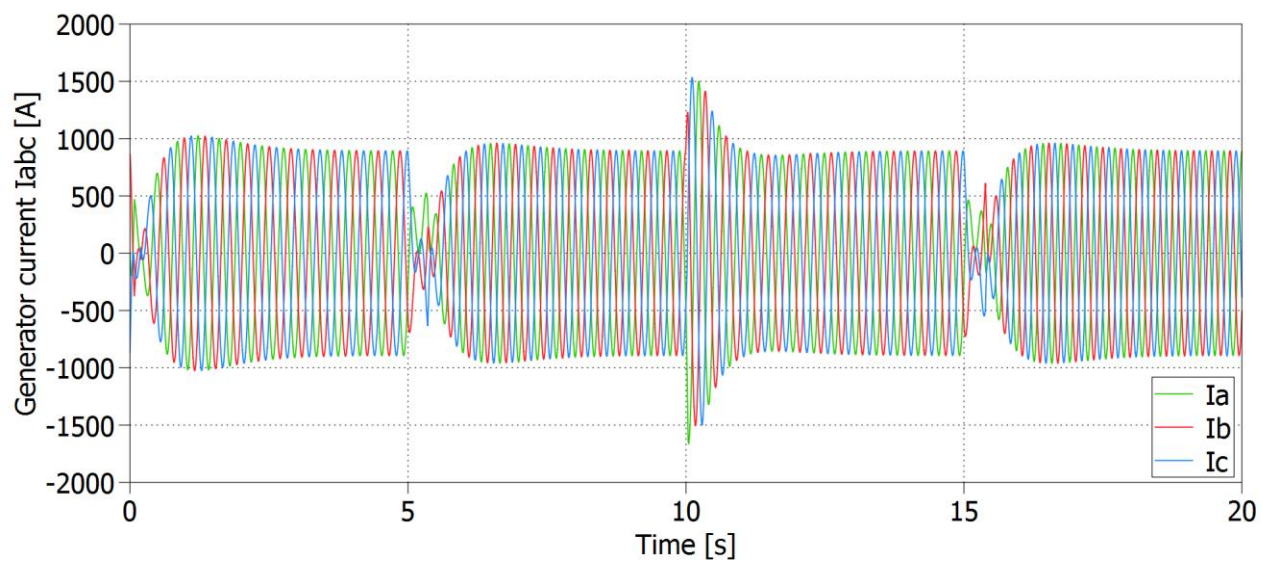


FIGURE 42: GENERATOR CURRENTS UNDER THE VARIATION OF THE GENERATOR SPEED PRESENTED IN FIGURE 41

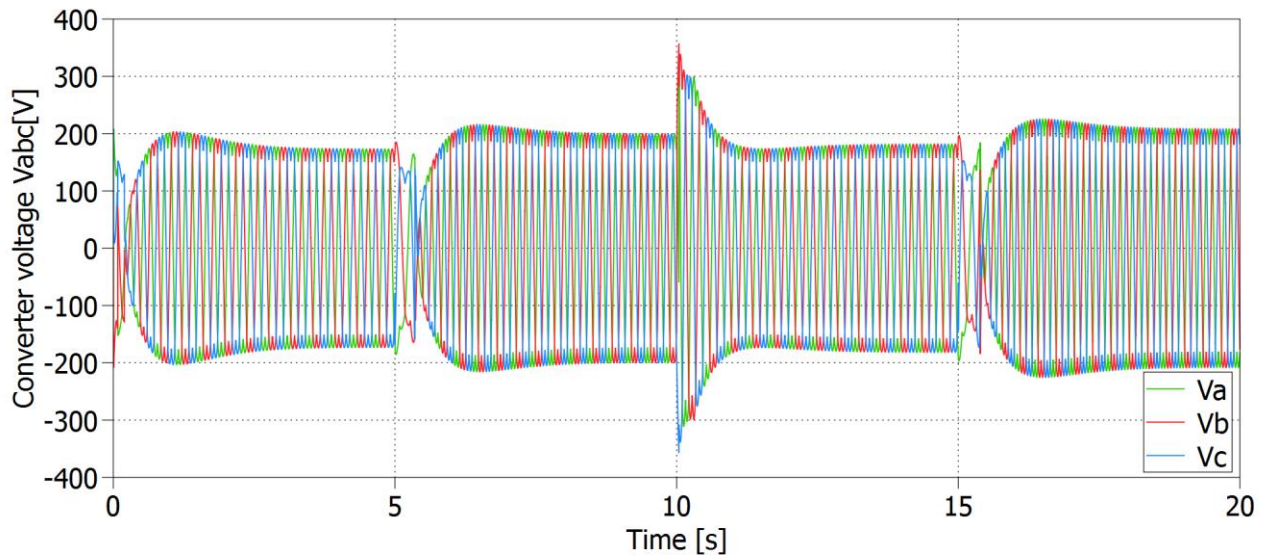
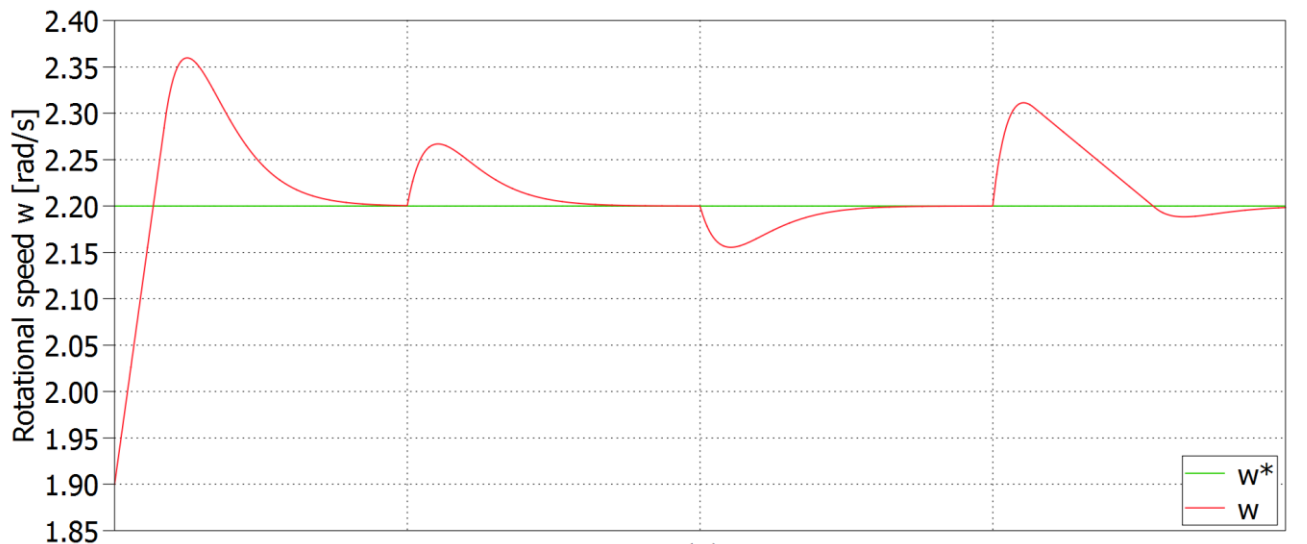


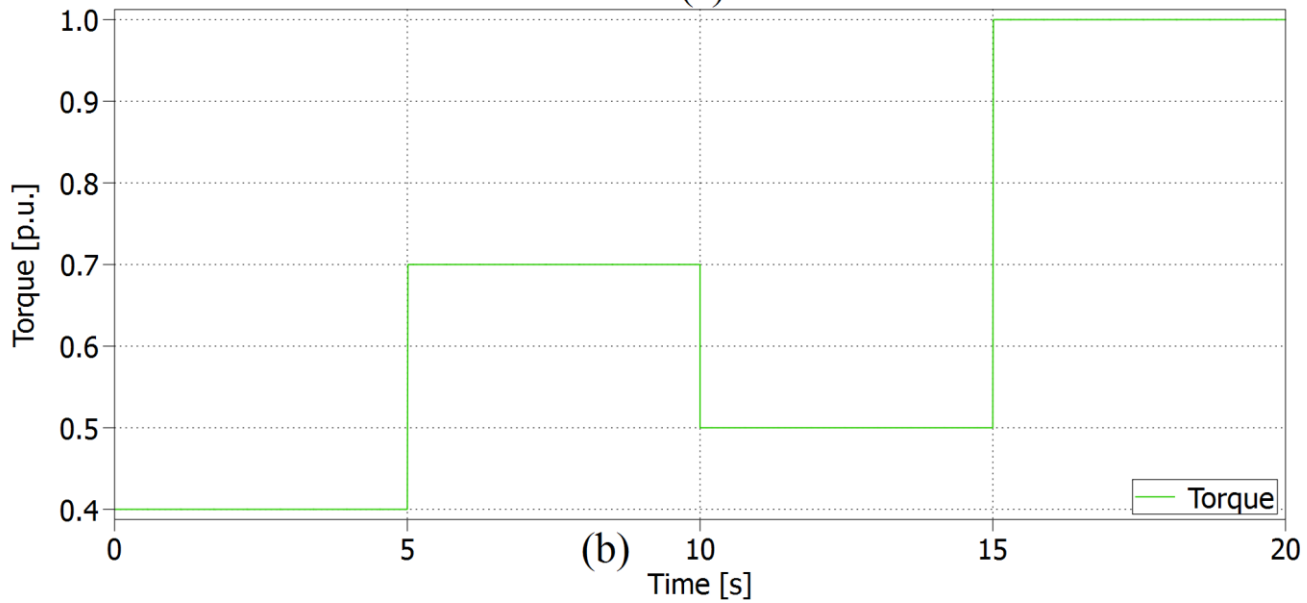
FIGURE 43: GENERATOR VOLTAGES UNDER VARIATION OF THE GENERATOR SPEED PRESENTED IN FIGURE 41

As expected from the controller design stage, for a step in the reference speed, the response time is around a half a second, the settling time is 3 seconds and the overshoot is close to 22%. For a system like this, the results are satisfactory, as a system with such a high time constant, instead of giving the reference as step, it can be given as a ramp, which will minimize the effect of the overshoot, thus not causing any problems. As for the current, the peaks can be also smoothed if the control speed is reduced and a ramp signal is used instead of step for changes in reference. The speed of the system can be improved if the limitations in the reference current would be larger, but this may cause higher current spikes which are not acceptable for the protection system. As it can be observed in Figure 42, in the presented case the current does not exceed the maximum allowed value of 1700 A.

As for the speed response in the case of change in torque it can be observed that no current or voltage spikes are present. The speed changes its value, but returns to the reference one in around 3 seconds.



(a)



(b)

FIGURE 44: GENERATOR SPEED (A) UNDER CHANGE IN TORQUE APPLIED TORQUE (B)

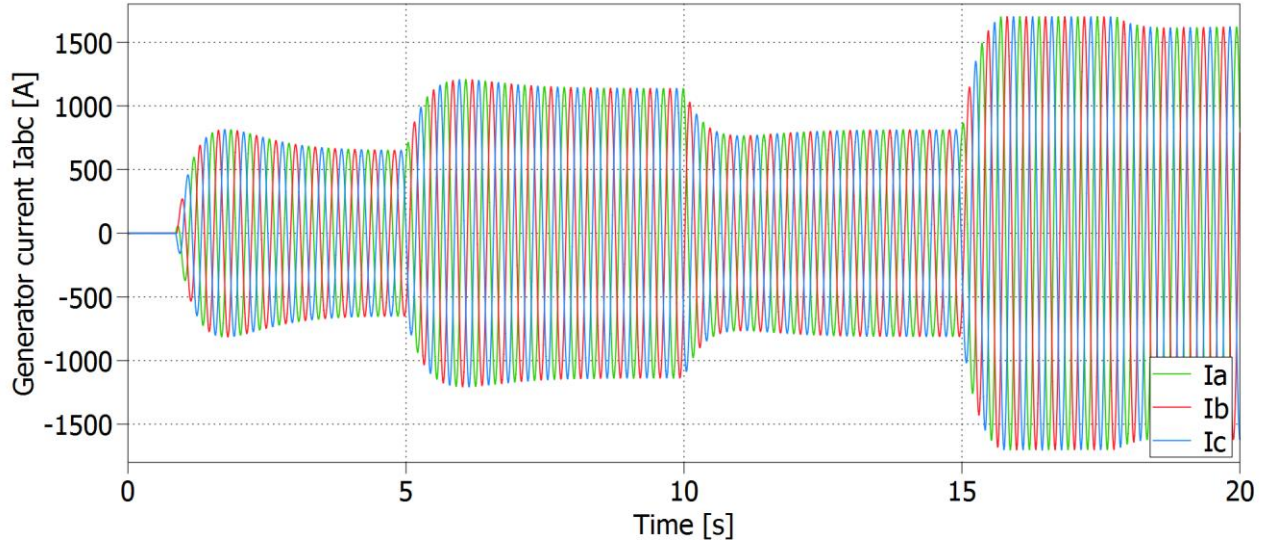


FIGURE 45: GENERATOR CURRENTS UNDER VARIATION OF GENERATOR TORQUE SHOWN IN FIGURE 44

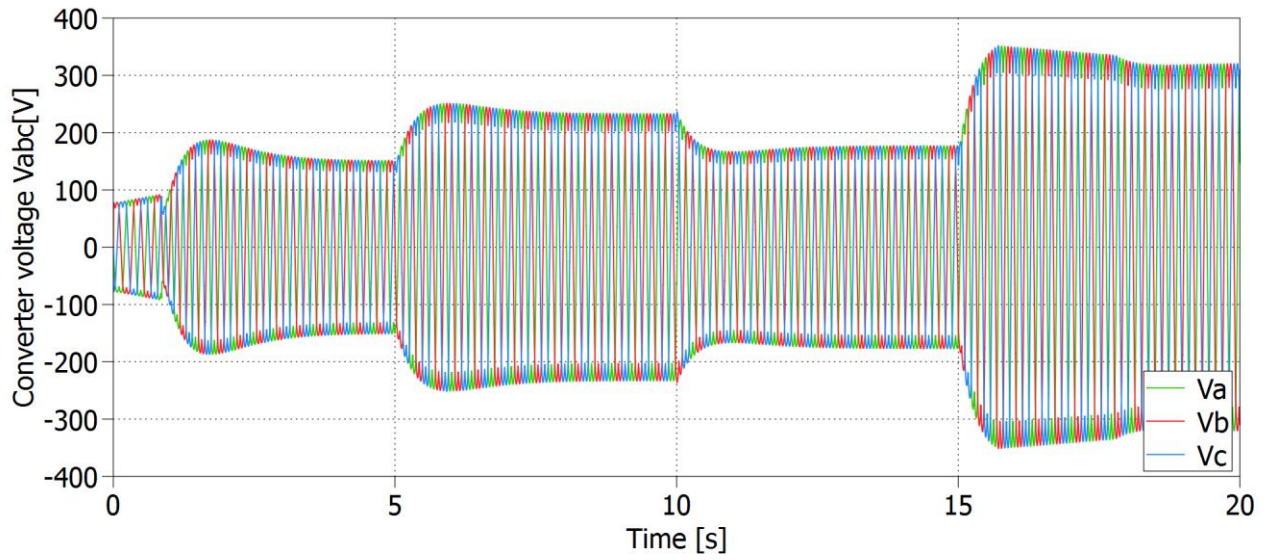


FIGURE 46: GENERATOR VOLTAGE UNDER VARIATION OF GENERATOR TORQUE SHOWN IN FIGURE 44

4.3. WIND TURBINE – GENERATOR – AC-DC CONVERTER SYSTEM SIMULATION

For this part, the schematic of the system given in Figure 39 is used for simulation. The wind profile was chosen as a stair sequence with values between 10 and 13 m/s. The values were chosen around the rated value in order to observe that the limitations used in the control will not affect the behavior of the system. To ensure that the output power does not surpass the rated value of the generator, a pitch control strategy can be used and is implemented. Because the main focus on this project is on the power electronics side, the pitch control was implemented using a look-up table based on the wind speed.

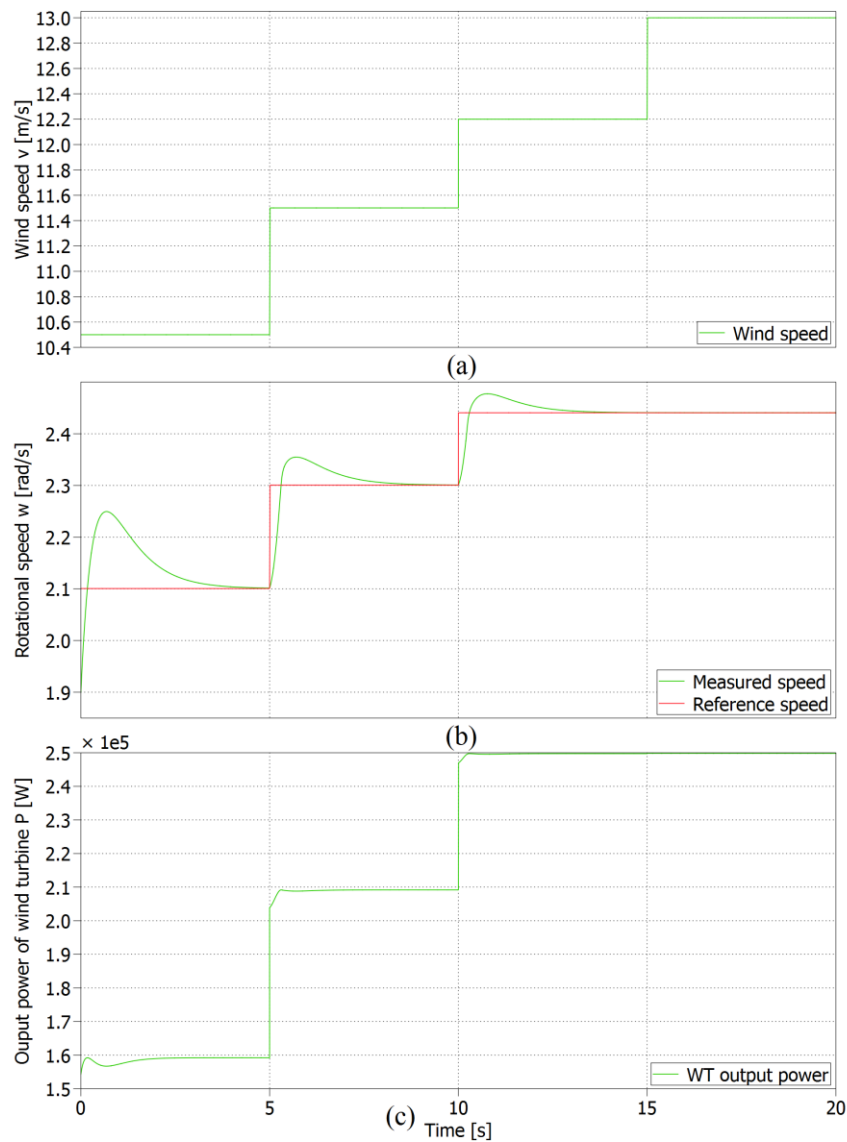


FIGURE 47: WIND SPEED VARIATION (A), ROTATIONAL SPEED OF THE WIND TURBINE (B), OUTPUT POWER OF THE WIND TURBINE (C)

As it was desired, the generator speed reference changes according to the wind speed in order to achieve maximum power point tracking and within 3 seconds the actual speed achieves the reference value. Due to the limitations in the PI controller output, there are no large current/voltage spikes, as it can be observed in Figure 48 and Figure 49. The output power of the AC-DC converter changes according to the wind turbine power in order to achieve the desired rotational speed and the simulation results can be seen in Figure 50. Due to the high increase in converter voltage during transients, a short spike is seen in the output power.

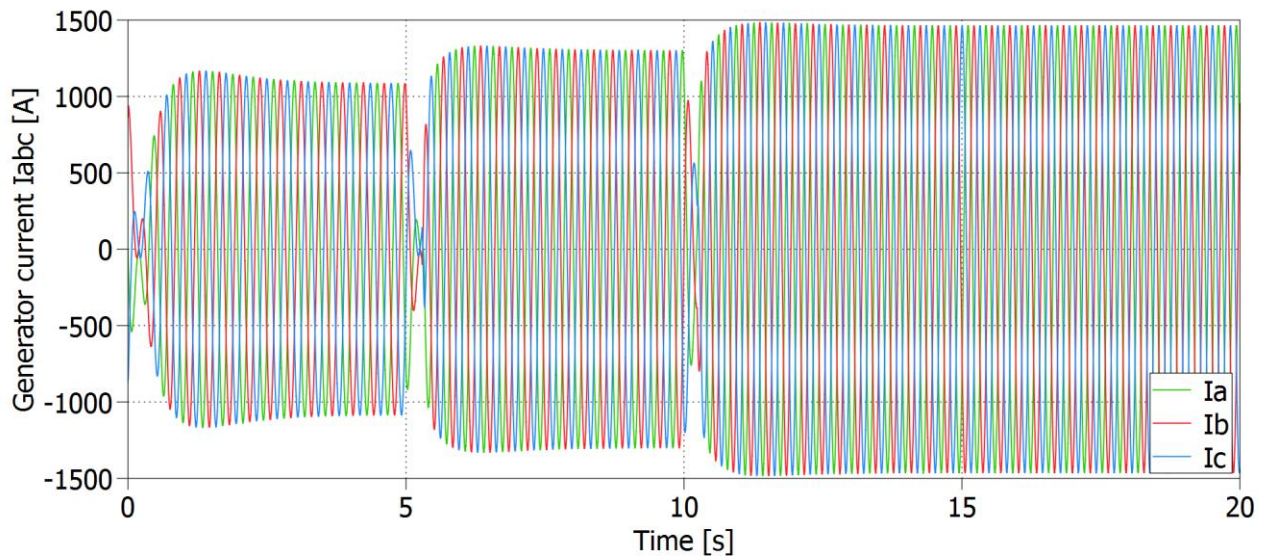


FIGURE 48: GENERATOR CURRENT UNDER VARIATION OF WIND SPEED SHOWN IN FIGURE 47

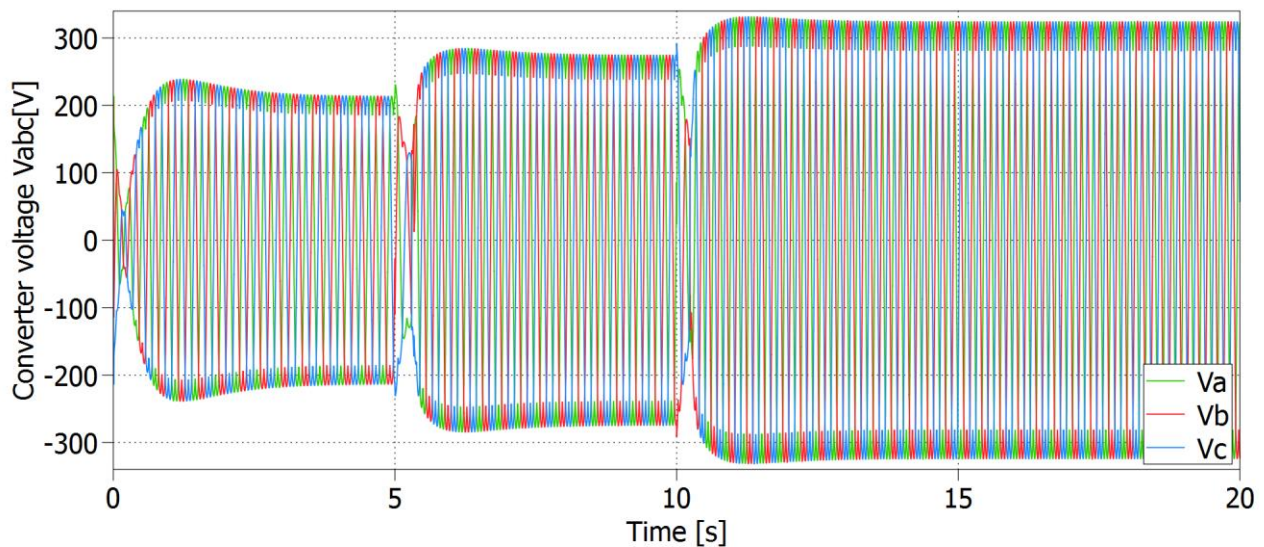


FIGURE 49: GENERATOR VOLTAGE UNDER VARIATION OF WIND SPEED SHOWN IN FIGURE 47

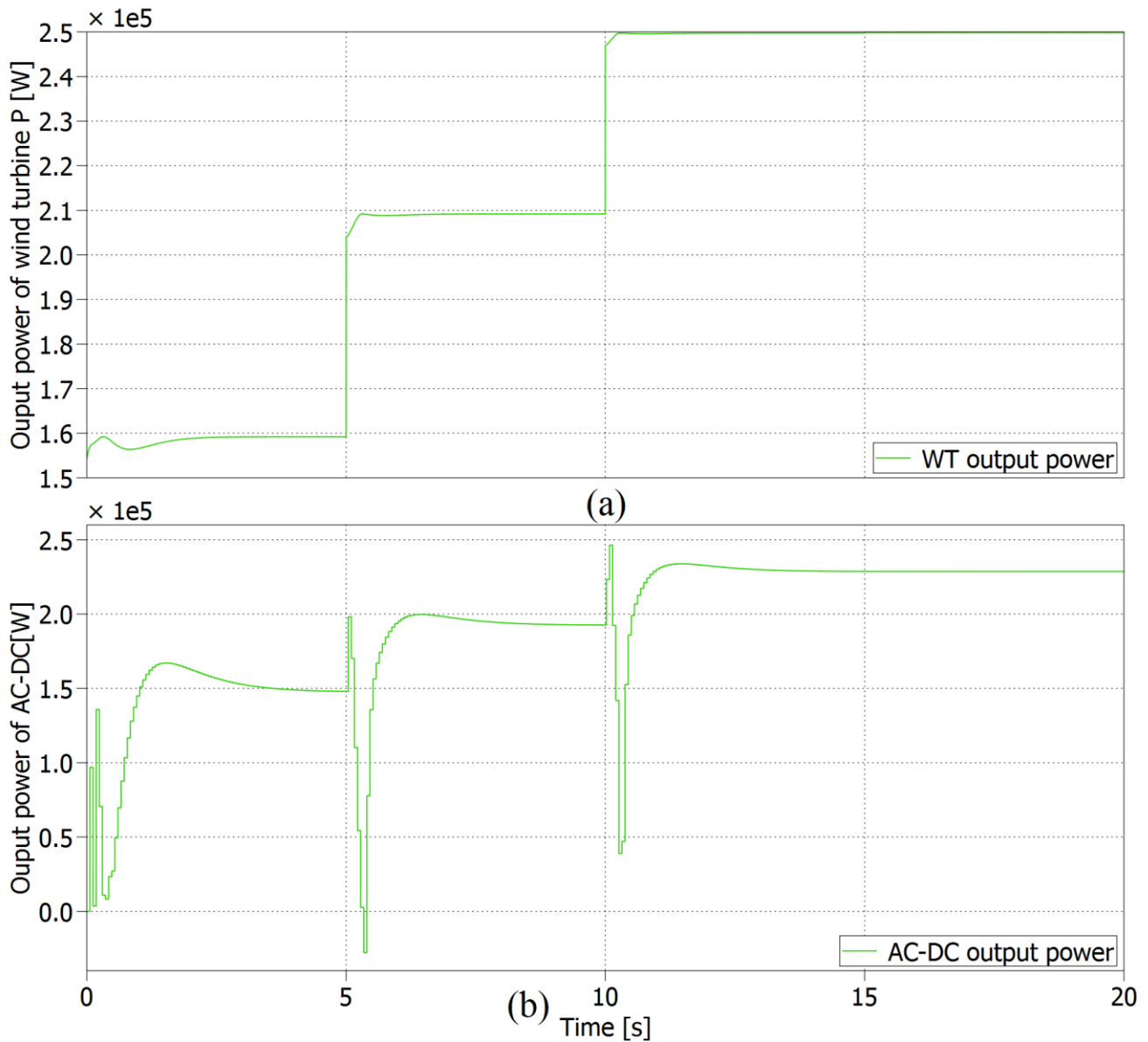


FIGURE 50: OUTPUT POWER OF THE WIND TURBINE (A) AND OUTPUT POWER OF THE AC-DC CONVERTER (B) FOR WIND SPEED VARIATION SHOWN IN FIGURE 47

As previously mentioned, the DC-DC converter simulation is made separately due to the fact that adding all the components in a simulation would have made it impossible for the simulation program to run it as different time-scales are present. In order to verify the functionality of the system, the DC-DC converter is tested using the same approach as in the AC-DC part.

4.4.DC-DC CONVERTER SIMULATION

As it was mentioned in the design of power electronics chapter, the DC-DC converter is composed of 3 paralleled converters, each one using a full bridge, a high frequency transformer, a rectifier and an output filter. Each one of the converters is connected to the same DC-link and the same load, and they are controlled like current sources. The reference current comes from the DC-link voltage control loop, as it is presented in Figure 51, where the current control and the DC-link voltage both consist simply as PI controllers for which the tuning was presented in the previous chapter (see subchapter 3.7).

To ensure proper functionality of the system, simulations for the DC-DC conversion were divided into two main stages. At first only one converter is tested, starting with the current control loop, followed by the Dc-link voltage control loop; after which the whole system with 3 DC-DC converters is simulated as shown in Figure 52.

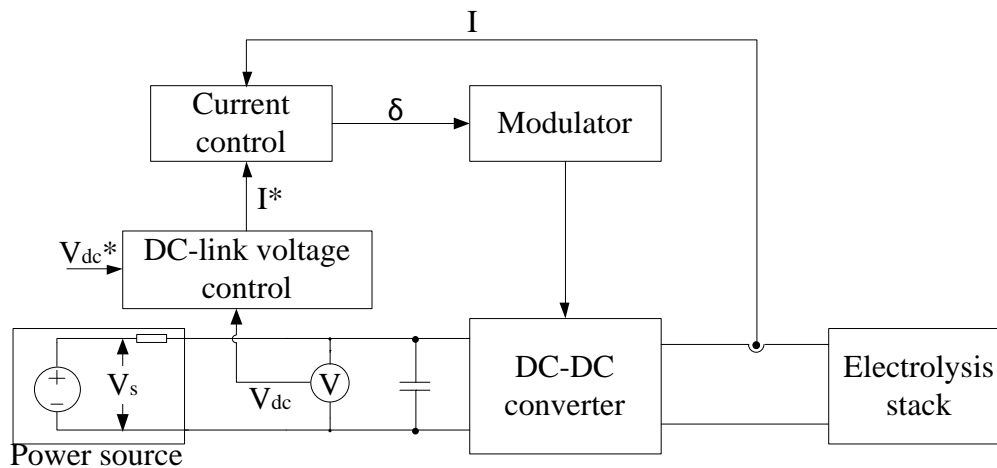


FIGURE 51: DC-DC CONTROL BLOCK DIAGRAM FOR ONE CONVERTER

For the current control verification, the diagram from Figure 51 is slightly modified. The power source is being replaced with a DC voltage source and the current reference is not given by the DC link voltage controller, but is given as an external signal. The results can be seen in Figure 53. As it can be observed, the response time is around 25 ms when it switches from zero due to the integrator term in the PI which increases significantly until the output voltage reaches the minimum conduction voltage required by the Electrolysis stack to be in conduction mode. This dynamic response can be improved by adding a feed-forward term after the PI controller, but it is not necessary due to the fact that for starting the electrolysis system a slow and gradual increase in current is needed. An overshoot of 4% is present in the change in the current, which is acceptable considering the response time of 1 ms.

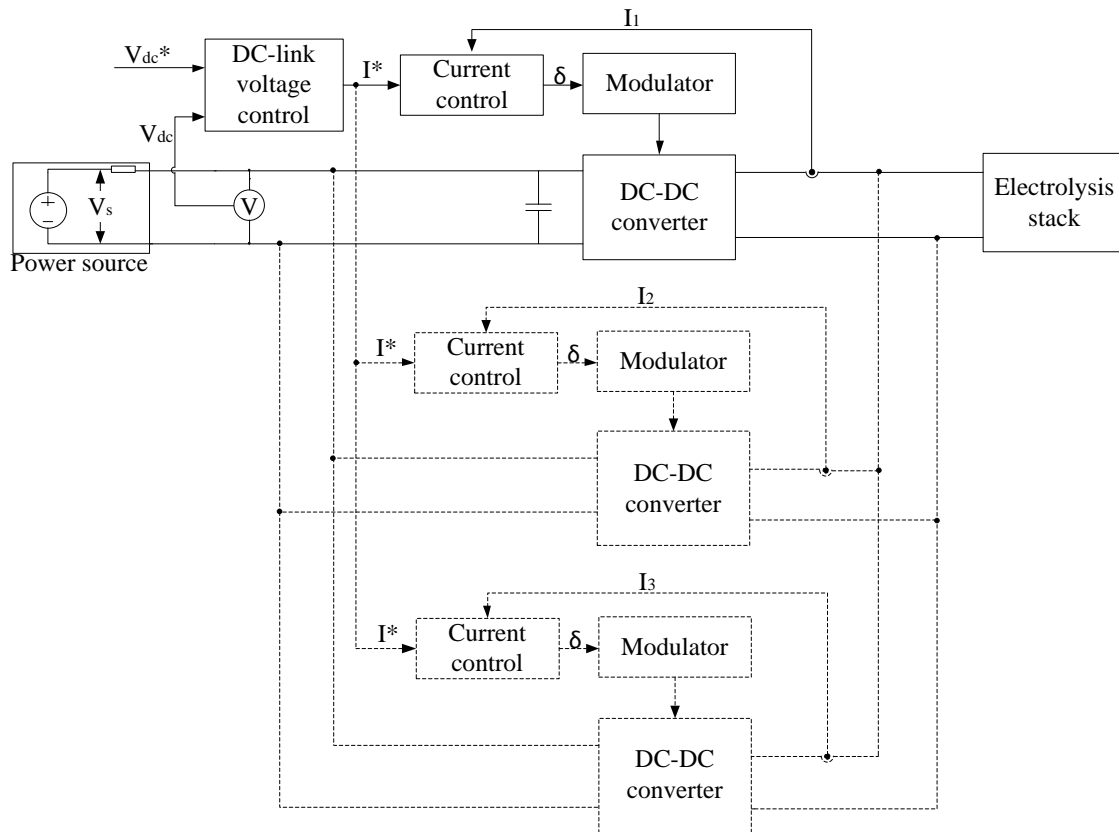


FIGURE 52: DC-DC CONTROL BLOCK DIAGRAM FOR 3 INTERLEAVED CONVERTERS

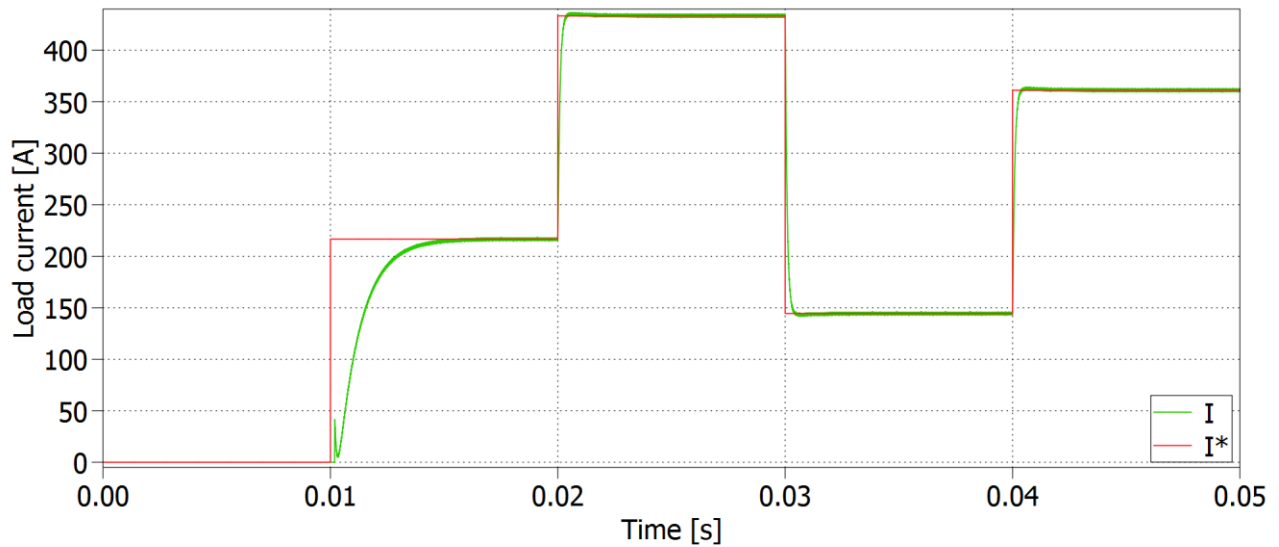


FIGURE 53: REFERENCE LOAD CURRENT (RED) AND MEASURED LOAD CURRENT (GREEN)

For the DC-link voltage control loop verification, the schematic shown in Figure 51 is used. The input power is changed using a variable voltage source V_s in series with a 0.1Ω resistor in order to simulate the effect of the AC-DC converter. The DC-link voltage response can be seen in Figure 54 and the output current can be observed in Figure 55. As it is expected, the voltage overshoot is present due to the change in input power, but the DC-link voltage is regulated at the desired value in 0.2 seconds.

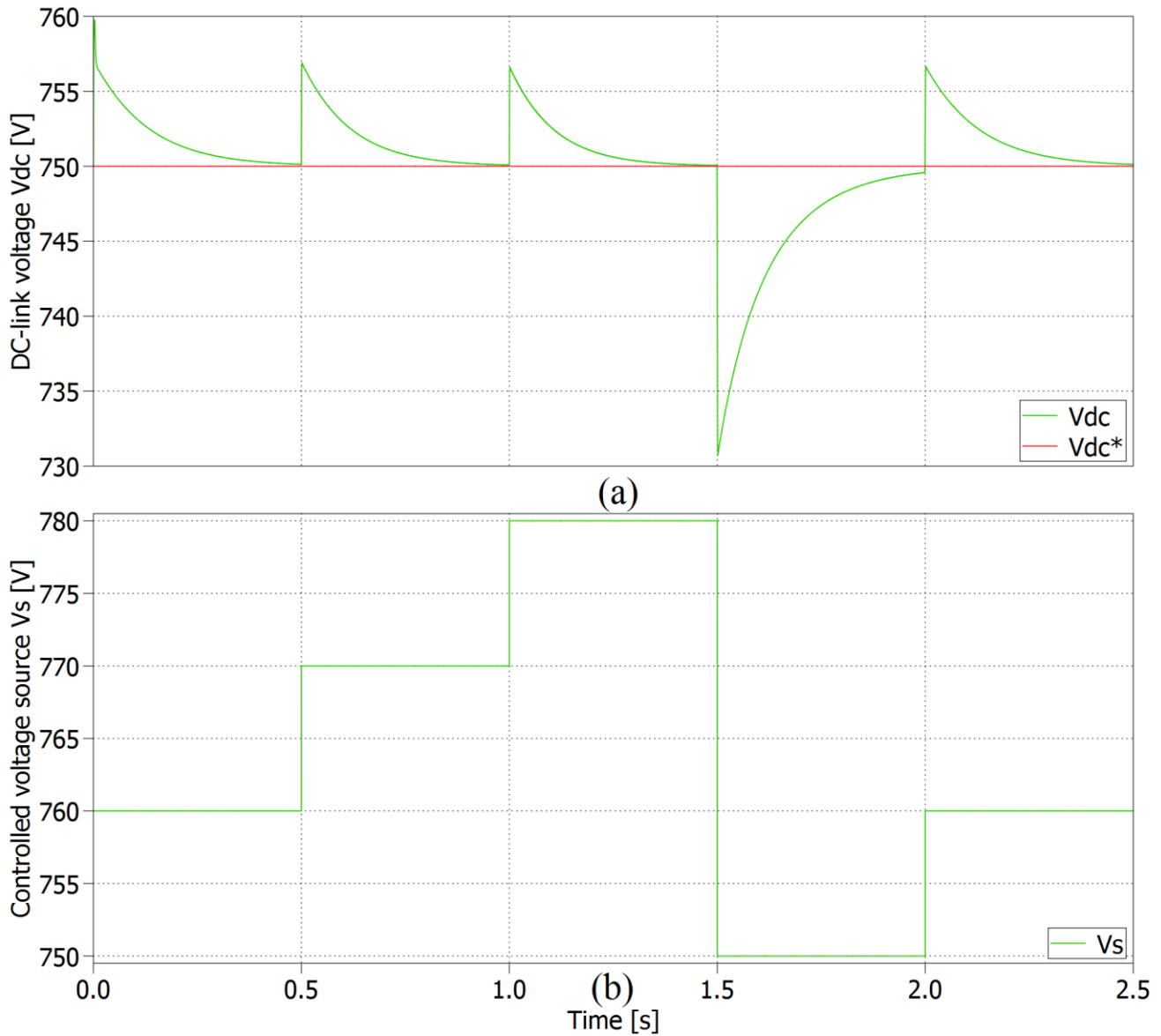


FIGURE 54: DC LINK VOLTAGE (A) AS A RESPONSE TO VARIATION OF VOLTAGE OF THE CONTROLLED VOLTAGE SOURCE V_s (B)

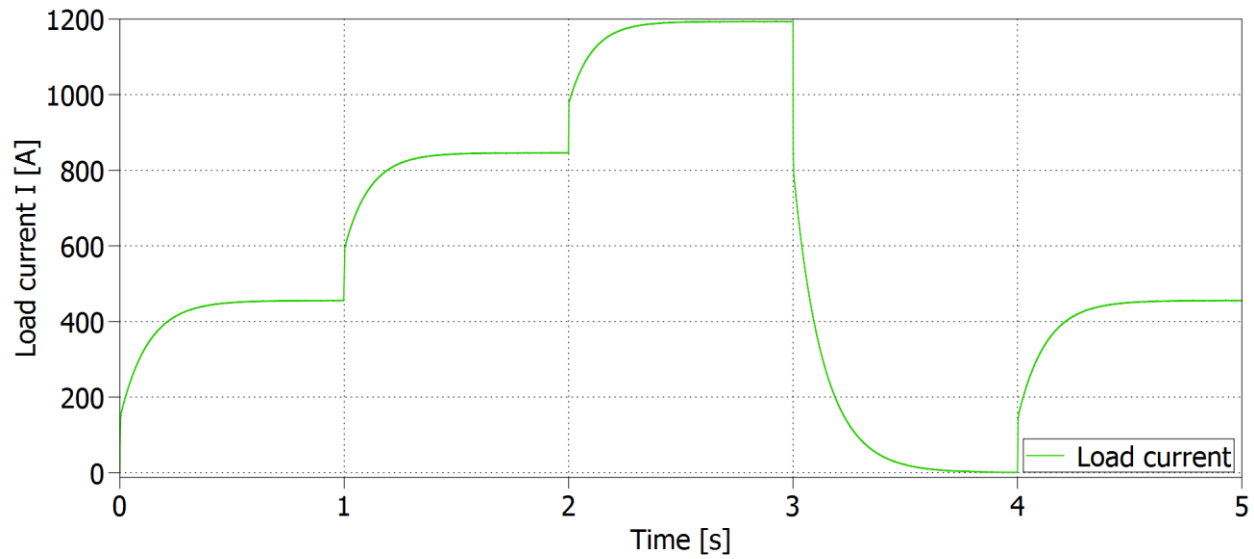


FIGURE 55: LOAD CURRENT CORRESPONDING TO THE CHANGES IN INPUT POWER CAUSED BY THE VARIATION OF VOLTAGE OF THE CONTROLLED VOLTAGE SOURCE V_s

For the case where three converters are used in parallel, the reference current is given by the DC-link voltage control block, and is divided equally between the three converters. The Dc-link voltage response of a change in the input power is shown in Figure 56 and the current corresponding to that change for each converter is shown in Figure 57.

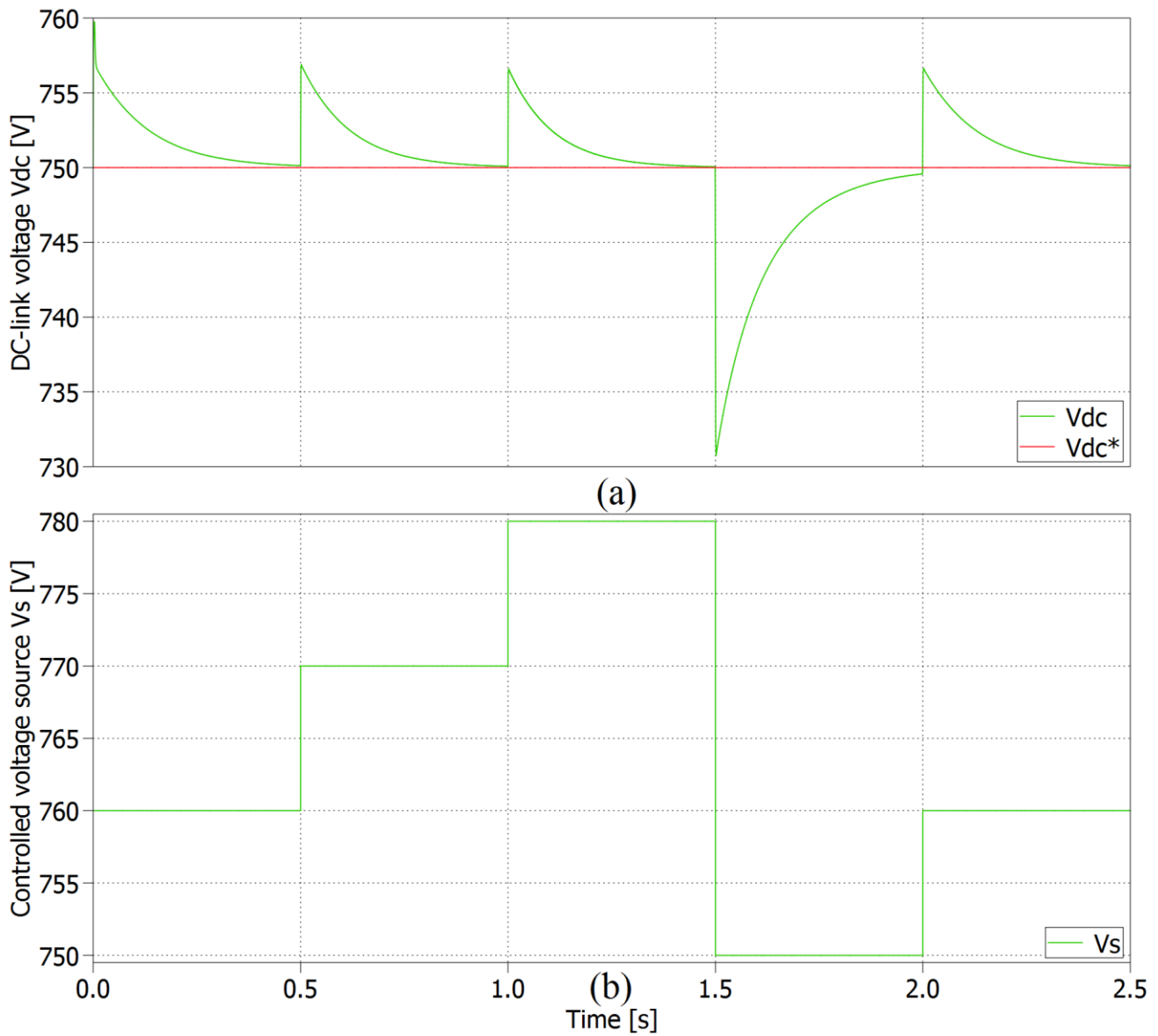


FIGURE 56: DC LINK VOLTAGE (A) CAUSED BY VARIATION IN THE VOLTAGE OF THE CONTROLLED VOLTAGE SOURCE V_s (B) FOR THE CASE WITH THREE DC-DC CONVERTERS INTERLEAVED

As all of the converters behave in the same way there is no visible difference in their currents. In Figure 58 the inductor current of each converter can be seen. The three converters are interleaved, so the resulting current ripple is significantly reduced compared to each converter ripple, as it can be observed in Figure 59.

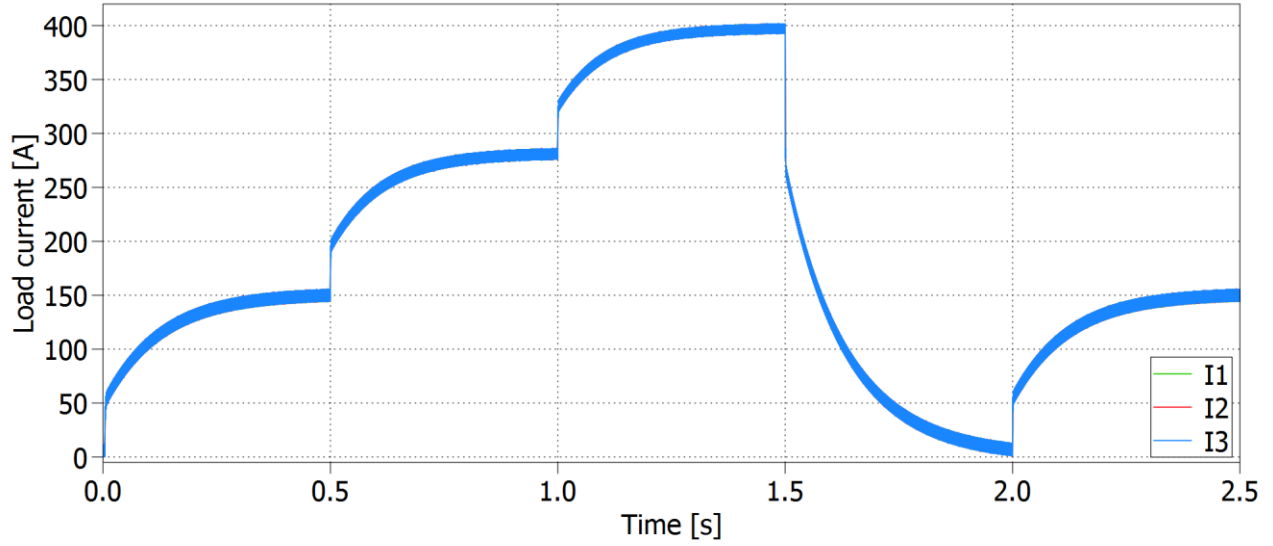


FIGURE 57: CONVERTER CURRENTS CORRESPONDING TO THE CHANGES IN INPUT POWER AS SHOWN IN FIGURE 56 B

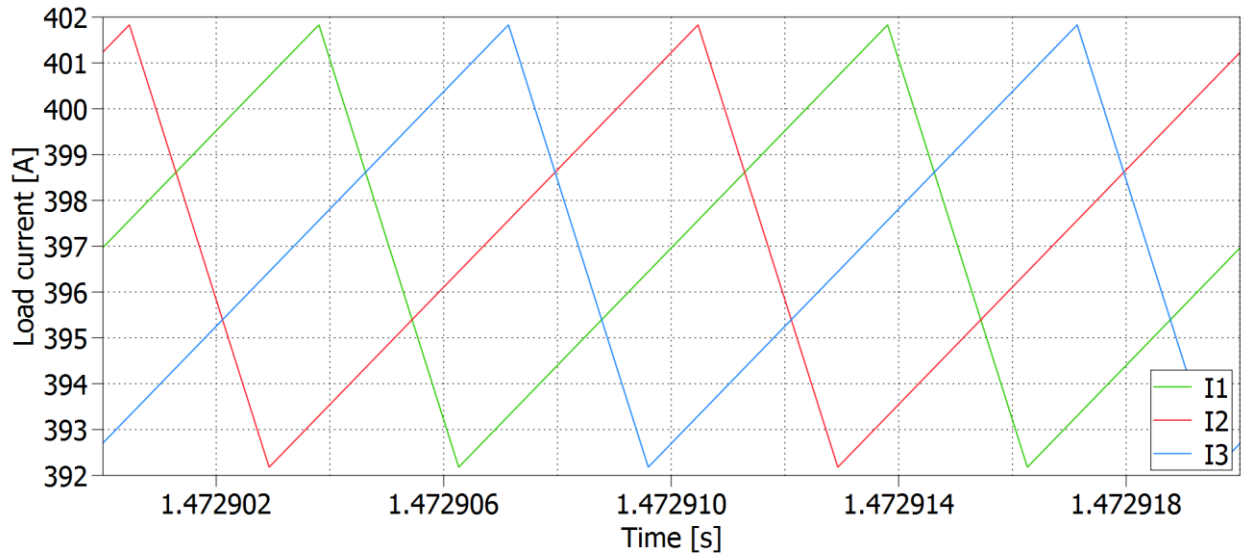


FIGURE 58: INDUCTOR CURRENTS OF EACH CONVERTER FOR THE CASE WHERE THREE INTERLEAVED DC-DC CONVERTERS ARE USED

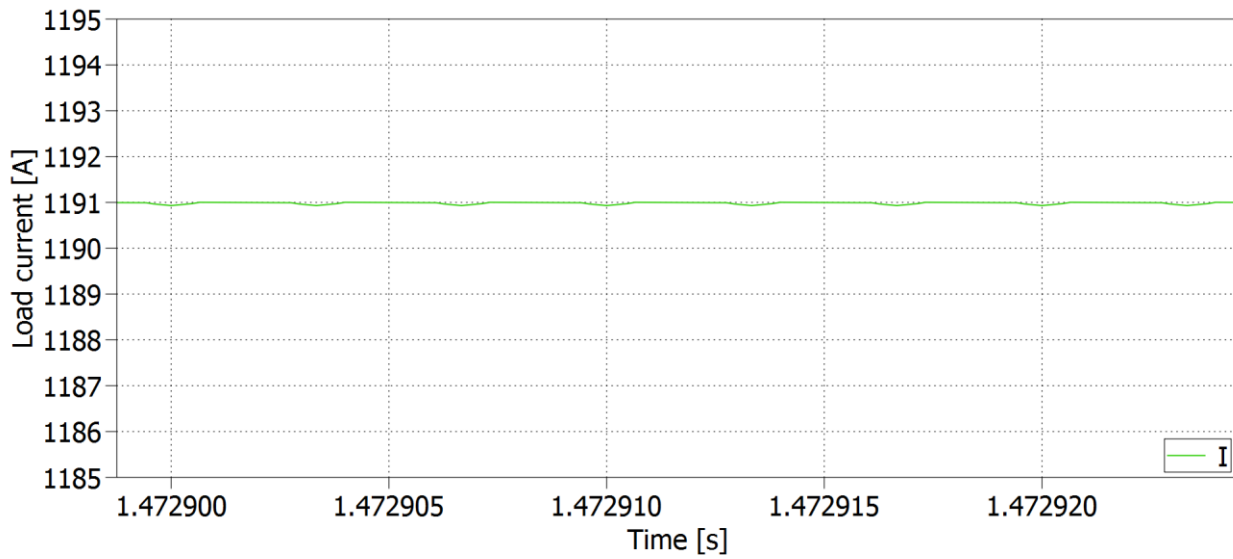


FIGURE 59: LOAD CURRENT IN THE CASE OF THE THREE CONVERTERS INTERLEAVED

In order to analyze the thermal response of the transistors, a thermal simulation was done considering full load operation (rated current and rated DC-link voltage). The junction temperature of the transistor in Figure 60 and the steady state losses can be seen in Figure 61.

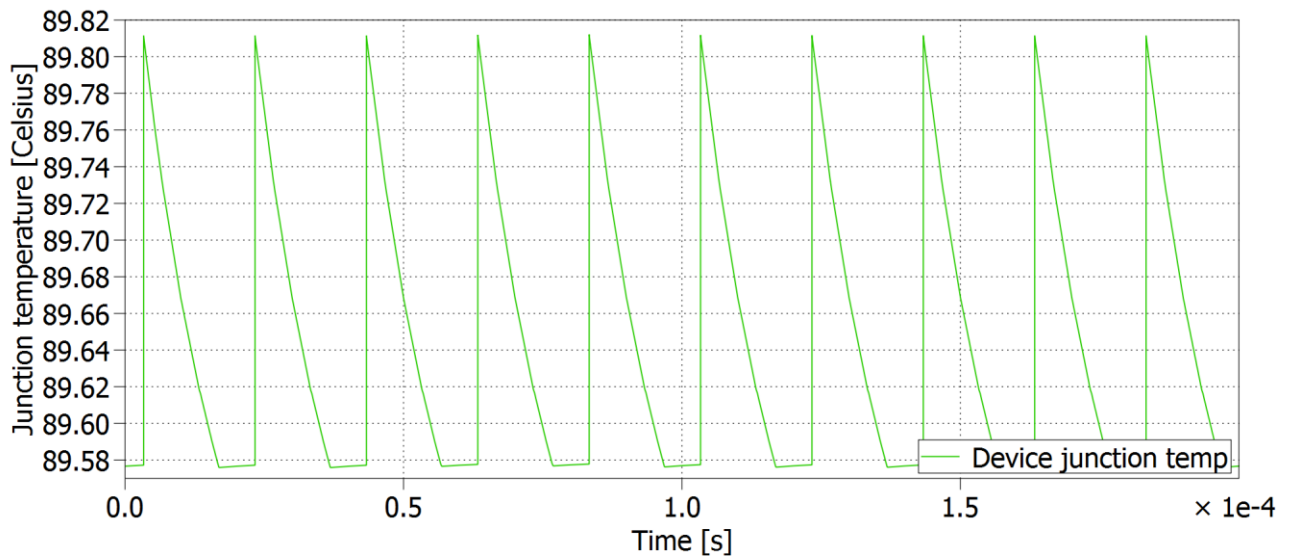
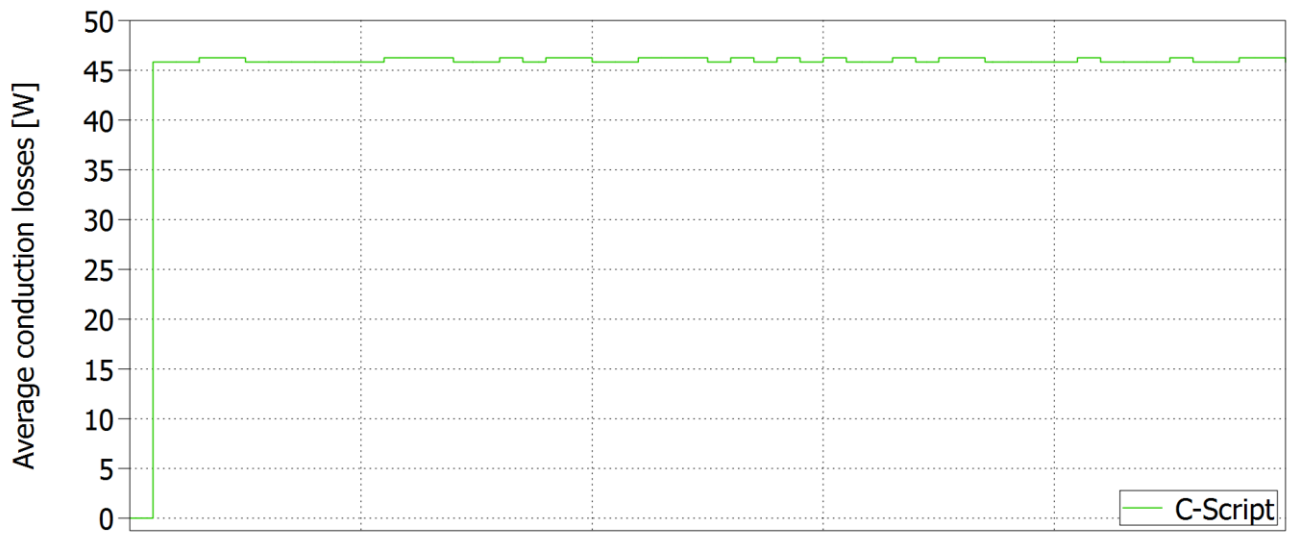
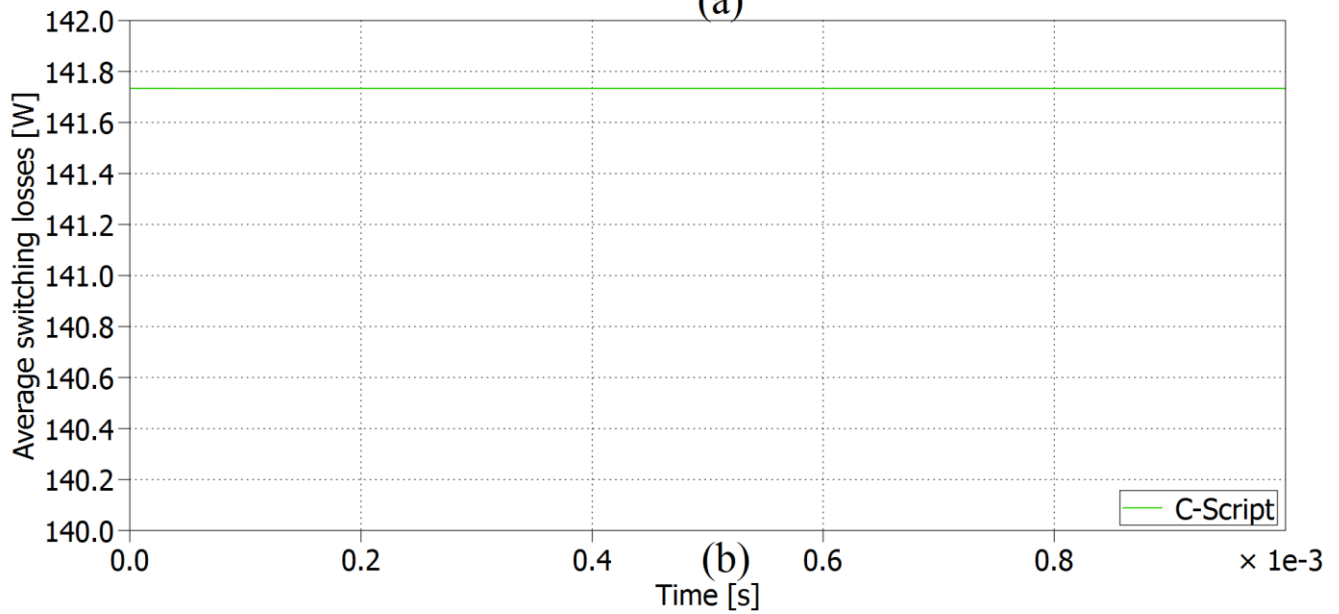


FIGURE 60: MOSFET JUNCTION TEMPERATURE IN STEADY STATE OPERATION CONSIDERING THE AMBIENT TEMPERATURE AT 50 DEGREES CELSIUS



(a)



(b)

FIGURE 61: MOSFET AVERAGE LOSSES IN STEADY STATE OPERATION, CONDUCTION (A) AND SWITCHING (B)

4.5. SUMMARY

In this chapter simulations of all the models were presented. Initially for each system the inner current loop was tested to verify the response, after which the outer loop was tested. The whole system could not be included in one simulation due to computational power, so it was divided into two individual parts: AC-DC converter – generator – wind turbine subsystem and DC-DC converter – electrolysis system.

As it was expected, the simulations validated the models made in the previous chapter. The difference in responses between the simulation and controller design is due to the system limitation like maximum currents, voltages or duty-cycles.

The only overshoot that is higher than the desired limit is the speed controller, but that can be reduced if the reference speed is given as a ramp and not a step input. Due to the fact that the overall system has a high time constant this is acceptable.

It can also be observed, introducing more converters in parallel on the DC-DC stage is possible if more power is needed. If they are interleaved, the ripple in the output current is reduced, thus being able to reduce the inductor size of the converters. Also the junction temperature of the switching devices is analyzed, and as it can be seen, it is expected to be 90 °C, with 60 degrees below the maximum admissible temperature (150 °C specified in the device datasheet), resulting in the possibility of overloading the converter.

To validate the converter design method, a small scale prototype was developed in the laboratory and tested. The results will be presented in the following chapter.

CHAPTER 5. EXPERIMENTAL PROTOTYPE

5.1. DESCRIPTION OF EXPERIMENTAL SETUP

As mentioned in the beginning of the thesis the prototype setup is different from the one used in simulations. The difference consists in the fact that the AC-DC converter is connected to the grid, not a wind turbine. A simplified schematic of the prototype is presented in Figure 62. The subsystems of the prototype are tested individually and also the whole system is tested as one. Prior to every stage of testing the used schematic for each case is presented or explained. The tests are divided in AC/DC converter testing, DC/DC converter testing and system experimental results. Also the control strategy and the design of the controllers are presented.

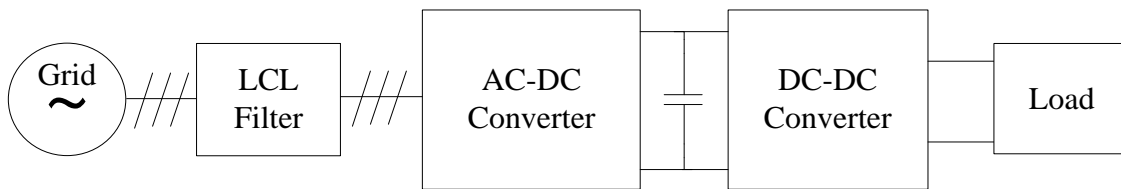


FIGURE 62: SIMPLIFIED SCHEMATIC OF THE PROTOTYPE USED FOR TEST IN THE LABORATORY

5.2. AC/DC CONVERTER TESTING

For the reason that a physical wind turbine it is not available to test the power electronics, as source of the AC voltage, the grid is used. Taking this into consideration instead of the field oriented control for AC-DC converter, a voltage oriented control (VOC) is employed. This is presented in Figure 63 [22]. The proposed control system is composed from a phase locked loop subsystem in order to synchronize with the grid, a reactive power controller to provide the q-component reference current, a DC-link voltage controller to keep the DC-link voltage constant which provides the reference for the current d-axis component, current controller block subsystem and for the modulator a space vector modulation technique was used. A more detailed view on the different controllers is presented in the following subchapters and the control strategy implemented in the DSP is presented in Appendix B.

The testing of the AC-DC converter was divided into three main parts: PLL testing, current controller testing and system test. Each stage is presented in different subchapters along with the design of the controllers used and the presentation of the test setup and control strategy.

All the tests are performed at low power (<10 kW) due to the power limitations in the laboratory.

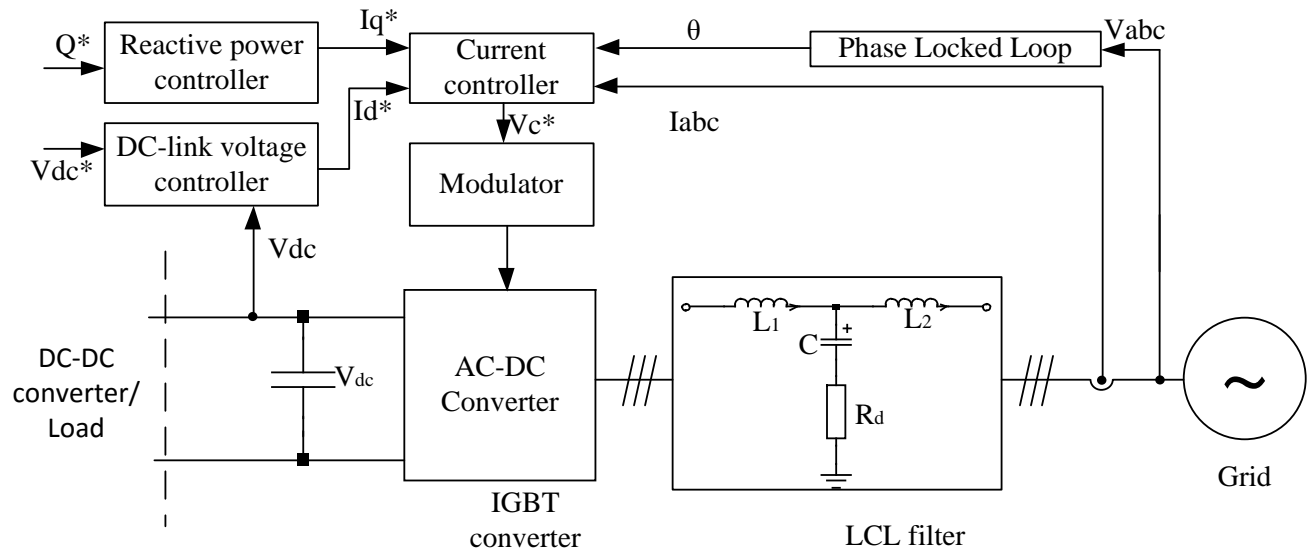


FIGURE 63: VOLTAGE ORIENTED CONTROL BLOCK DIAGRAM FOR THE GRID CONNECTED AC-DC CONVERTER

5.2.1. PLL DESIGN AND TESTING

In order to use the grid as the AC source, the voltage angle must be determined in order to be able to control the power flow. Synchronization is done by a phase locked loop system, as presented in Figure 64. The voltages are transformed from natural abc frame into the alpha-beta frame, after which they are filtered using a Second Order Generalized Integrator (SOGI), as presented in Figure 65. The filtered alpha-beta components of the voltages are transformed into rotational dq reference frame using the estimated angle θ . Using a PI regulator the estimated angle is changed so the q component of the voltage is maintained at zero, thus obtaining the real voltage angle [21].

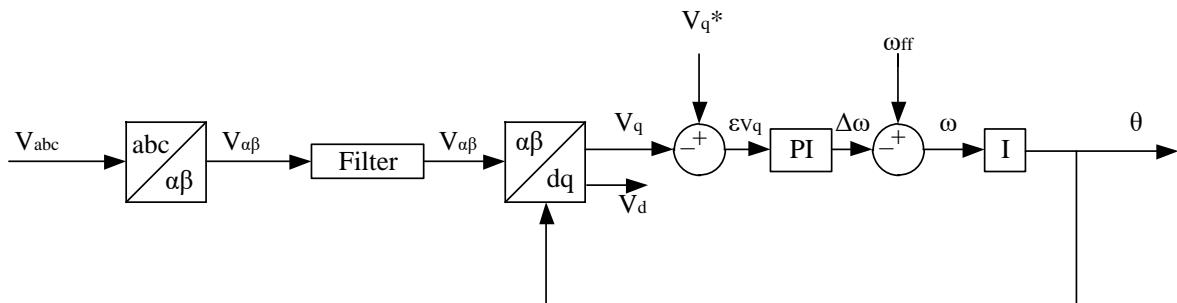


FIGURE 64: THREE-PHASE PHASE LOCKED SYSTEM FOR GRID CONNECTED CONVERTER

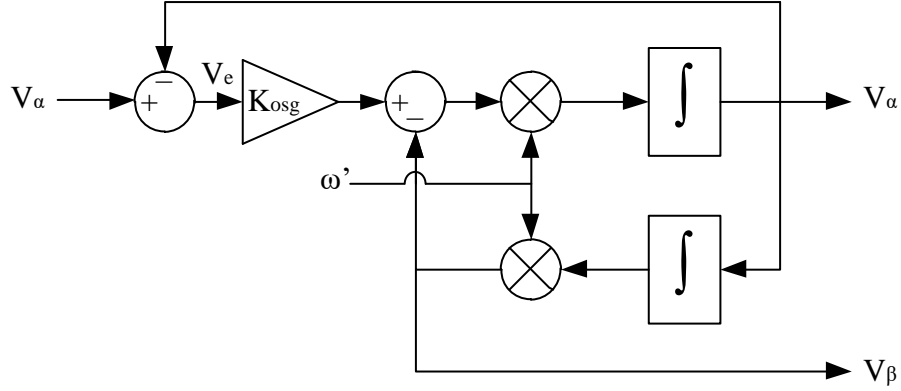


FIGURE 65: SECOND ORDER GENERALIZED INTEGRATOR STRUCTURE USED AS FILTER FOR THE ALPHA-BETA COMPONENTS OF THE GRID VOLTAGE

The implementation of the PLL using SOGI was done using a Texas instruments DSP (F28m36), which required discretization of both schematics and rewriting them as differential equations. From the three different methods that can be used to discretize the system: Backward Euler, Forward Euler or Tustin, the last one was chosen because it provides at the output of the oscillator a perfect 90 degree phase shift between V_α and V_β . After discretizing, the resulting transfer functions for the SOGI in the z-domain becomes (60) [26]:

$$\begin{aligned}
 H_\alpha(z) &= \frac{V_\alpha}{V_i} = \frac{b0d + b2dz^{-2}}{1 + alz^{-1} + a2z^{-2}}; \quad H_\beta(z) = \frac{V_\beta}{V_i} = \frac{b0q + b1qz^{-1} + b2qz^{-2}}{1 + alz^{-1} + a2z^{-2}} \\
 b0d &= \frac{2k\omega T_s}{\omega^2 T_s^2 + 2k\omega T_s + 4}; \quad b2d = -\frac{2k\omega T_s}{\omega^2 T_s^2 + 2k\omega T_s + 4}; \\
 b0q &= \frac{k\omega^2 T_s^2}{\omega^2 T_s^2 + 2k\omega T_s + 4}; \quad b1q = \frac{2k\omega^2 T_s^2}{\omega^2 T_s^2 + 2k\omega T_s + 4}; \\
 b2q &= \frac{k\omega^2 T_s^2}{\omega^2 T_s^2 + 2k\omega T_s + 4}; \\
 a1 &= \frac{2\omega^2 T_s^2 - 8}{\omega^2 T_s^2 + 2k\omega T_s + 4}; \quad a2 = \frac{\omega^2 T_s^2 - 2k\omega T_s + 4}{\omega^2 T_s^2 + 2k\omega T_s + 4};
 \end{aligned} \tag{60}$$

For the alpha-beta to dq transformations trigonometric functions have been used so no discretization was needed for the rest of the PLL except the integrator part and the PI controller.

The simplest way to implement the PI controller is to discretize using the Backward Euler (BE) method the s-domain PI transfer function (61). BE can be used because the digital implementation is not sensitive to the digitization method. In this way, the z-domain transfer function becomes (62) [26].

$$H_{PI}(s) = K_p \left(1 + \frac{K_i}{s}\right) \quad (61)$$

$$H_{PI}(z) = \frac{K_p + T_s \cdot K_i - K_p z^{-1}}{1 - z^{-1}} \quad (62)$$

The controller parameters can be tuned if the PLL loop from Figure 64 is linearized as in [22]. The damping factor of the second order system is set to 0.707 in order to obtain an overshoot below 5% and a fast response time. The time constant of the system should be at least 4.6 times slower than the settling time. In this way the gains of the PI can be calculated as [26]:

$$K_p = \frac{9.2}{T_{set}} \quad (63)$$

$$K_i = \left(\frac{4.6}{0.707 \cdot T_{set}}\right)^2 \quad (64)$$

Selecting a settling time of 60 ms yields a value of 153.33 for K_p and 11759.1 for K_i which after discretization will give the transfer function presented in (65).

$$H_{PI}(z) = \frac{155.25 - 153.33 z^{-1}}{1 - z^{-1}} \quad (65)$$

A good way to verify if the PLL manages to sync with the grid voltage, it is to monitor the q axis component of the voltage, which in a perfectly three phase balanced synchronized system would be zero. The result can be seen in Figure 67. Both the d- and q-axis voltages can be observed to verify also the magnitude of the voltage vector, which is represented by the d-axis component, measurement which is made with the setup shown in Figure 63.

In order to avoid aliasing and undesired noise which appears due to the long cable between the voltage measurement board and the DSP adapter board, a filter is designed and placed on the latter close to the ADC pins of the DSP. The topology chosen for the filter is Bessel at a cutoff frequency of 12 kHz. It is composed from 2 cascaded Sallen key filters, design presented in Figure 66 (schematic taken from the TI webench filter designer [27]). According to the frequency response of the filter, it can be observed that at 50 Hz it introduces a delay of 0.4 degrees which can be neglected and it has zero dB attenuation so the input signal's amplitude is not affected.

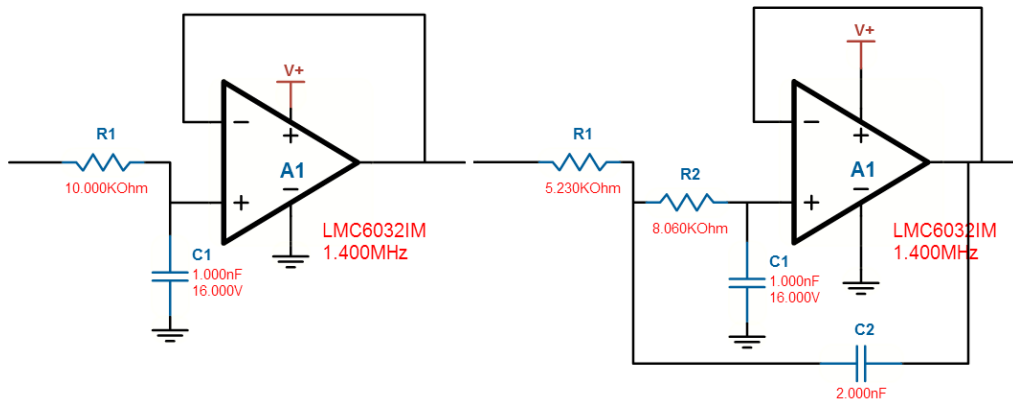


FIGURE 66: FILTER DESIGN USED FOR GRID VOLTAGE MEASUREMENT [27]

As it can be observed, the d component fluctuates around the peak value of the grid voltage and the q component around zero. Due to the fact that the grid in the laboratory is a weak grid, a higher disturbance can be seen at the start, when the converter is connected and power is absorbed or fed into the grid. After the initial disturbance there is also an oscillation present at a frequency of 50 Hz. This is due to the fact that the grid voltages are not perfectly sinusoidal and equal in amplitude. The grid voltages can be seen in Figure 68. Although the oscillation exists, in steady state the amplitude of it is maximum 8 volts, which accounts for an error of 2.4% out of the 340 which is the amplitude of the voltage vector.

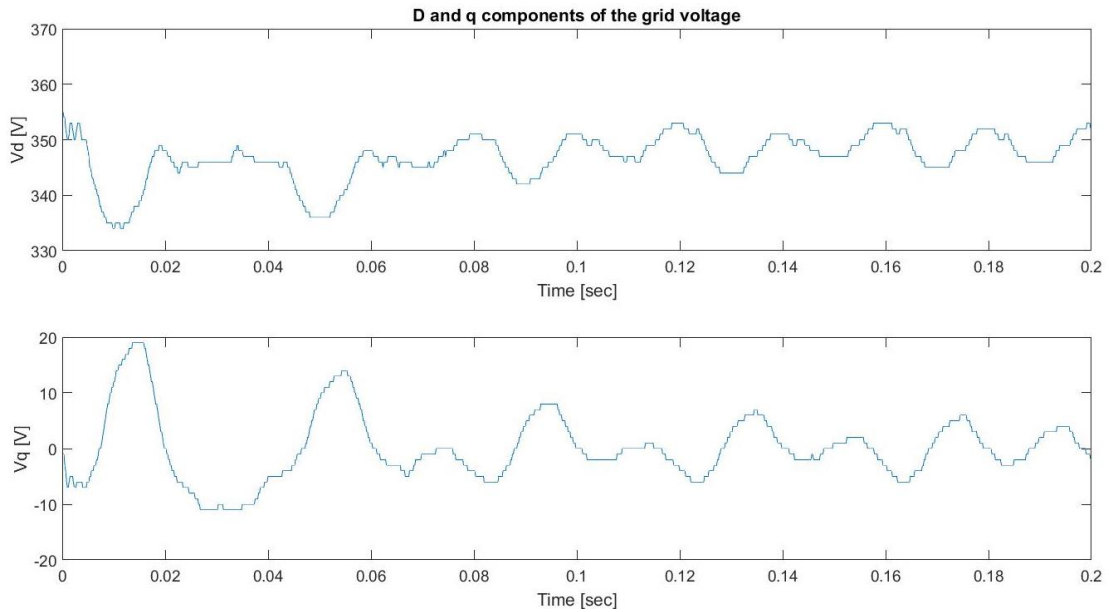


FIGURE 67: D (TOP) AND Q (BOTTOM) COMPONENTS OF THE GRID VOLTAGE PRESENTED IN FIGURE 68

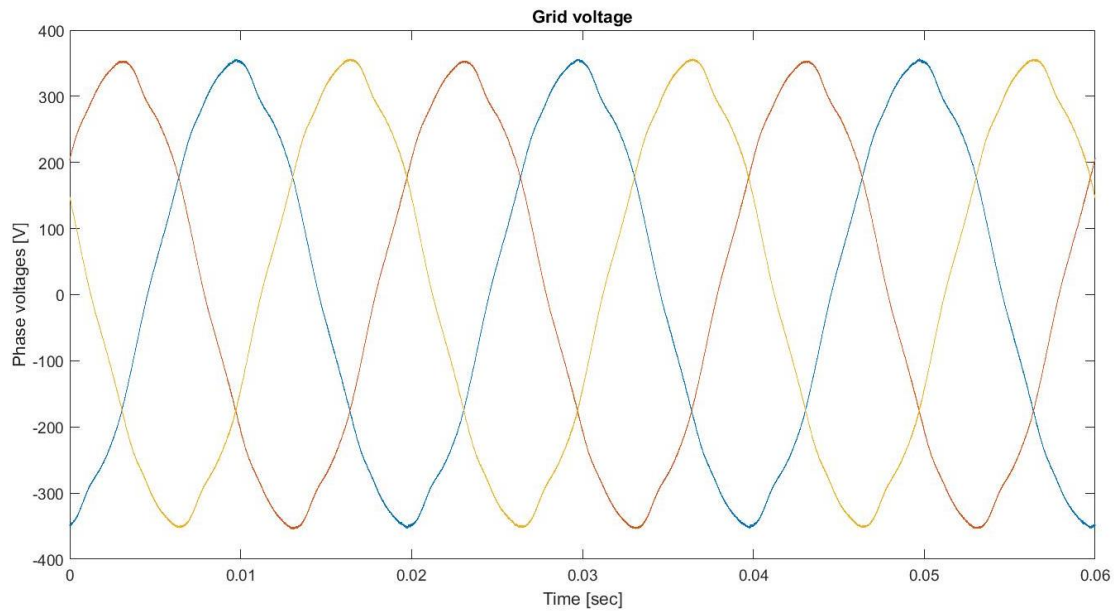


FIGURE 68: MEASURED GRID VOLTAGES V_{ABC} WITH THE GRID SIDE CONVERTER DISCONNECTED

5.2.2. CURRENT CONTROL OF THE GRID CONNECTED CONVERTER

The current controller strategy is very similar with the one presented for the FOC of the generator, the differences between them are the decoupling terms and feed forward terms. These do not affect the steady state values of the system, but influence on the dynamics of the system. A block diagram of the current control can be seen in Figure 69 [21].

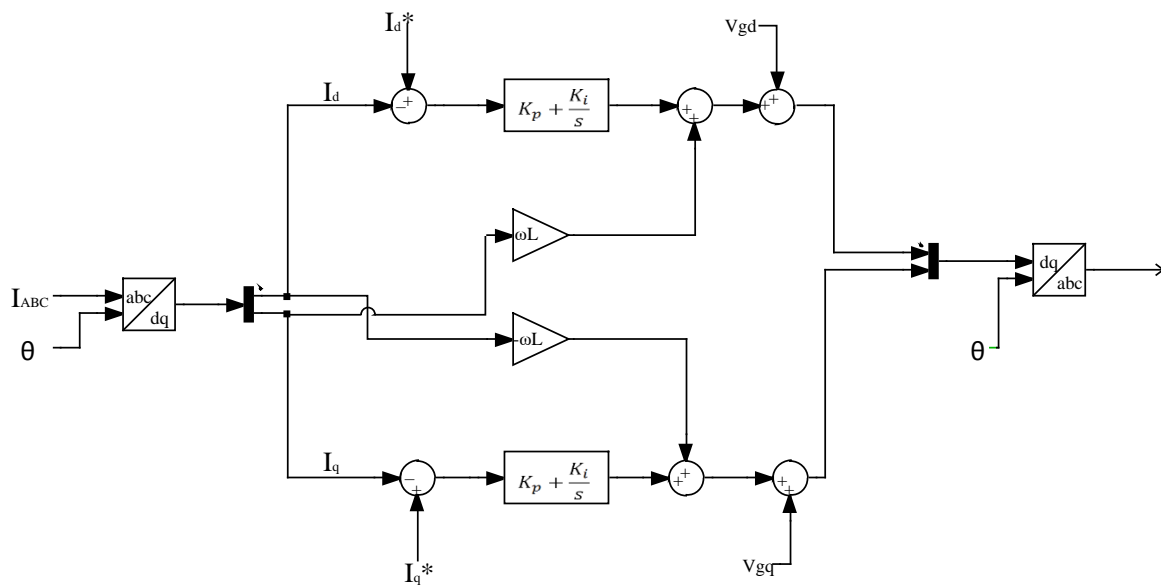


FIGURE 69: CURRENT CONTROL BLOCK DIAGRAM FOR GRID SIDE CONVERTER [21]

The decoupling terms include the total inductance seen by the converter, including filter and grid inductance. As the latter one is difficult to measure, it is not considered in the initial calculation of the decoupling terms.

With the two current axes decoupled, they can be seen as individual current controllers where the plant is the LCL filter, which has a transfer function presented in equation (66), where L_1 is the converter side inductor, L_2 is the grid side inductor, C_F is the filter capacitor and R_D is the damping resistor [28]. The values for the filter are presented in Table 22.

$$H(s) = \frac{I_I(s)}{V_I(s)} = \frac{L_1 C_F s^2 + R_D C_F s + 1}{L_1 L_2 C_F s^3 + (R_D L_1 C_F + R_D L_2 C_F) s^2 + (L_1 + L_2) s} \quad (66)$$

TABLE 22: LCL FILTER VALUES FOR THE GRID SIDE CONVERTER

L_1	2.8 [mH]
L_2	1.8 [mH]
C_F	50 [μF]
R_D	1 [Ω]

In the interest of designing the current controllers PI parameters for the discrete system to be able to implement them in a microcontroller, the transfer function is discretized using Tustin method and it will generate equation (67). For the controller a Forward Euler method is used for discretization having a sample time of 167 μs .

$$H(z) = \frac{0.05606z^2 - 0.09067z + 0.05095}{z^3 - 2.408z^2 + 2.267z - 0.8589} \quad (67)$$

The whole control loop can thereby be redrawn as shown in Figure 70. The root locus method can be used to determine the parameters of the controller. A T_i value of 5 ms was chosen for a fast response of the system. Based on the root locus, K_p was chosen to 3.66 and a step response of the system can be seen in Figure 71.

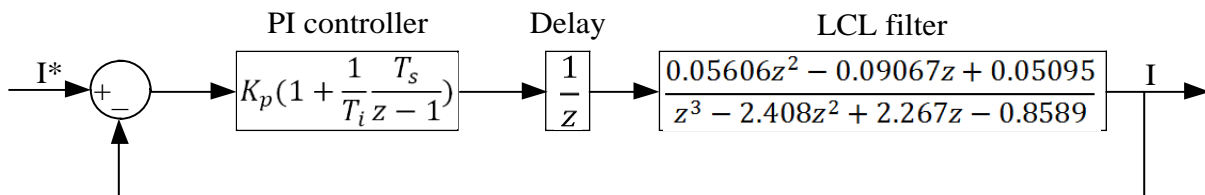


FIGURE 70: SIMPLIFIED CURRENT CONTROL LOOP IN A DIGITAL CONTROL SYSTEM

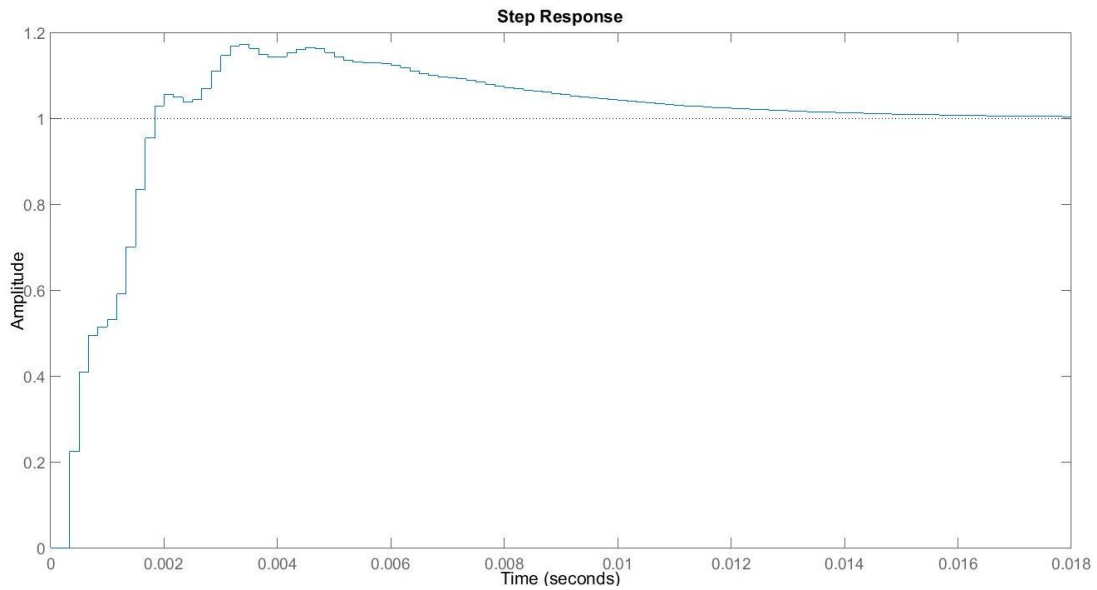


FIGURE 71: STEP RESPONSE FOR CURRENT CONTROL LOOP OF THE GRID CONNECTED CONVERTER

In order to be able to verify the current controller's response, the system presented in Figure 72 has been set up in the laboratory. A DC voltage source is used instead of a load in order to maintain the DC link voltage constant while both d- and q-components of the current are varied. A limitation of this setup is that active power can only be fed into the grid, not absorbed, due to the lack of loads on the DC side. However this is not so important because the controllers behave the same if active power is introduced or absorbed from the grid. The only difference between the two is the sign of the d-component of the current.

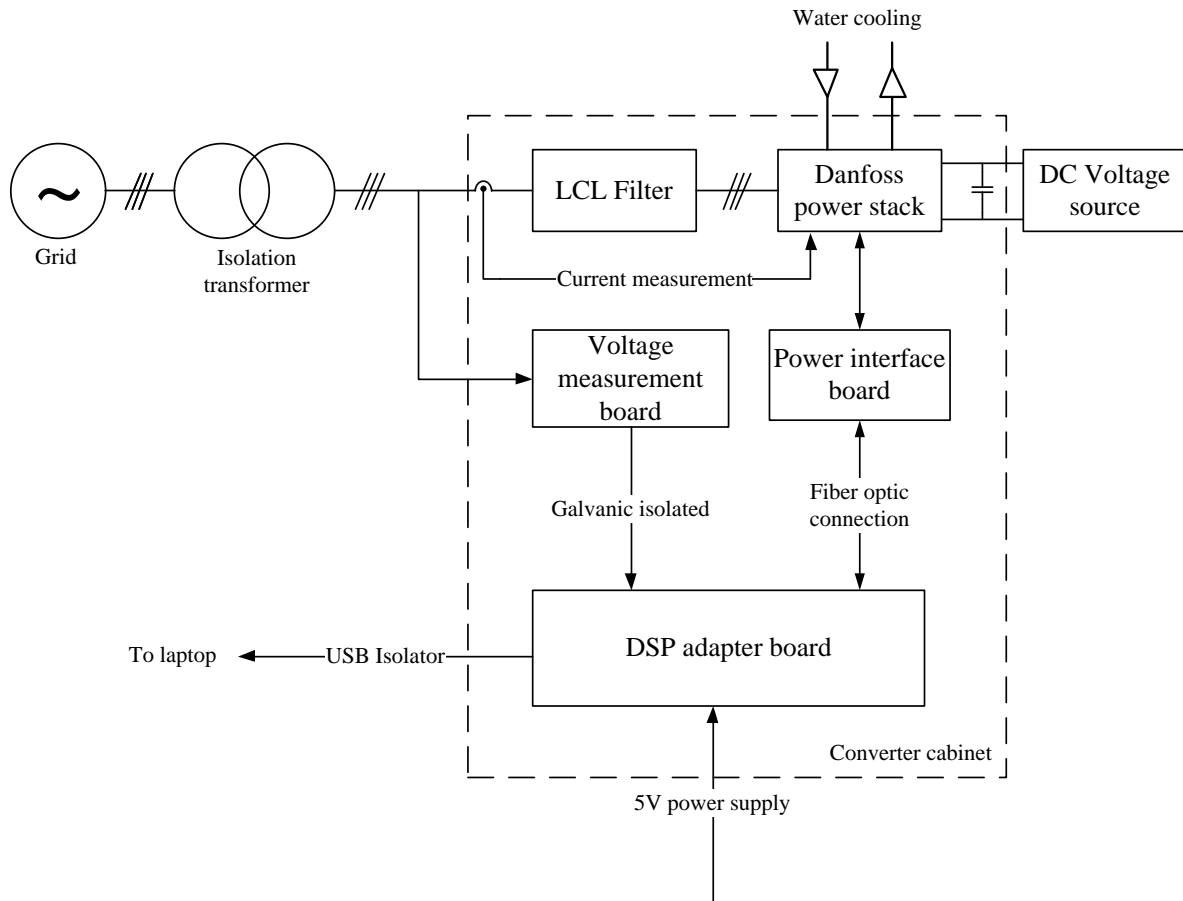


FIGURE 72: EXPERIMENTAL SETUP FOR TESTING THE CURRENT CONTROLLERS IN A 250KW GRID CONNECTED CONVERTER

There is a power limitation imposed in the laboratory by the circuit breakers at 16 amps, thus making the measuring of the currents with high accuracy not possible due to the fact that the current sensors are rated for ± 1400 amps with a tolerance of 1%. For increasing the accuracy the cable was wound 8 times through the current sensor, and thereby reducing the measuring range to ± 175 amps ($1400/8$) and thus reducing the tolerance to 1.75 amps.

For verifying the controller's behavior and the influence of one on the other, positive and negative steps in both components were performed. The results can be seen in Figure 73 to Figure 76 where in the top is the d component of the grid current and bottom is the q component.

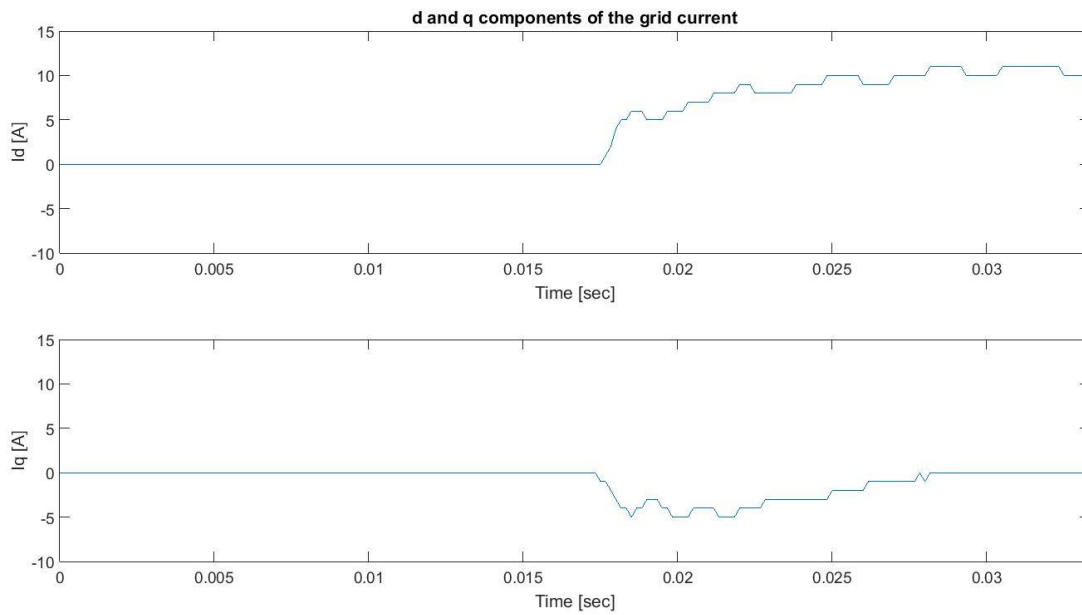


FIGURE 73: 10 AMP STEP IN I_D FOR CURRENT CONTROLLER TEST OF GRID CONNECTED CONVERTER

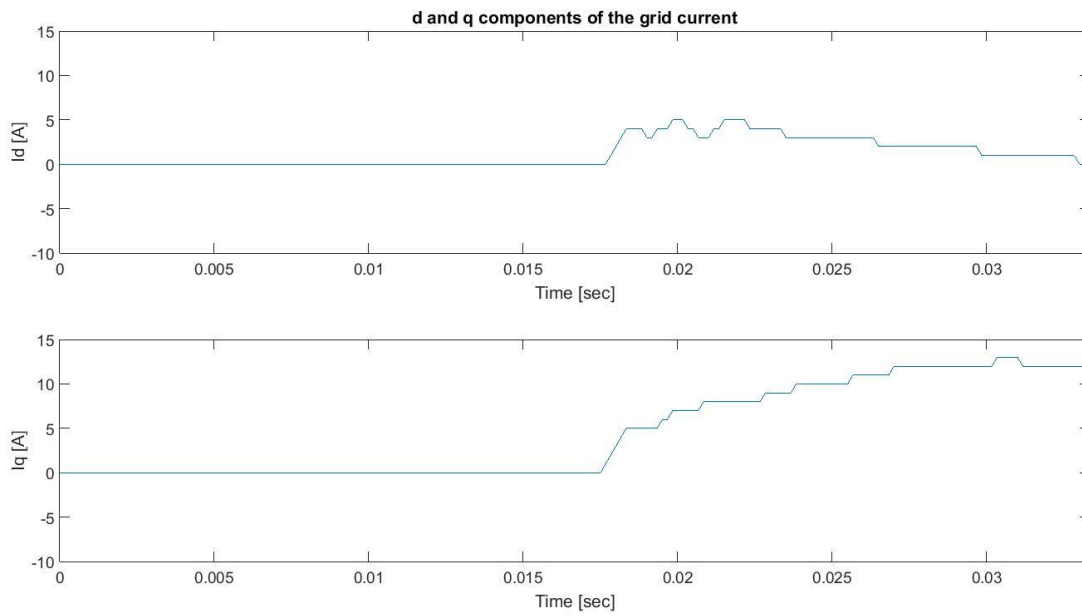


FIGURE 74: 10 AMP STEP IN I_Q FOR CURRENT CONTROLLER TEST OF GRID CONNECTED CONVERTER

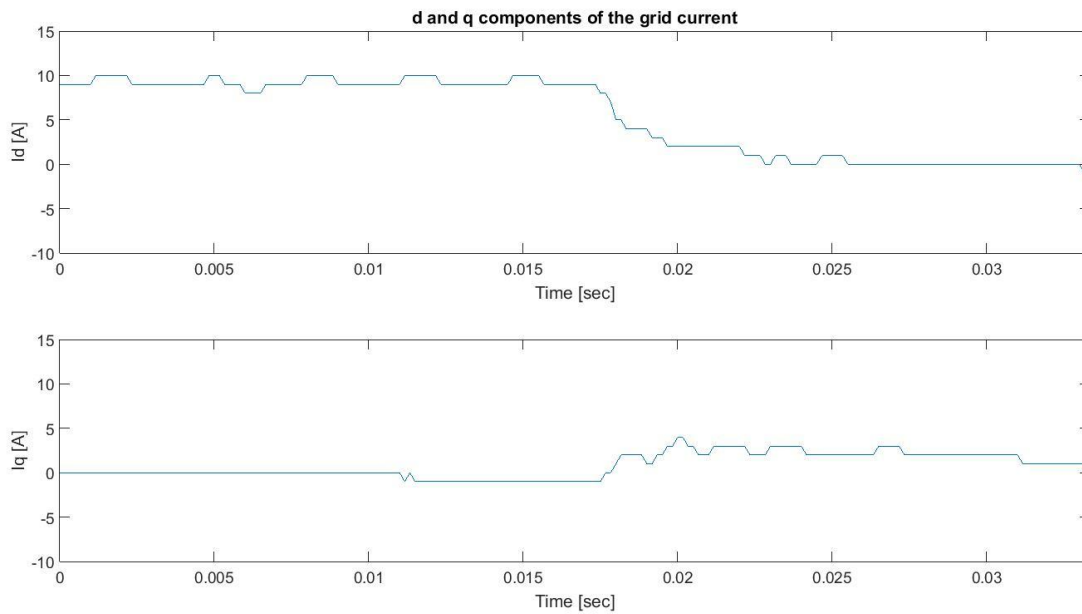


FIGURE 75: NEGATIVE 10 AMP STEP IN I_D FOR CURRENT CONTROLLER TEST OF GRID CONNECTED CONVERTER

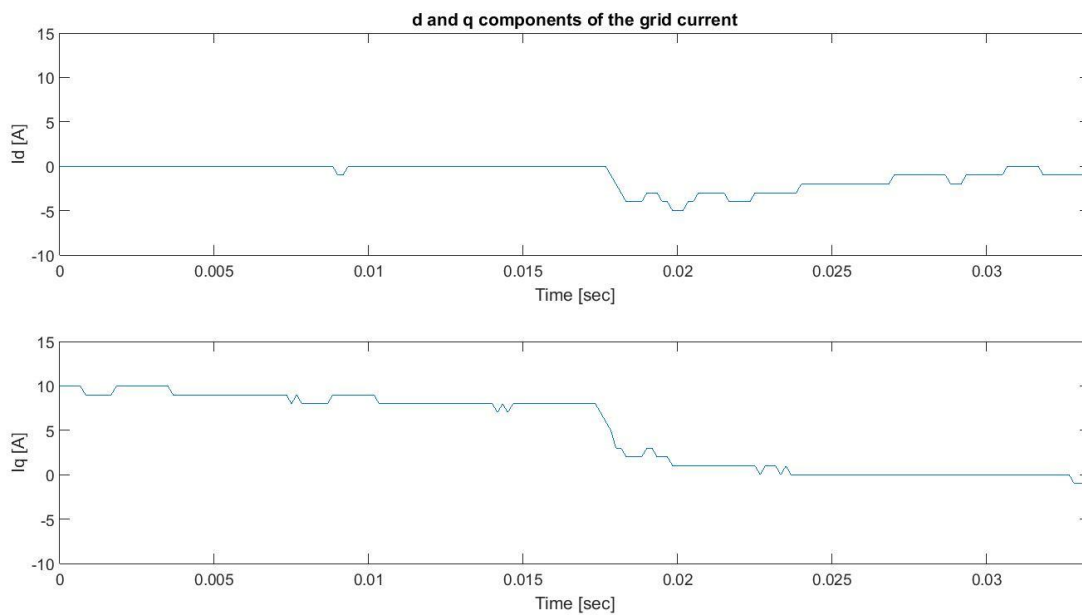


FIGURE 76: NEGATIVE 10 AMP STEP IN I_Q FOR CURRENT CONTROLLER TEST OF GRID CONNECTED CONVERTER

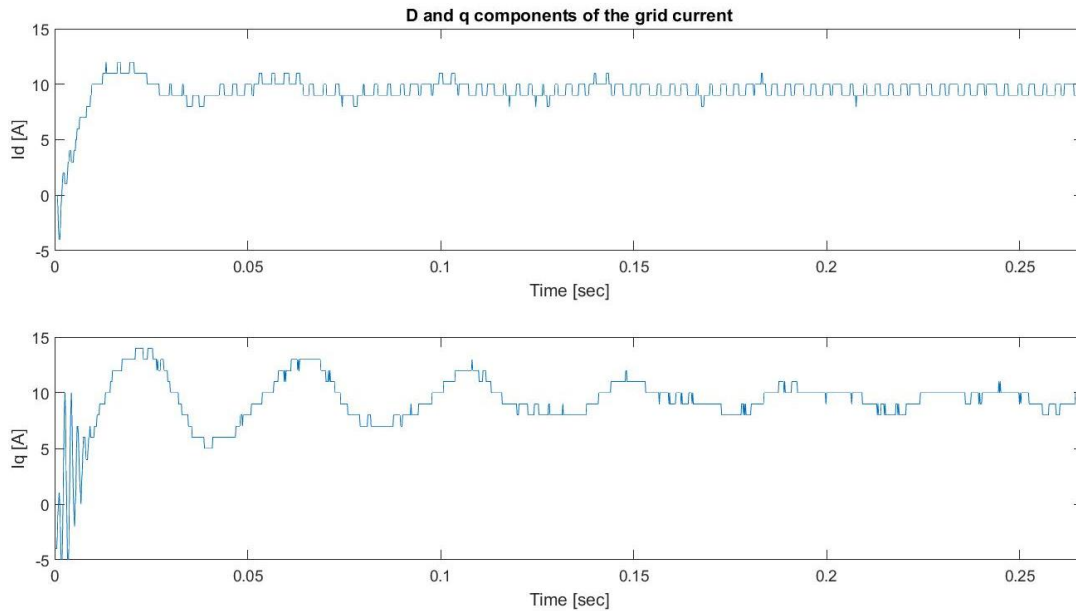


FIGURE 77: INITIAL 10 AMP STEP IN BOTH I_D AND I_Q FOR CURRENT CONTROLLER TEST OF GRID CONNECTED CONVERTER

Based on the measurements, it can be concluded that the step response is about 20 samples (3.3 ms) and the overshoot is around 10%. These results are obtained after the parameters of the PI controllers were slightly modified under observations of the system performance. The controller parameters were varied around the designed values and the values which gave the best results were chosen.

As it can be observed there is a small ripple (approximately 1 amp) in both components of the grid current. This is due to noise picked up by the cable between the stack and power interface board which will be reduced to minimum needed in the final version of the converter, thus minimizing the noise interference. Due to this noise, the resolution of measurements was maintained at 1 A because any value smaller would be unreliable. It can also be observed that the amplitude of the ripple does not change with the value of I_d or I_q which means at higher currents, this ripple will be negligible, being smaller than the sensor tolerance. There is also smaller frequency ripple present in the q component (as it can be seen in Figure 77) which is caused by the harmonic components of the filter absorbed current. A more precise measurement can be performed when tests at higher power will be realized since the noise to signal ratio will be reduced in such a case.

There is interference between the two components currents, and it is due the fact that the grid impedance was not taken into account when designing the decoupling terms. In this design only the filter inductance has been considered because the grid inductance is not known, but it can be estimated based on more measurements.

As for the grid currents in relation to the grid voltages, this one can be seen in Figure 78 to Figure 83. These measurements were made as if the converter would have been the load, positive voltage and current symbolizing the converter is absorbing power.

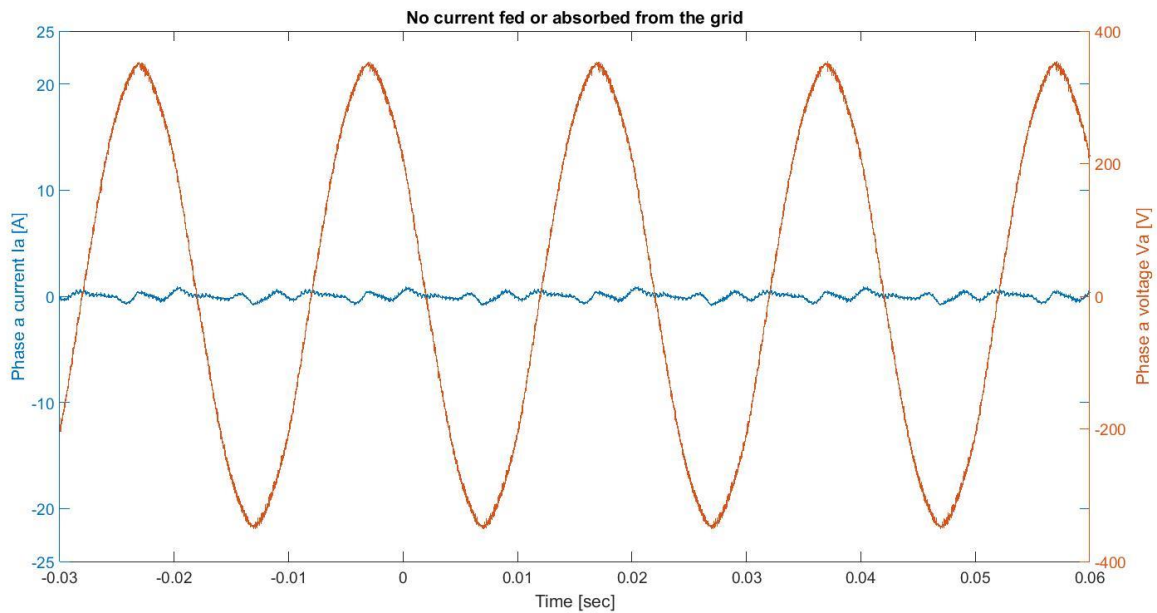


FIGURE 78: CURRENT CONTROLLER TEST OF THE GRID SIDE CONVERTER, PHASE A CURRENT (BLUE) AND VOLTAGE (RED) WHEN $I_d=I_q=0$ A

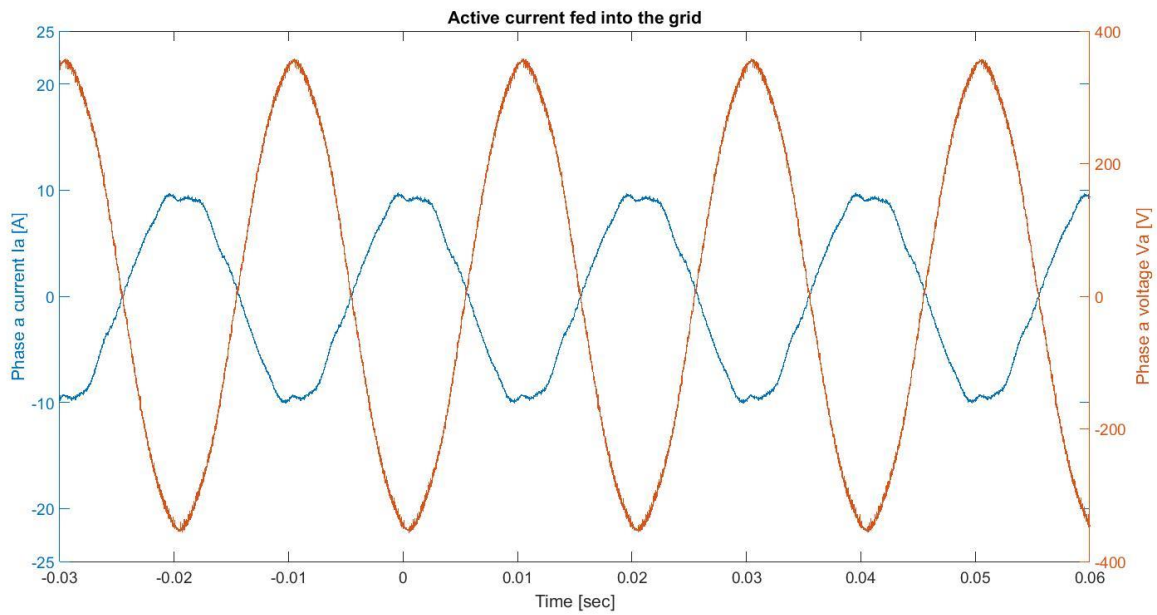


FIGURE 79: CURRENT CONTROLLER TEST OF THE GRID SIDE CONVERTER, PHASE A CURRENT (BLUE) AND VOLTAGE (RED) WHEN $I_d=10$ A AND $I_q=0$ A

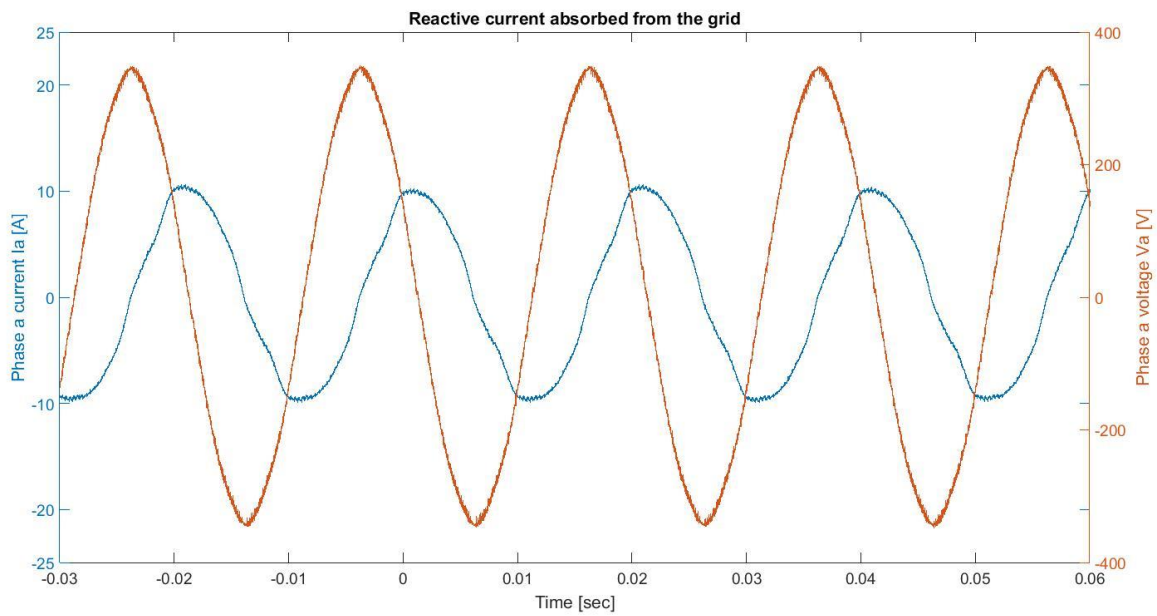


FIGURE 80: CURRENT CONTROLLER TEST OF THE GRID SIDE CONVERTER, PHASE A CURRENT (BLUE) AND VOLTAGE (RED) WHEN $I_d=0$ A AND $I_q=10$ A

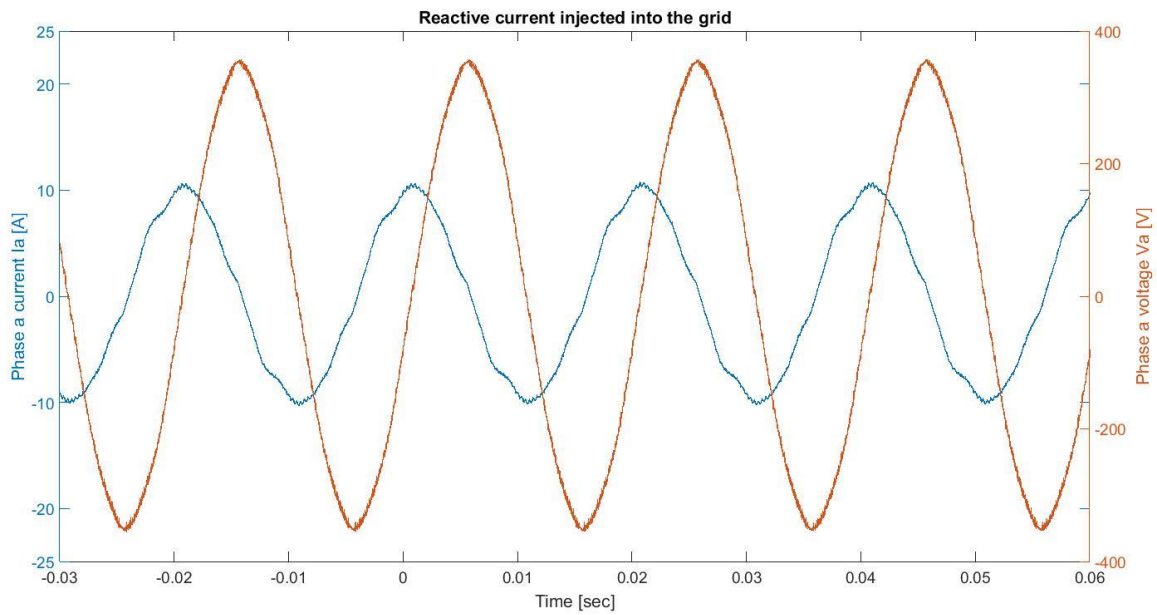


FIGURE 81: CURRENT CONTROLLER TEST OF THE GRID SIDE CONVERTER, PHASE A CURRENT (BLUE) AND VOLTAGE (RED) WHEN $I_d=0$ A AND $I_q=-10$ A

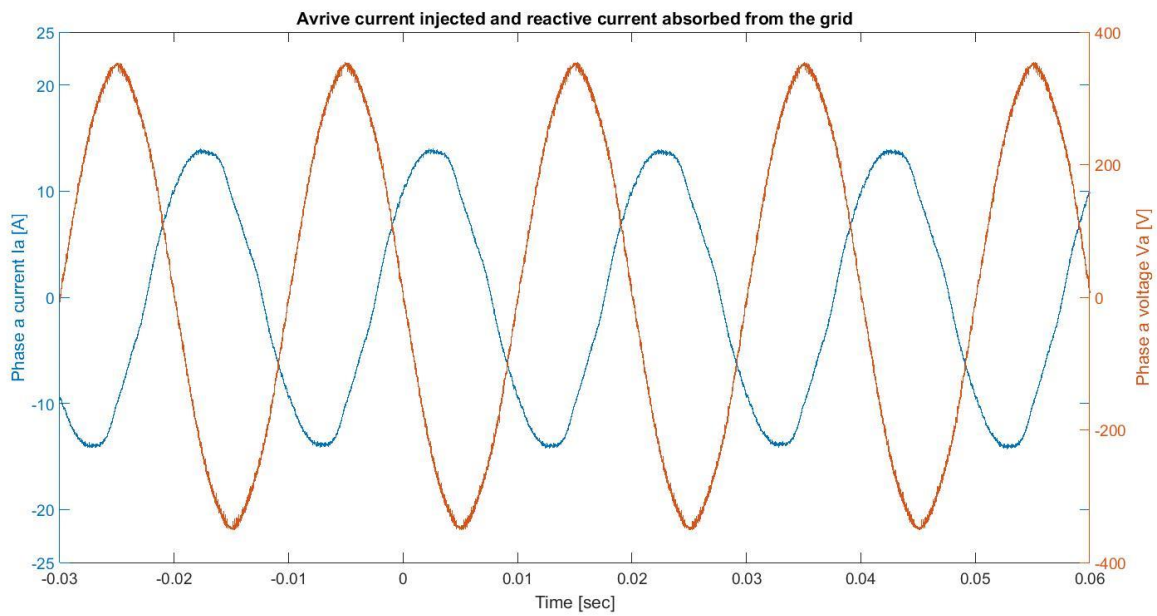


FIGURE 82: CURRENT CONTROLLER TEST OF THE GRID SIDE CONVERTER, PHASE A CURRENT (BLUE) AND VOLTAGE (RED) WHEN $I_d=10$ A AND $I_q=10$ A

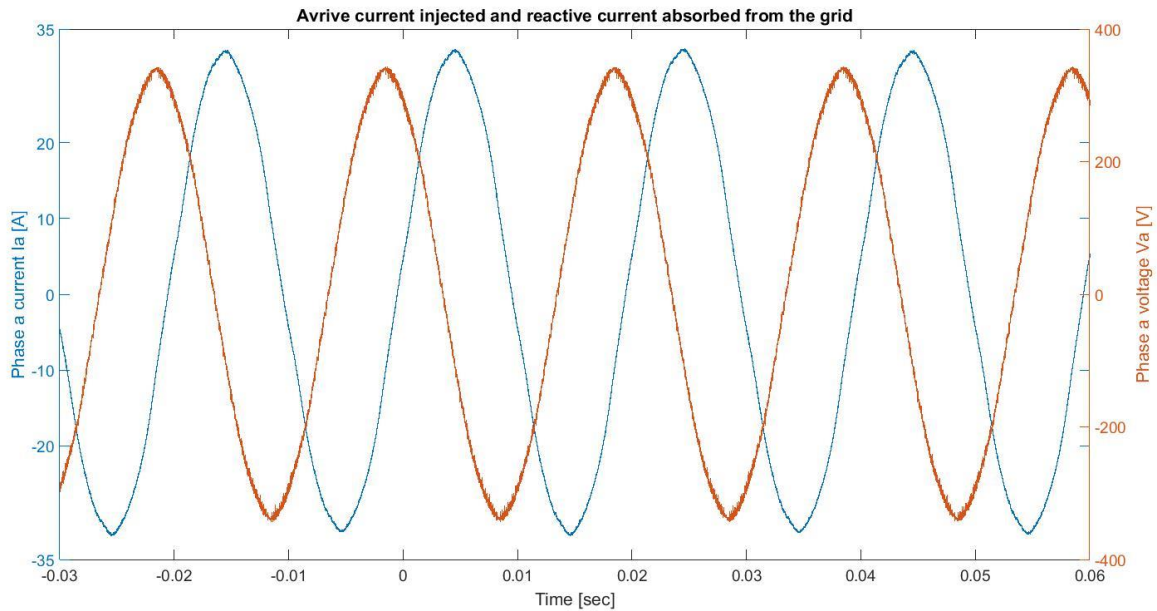


FIGURE 83: CURRENT CONTROLLER TEST OF THE GRID SIDE CONVERTER, PHASE A CURRENT (BLUE) AND VOLTAGE (RED) WHEN $I_d=10$ A AND $I_q=30$ A

Although more tests were done, only 6 cases are presented: when the reference for both currents are zero, when the active current is injected into the grid, when the reactive current is fed into the grid, when reactive current is absorbed from the grid and when both components of the current are non-zero. As previously mentioned, at higher power the influence of this current will decrease and the quality of the current will improve significantly. This can be seen in Figure 83, where the waveform of the current is better compared to the smaller currents results.

A step response of the current can be observed in Figure 84, where it can be seen that just a small overshoot is present, but the settling time is less than one period.

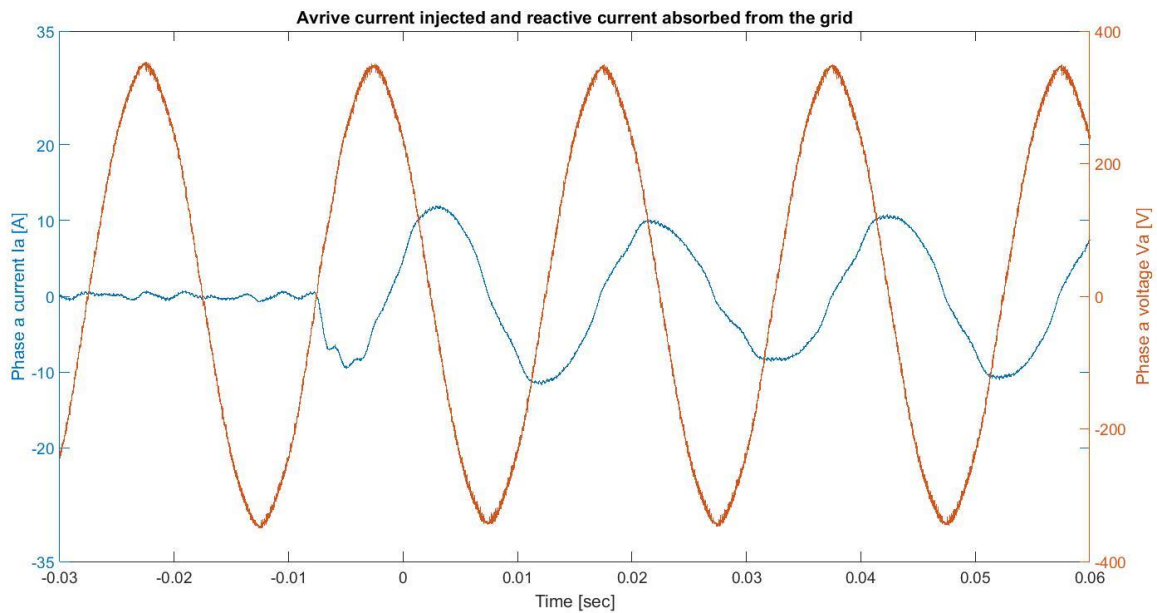


FIGURE 84: CURRENT CONTROLLER TEST OF THE GRID SIDE CONVERTER, 10 A STEP RESPONSE IN THE q -COMPONENT OF THE CURRENT

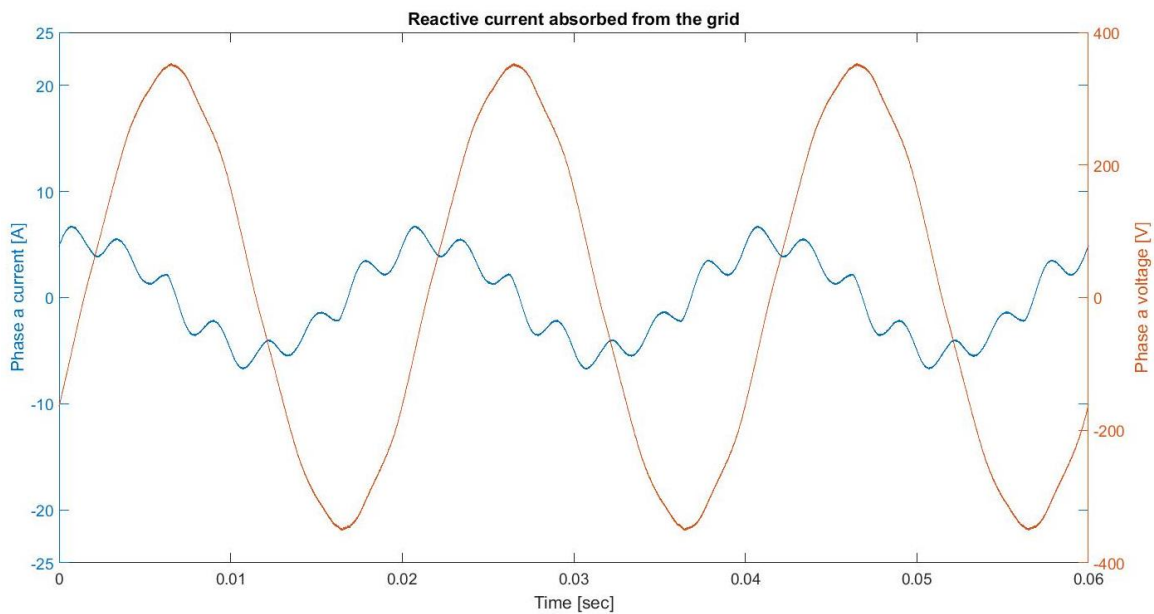


FIGURE 85: MEASUREMENT OF THE FILTER CURRENT AND GRID VOLTAGE ON PHASE A WHEN THE CONVERTER IS DISCONNECTED

The grid current is not perfectly sinusoidal due to the fact that it needs to compensate also the filter absorbed current, which is rich in harmonics and this can be observed in Figure 85. This is due to the poor quality of the grid voltages, which was presented in the previous subchapter.

5.2.3. DC VOLTAGE AND REACTIVE POWER CONTROL

The reactive power and DC-link voltage control loop it is an outer loop (see Figure 63) which provides the references for the two axis currents in order to obtain necessary values and it is presented in Figure 86.

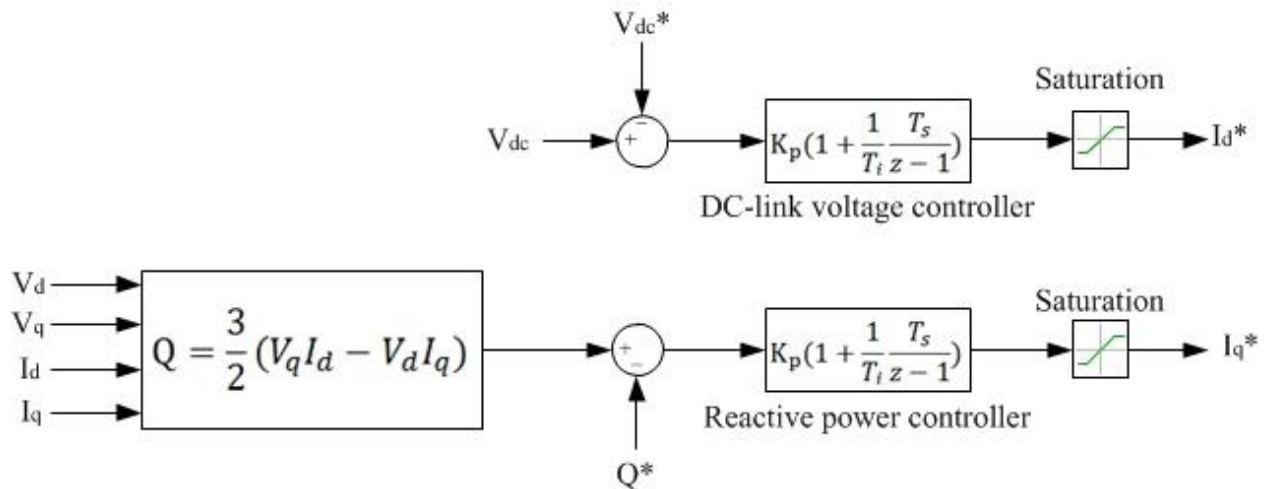


FIGURE 86: REACTIVE POWER AND DC-LINK VOLTAGE CONTROL STRATEGY FOT THE AC-DC CONVERTER

The DC link voltage gives the reference for I_d and the reactive power controller gives the reference for I_q . The saturation blocks are used in order to limit the values for the current references so that they do not exceed the rated values for the converter.

The controller design for the two outer loops is done assuming perfect synchronization with the grid voltage, resulting in (68) and (69). In this way the active power becomes proportional with I_d and the reactive power proportional with I_q . Due to the fact that the DC link voltage is a function of the active power, it results that the DC-link voltage is a function of d axis current, like presented in Figure 87.

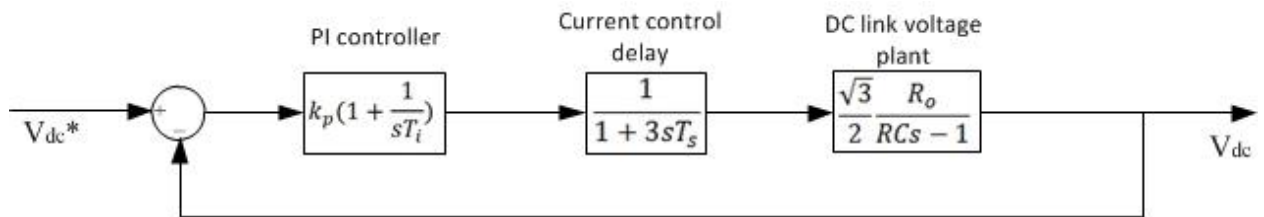


FIGURE 87: DC-LINK VOLTAGE CONTROL BLOCK DIAGRAMFOR THE AC-DC CONVERTER [22]

$$P = \frac{3}{2} V_d I_d = \frac{3}{2} \cdot \sqrt{2} \cdot 230 \cdot I_d = 486 \cdot I_d \quad (68)$$

$$Q = -\frac{3}{2}V_d I_q = -486 \cdot I_q \quad (69)$$

According to [22], the Dc-link voltage to I_d transfer function can be expressed as (70), where R_o represents the equivalent resistance of the converter ($\frac{V_{dc}}{I_{dc}}$) and C is the dc-link capacitor value.

$$\frac{v_{dc}(s)}{i_d(s)} = \frac{\sqrt{3}}{2} \frac{R_o}{1 - R_o C s} \quad (70)$$

By considering $R_o C$ much larger than $3T_s$ and multiplying (70) with the transfer function of a PI controller and a delay corresponding to the current control loop, the open loop transfer function can be described as (71) and the controller parameters can be found using the symmetrical optimum method because there is a double integration in the control system [22].

$$\frac{v_{dc}(s)}{i_d(s)} = \frac{\sqrt{3}}{2} \frac{k_p(1 + T_I s)}{T_I s(1 + 3T_s s) C s} \quad (71)$$

In order to obtain a maximum phase margin, the crossover frequency (ω_c) has to be chosen at the geometric mean of the two corner frequencies. In this way the Bode diagram will show symmetry with respect to the crossover frequency. The relationship between the crossover frequency, phase margin (ψ), sample time (T_s) and integrator time (T_I) is presented in (72) [22].

$$\begin{aligned} \omega_c &= \frac{1}{3aT_s} \\ a &= \frac{1 + \cos\Psi}{\sin\Psi} \\ a &= \sqrt{\frac{T_I}{3T_s}} \end{aligned} \quad (72)$$

At the crossover frequency, the gain of the PI can be expressed as (73) [22]:

$$k_p = \frac{C}{2\sqrt{3}aT_s} \quad (73)$$

Given the phase margin or the constant factor a , the transfer function for the closed loop system becomes (74):

(74)

$$H(s) = \frac{1 + T_I s}{12T_I T_S^2 a s^3 + 4T_I T_S a s^2 + T_I s + 1}$$

At a value of $a=2.4$ a phase margin of 45° is obtained and a damping factor of 0.707 due to the pair of complex poles in the closed loop transfer function. From this the PI parameters of the reactive power controller can be derived as [22]:

$$k_p = 0.12 \cdot \frac{C}{T_S} = 0.12 \cdot \frac{4e^{-3}}{1.66e^{-4}} \quad (75)$$

$$k_I = 17 \cdot T_S = \frac{17}{1.66e^{-4}}$$

As for the reactive power controller, a more simple approach can be used due to the simple proportionality between the reactive power and current. In this way the plant can be assumed to be a simple proportional gain. In order avoid oscillations caused by ripple in the current (which may be due to noise) a digital filter is used in the feedback loop. Taking also into consideration the current control closed loop the system becomes as presented in Figure 88. In this case by using the root locus it is possible to determine the parameters of the PI controller.

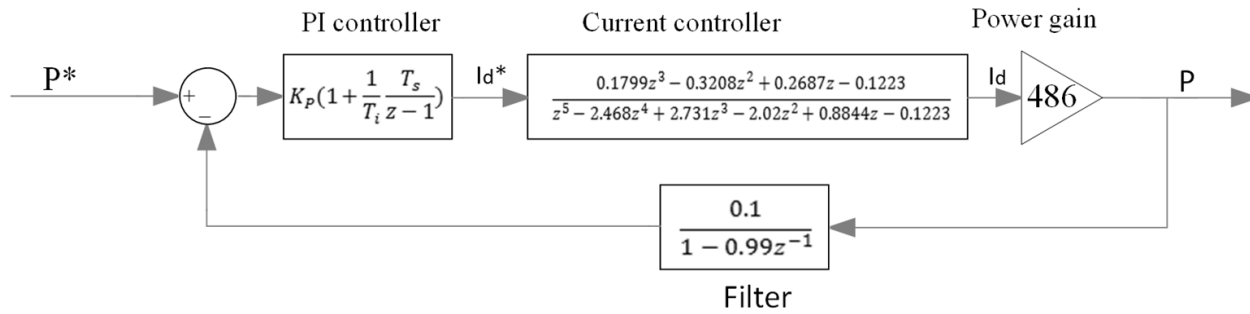


FIGURE 88: REACTIVE POWER CONTROL LOOP FOR THE GRID SIDE CONVERTER

In order to obtain a fast response and also have a time constant slow enough to have the outer loop decoupled from the inner loop an integral constant $T_I = 20$ ms was chosen. Based on the root locus, $K_p = 0.0082$ was chosen, resulting in the final form of the controller (76) which gives the step response presented in Figure 89.

$$G_{\text{controller}} = \frac{0.00818 \cdot z - 0.008112}{z - 1} \quad (76)$$

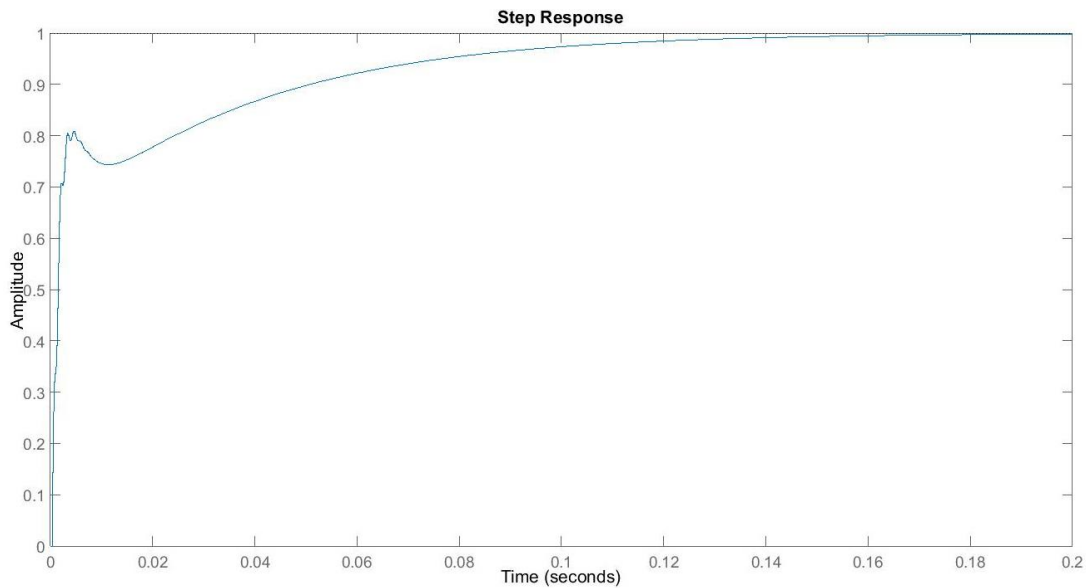


FIGURE 89: STEP RESPONSE FOR REACTIVE POWER CONTROLLER FOR THE AC-DC CONVERTER

To verify the design of the controllers, the test setup was modified from the previous tests it is similar with the one presented in Figure 72. The difference between this one and the one used for testing the current controllers is that the voltage source is replaced with a resistive load in order to observe the converter capability of maintaining the DC voltage at a reference value. The main drawback is that due to security reasons the value of the load cannot be changed, thus the only way to change the amount of active power absorbed from the grid is by changing the DC-link voltage. To validate the controller design multiple test cases are performed: 9000 VAr positive and negative step in reactive power and also 50 V step in the DC-link voltage. The results are shown in Figure 90 to Figure 93.

Although theoretically the reactive power step response should have no ripple, due to disturbances mainly caused by the q component of the grid voltage which is not zero, an oscillation is present with a significant value (1 kVAr). In Figure 91, it can be seen the reactive power alongside the filtered value which, as it can be observed is constant maintained constant by the controllers.

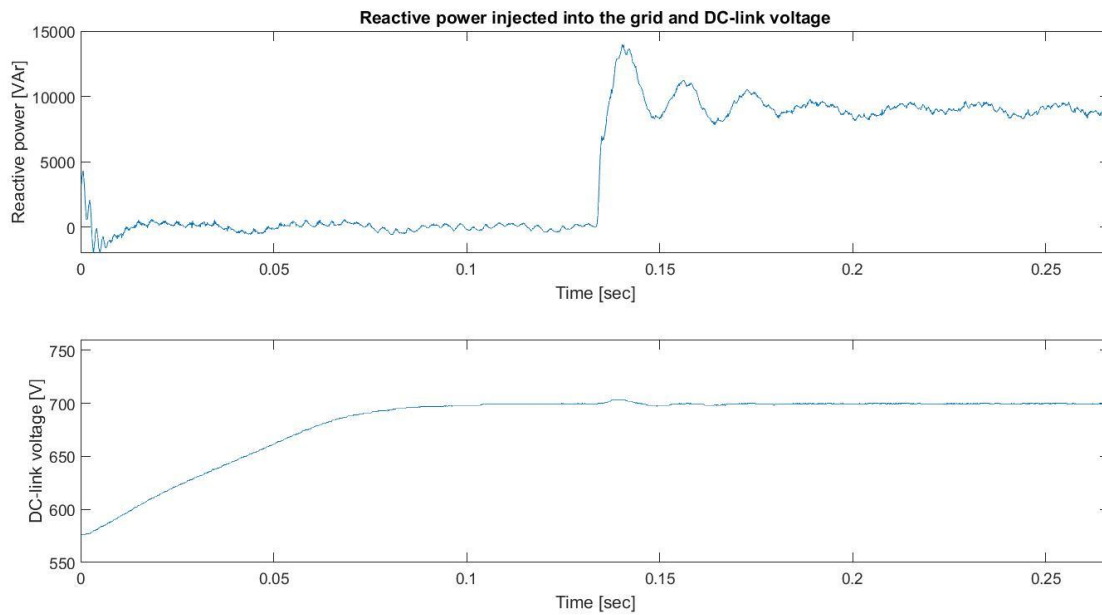


FIGURE 90: TEST OF REACTIVE POWER CONTROLLER FOR THE GRID CONNECTED CONVERTER: REACTIVE POWER (TOP) 9 KVAR STEP AND DC-LINK VOLTAGE (BOTTOM)

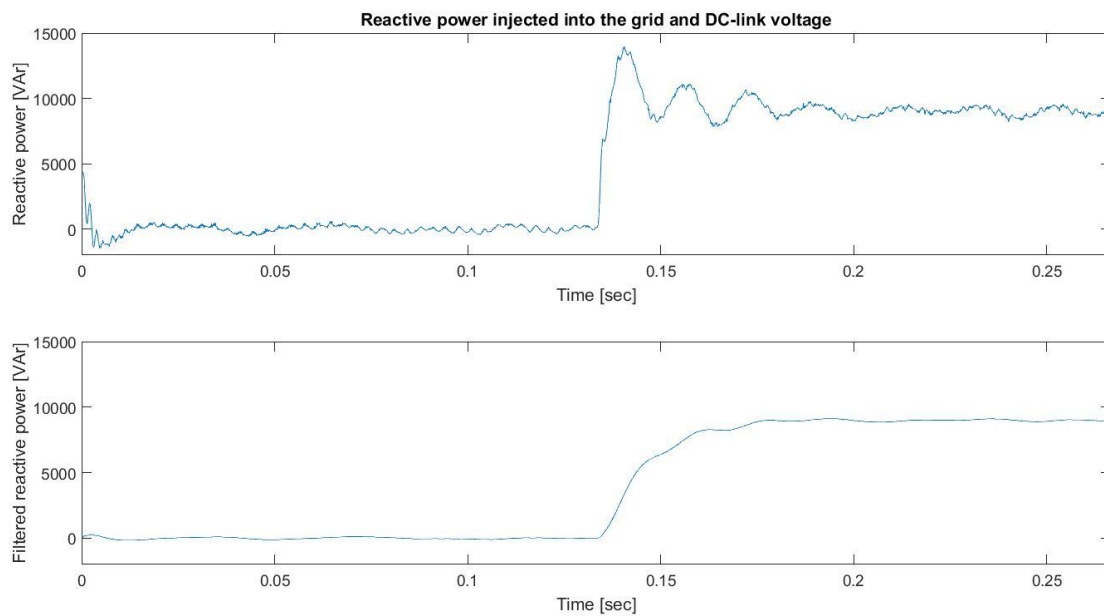


FIGURE 91: TEST OF REACTIVE POWER CONTROLLER FOR THE GRID CONNECTED REACTIVE POWER (TOP) 9 KVAR STEP AND FILTERED REACTIVE POWER (BOTTOM)

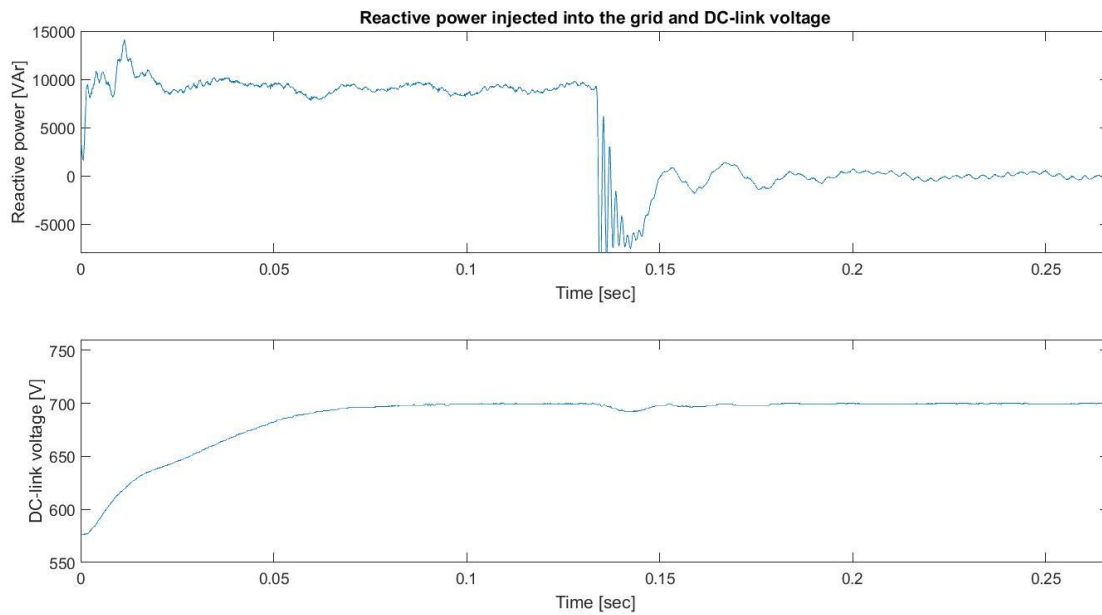


FIGURE 92: TEST OF REACTIVE POWER CONTROLLER FOR THE GRID CONNECTED CONVERTER: REACTIVE POWER (TOP) NEGATIVE 9 KVAR STEP AND DC-LINK VOLTAGE (BOTTOM)

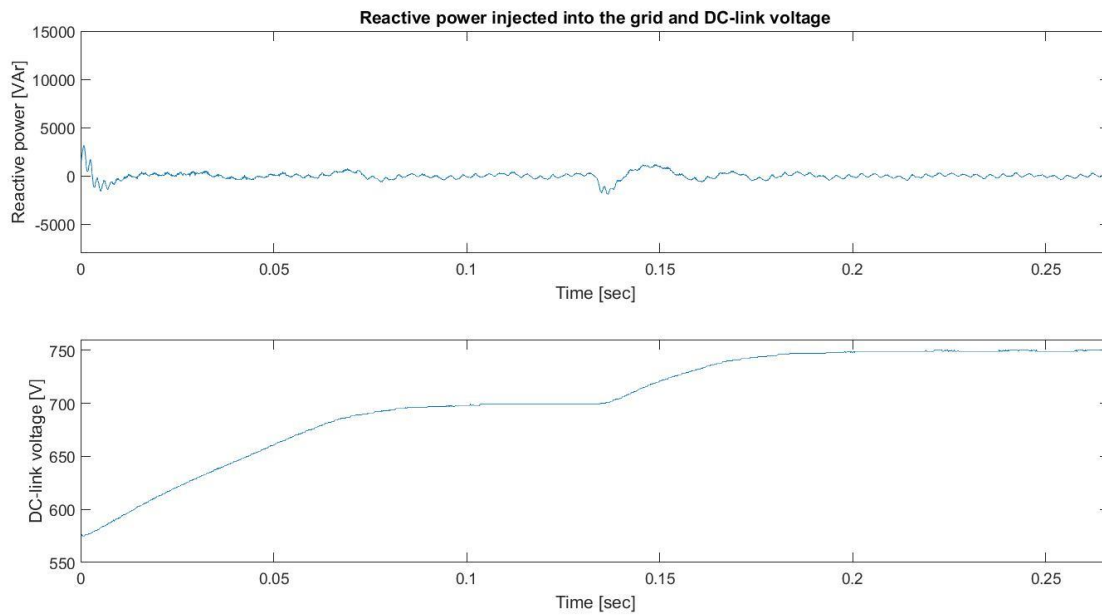


FIGURE 93: TEST OF REACTIVE POWER CONTROLLER FOR THE GRID CONNECTED CONVERTER: REACTIVE POWER (TOP) AND 50V STEP IN THE DC-LINK VOLTAGE (BOTTOM)

As assumed, a step in reactive power will cause a disturbance in the DC-link voltage, due to the fact that the decoupling between the d and q axis is not perfect. A better estimation of the grid impedance would reduce this interference.

The grid current with respect to voltage in the three possible test cases with this setup are presented in Figure 94 to Figure 96. For the case where no reactive power flow is involved, it can be seen that the current is in phase with the voltage, but due to the small amplitude, the quality of the current is affected significantly. For the two other cases, it can be seen that the current has a sinusoidal form but being a bit distorted around the peak values. For the step response it can be observed that the overshoot is rapidly cancelled by the controller. This is affected also by the oscillation in the q component of the voltage.

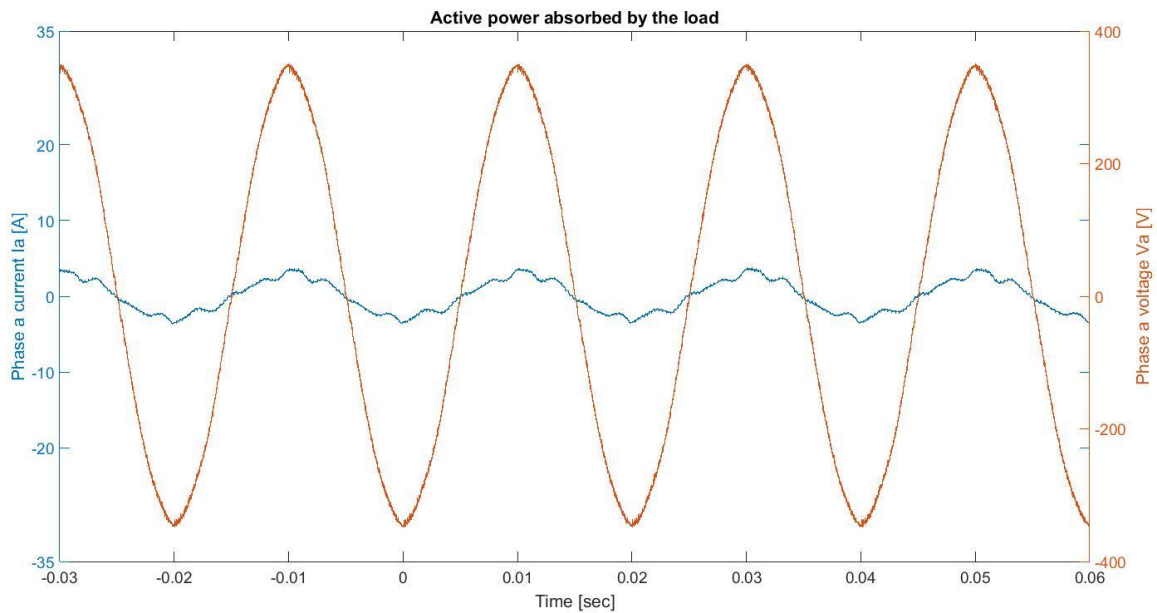


FIGURE 94: TEST OF REACTIVE POWER CONTROLLER FOR THE GRID CONNECTED CONVERTER: NO REACTIVE POWER ABSORBED BY THE CONVERTER

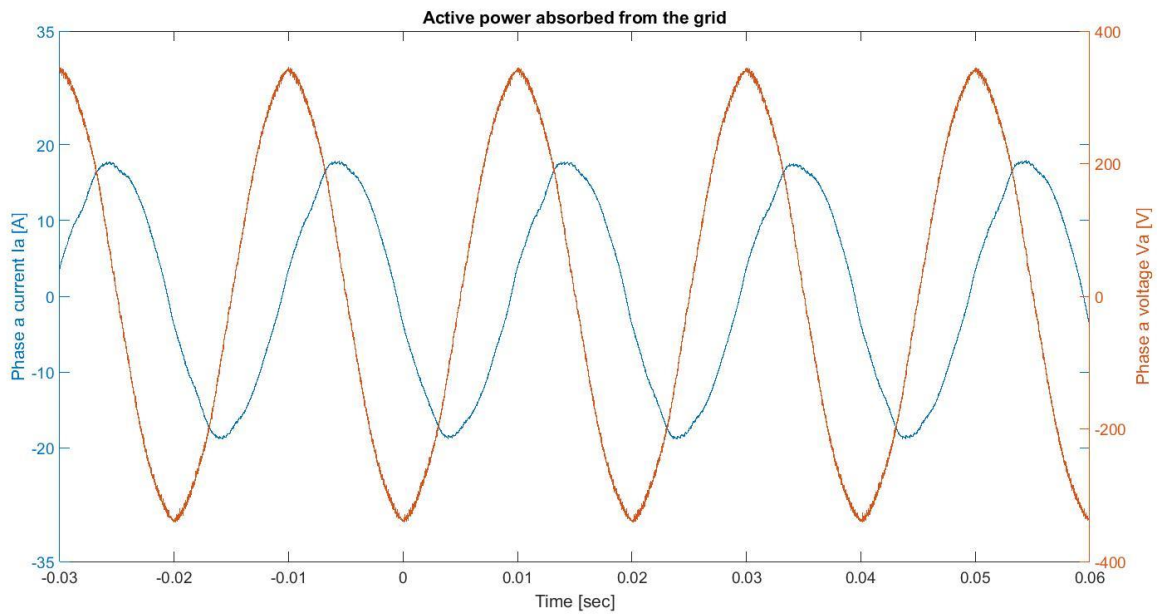


FIGURE 95: TEST OF REACTIVE POWER CONTROLLER FOR THE GRID CONNECTED CONVERTER: 9 KVAR ABSORBED BY THE CONVERTER

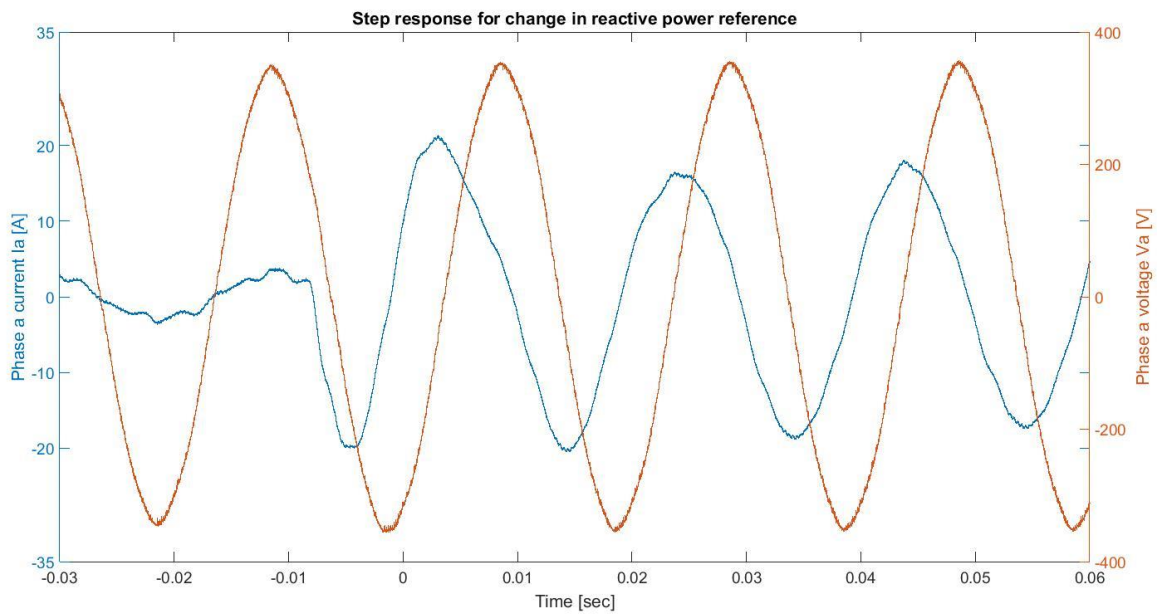


FIGURE 96: TEST OF REACTIVE POWER CONTROLLER FOR THE GRID CONNECTED CONVERTER: 9 KVAR GENERATED BY THE CONVERTER

5.3. DC/DC CONVERTER TESTING

As for the DC-DC converter, this was tested stage by stage like shown in Figure 97, to verify the functionality of all the components. A DC-link voltage of 700V was used. For all test cases 50% duty-cycle was used for driving the transistors, the switching sequence being first T1 and T4 on, followed by all off, T2 and T3 on, and followed by all off. A built prototype can be seen in Appendix A in Figure 110.

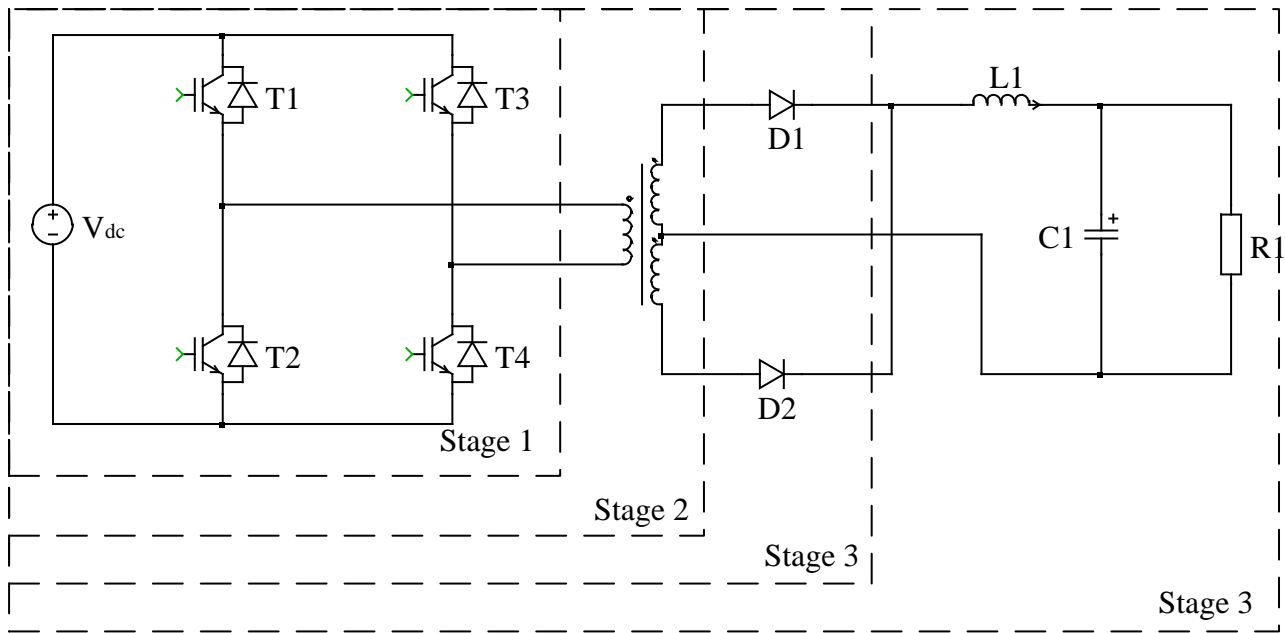


FIGURE 97: TESTING OF THE 10 KW BUILT DC-DC CONVERTER

In the first stage, the load R of 10 ohm was connected directly to the output of the full bridge. As it can be seen, due to the parasitic capacitances of the transistors, during the time when all of the transistors are off the output voltage oscillates. This does not affect the quality of the output voltage of the converter, but it may cause EMI problems. Because the functionality of the converter is not affected, there were no furthermore means taken to cancel the oscillations.

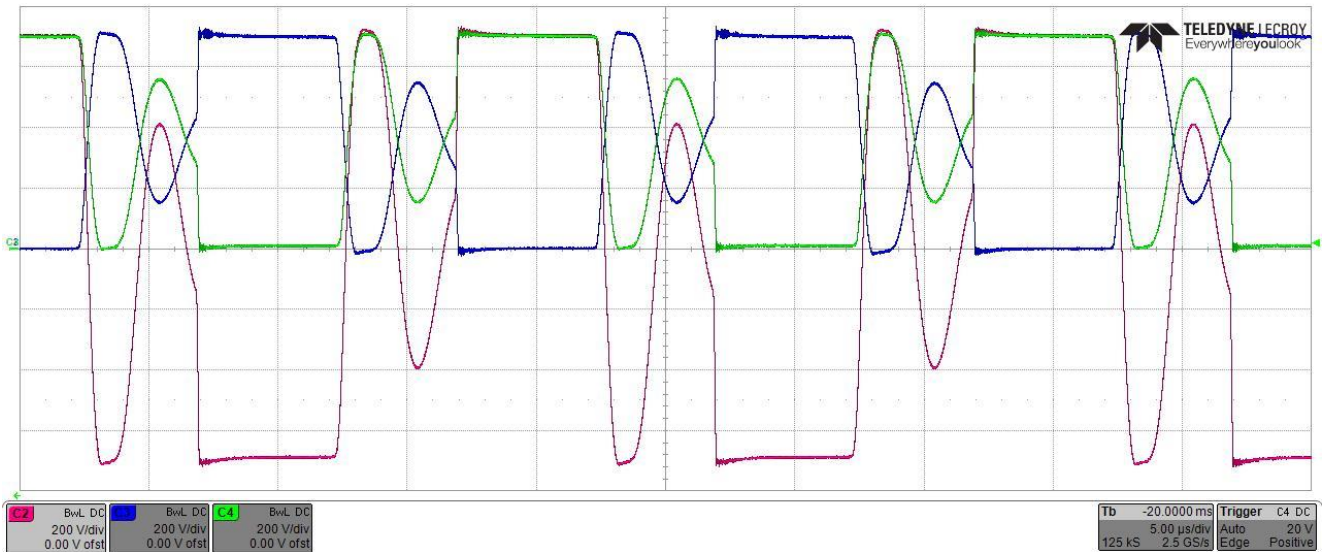


FIGURE 98: STAGE ONE TESTING OF THE DC-DC CONVERTER: OUTPUT VOLTAGE OF THE FULL BRIDGE (RED), OUTPUT VOLTAGE OF RIGHT LEG OF THE CONVERTER (BLUE), OUTPUT VOLTAGE OF LEFT LEG OF THE CONVERTER (GREEN)

During the second stage (see Figure 97) the oscillations increased due to the leakage inductance of the transformer. When the oscillations amplitude becomes greater than the Dc-link voltage, this is clamped to through the diodes. In this way it is ensured that the voltage across the devices does not exceed the DC-link limit and thus the devices are protected from over-voltages. As it can be seen in the waveforms, the voltage in the secondary winding is three times smaller than in the primary side, how it was designed to be.

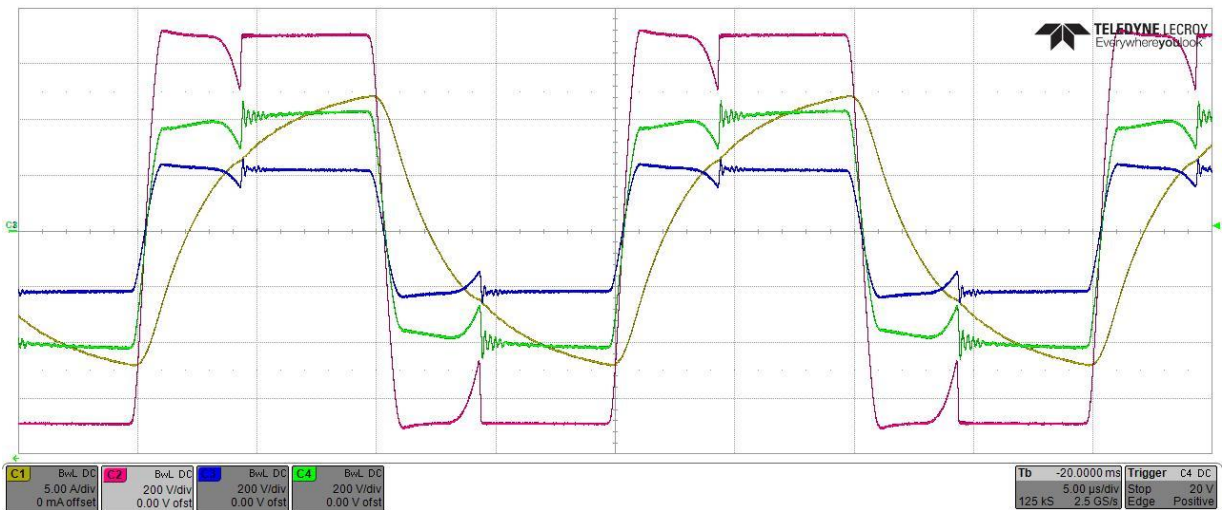


FIGURE 99: STAGE TWO TESTING OF THE DC-DC CONVERTER: LOAD CURRENT (YELLOW), VOLTAGE ON PRIMARY WINDING OF THE TRANSFORMER (RED), TOP SECONDARY OUTPUT VOLTAGE (BLUE), OUTPUT VOLTAGE OF THE TRANSFORMER WITH THE SECONDARIES CONNECTED IN MIDDLE (GREEN)

For the third stage (see Figure 97), when the rectifying diodes are connected a ripple in the output voltage of the transformer is observed. This is due to the parasitic capacitance of the diodes and, as for the oscillations in the primary side it does not affect the output voltage waveform of the converter so it is not acted upon it.

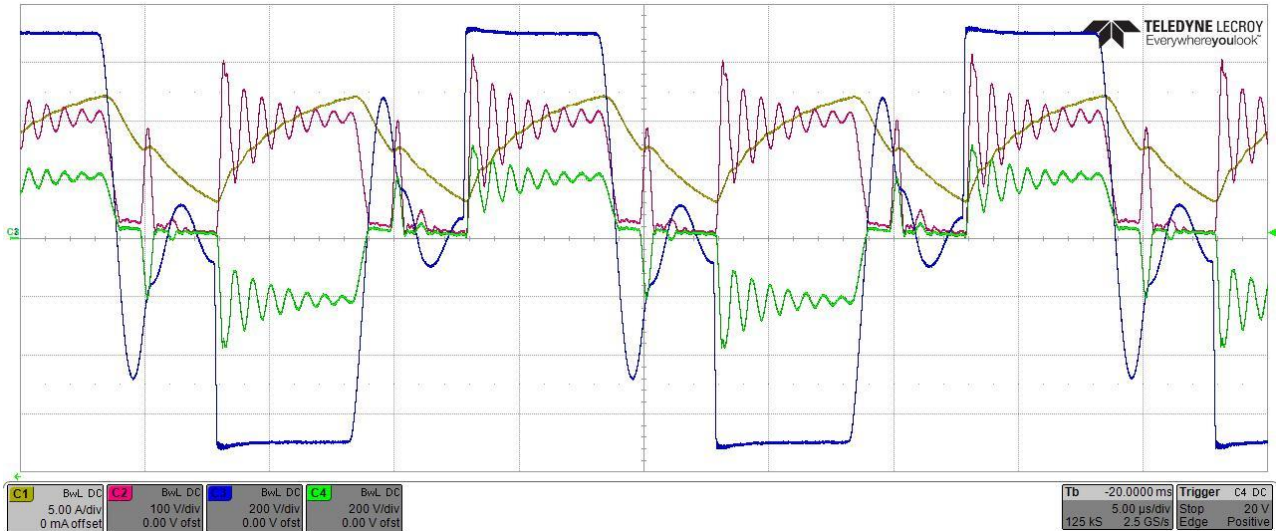


FIGURE 100: STAGE THREE TESTING OF THE DC-DC CONVERTER: LOAD CURRENT (YELLOW), RECTIFIED VOLTAGE (RED), VOLTAGE ON PRIMARY WINDING OF THE TRANSFORMER (BLUE), TOP SECONDARY OUTPUT VOLTAGE (GREEN)

For the last stage (see Figure 97) when all the components are connected it can be observed that the load voltage is constant and the load current is not very much affected by the oscillations presented in the rectified voltage.

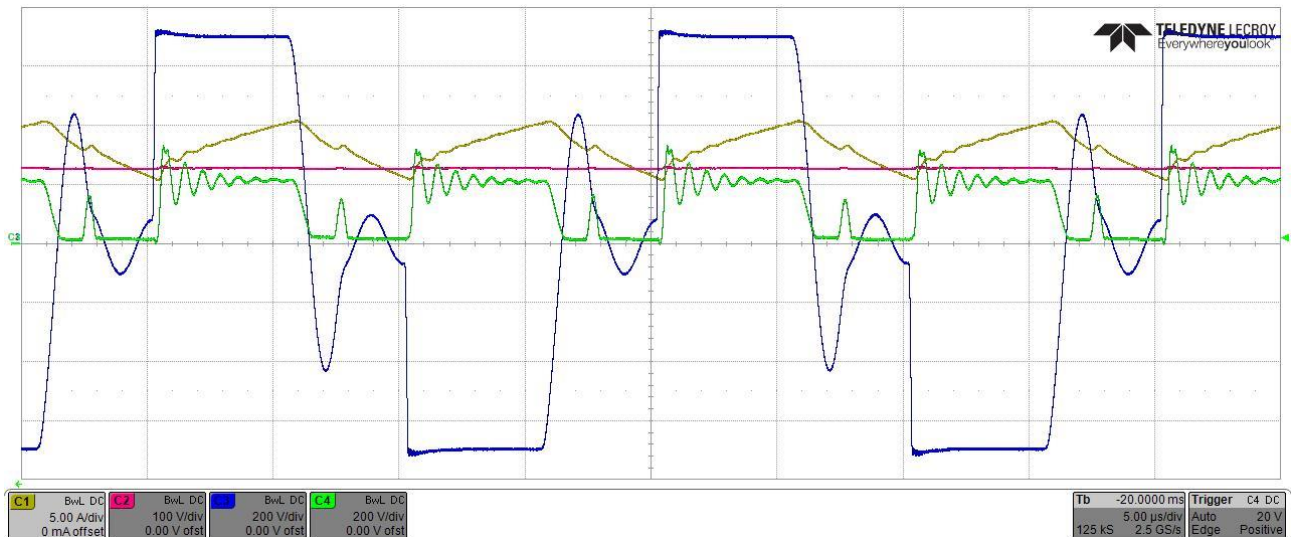


FIGURE 101: STAGE FOUR TESTING OF THE DC-DC CONVERTER: LOAD CURRENT (YELLOW), LOAD VOLTAGE (RED), VOLTAGE ON PRIMARY WINDING OF THE TRANSFORMER (BLUE), RECTIFIED VOLTAGE (GREEN)

After observing that the converter works as expected in open loop, the current controller was implemented. The current is measured twice in each period and an average over the last 20 measurements is taken in order to avoid measurements error. Besides this, an analogic 100 kHz low-pass filter is mounted on the measurement board before the ADC measurement. In this way the current controller frequency is 5 kHz and thus it reduces the response time of the system, compared to the designed PI controller. The response time for the controller is 3 milliseconds, with a small overshoot if the reference is below 10 amps.

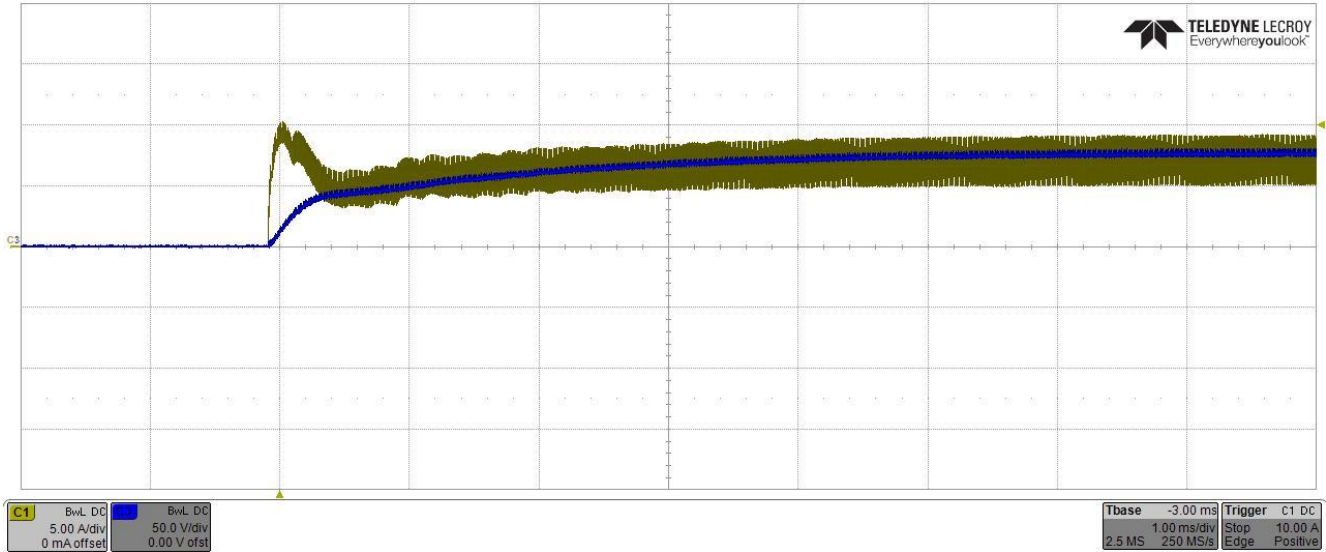


FIGURE 102: TEST OF CURENT CONTROL LOOP FOR THE BUILT DC-DC CONVERTER: STEP RESPONSE TO 7 AMP REFERENCE, INDUCTOR CURRENT (YELLOW), LOAD VOLTAGE (BLUE)

In Figure 102 and Figure 103 it can be seen the positive step response for 7 A respectively 16 A, while in Figure 104 and Figure 105 a negative step response for 16 A to 7 A and from 16 A to 0 A. As it can be observed in both positive and negative steps the response time is less than 3 ms for the current, while the voltage is a bit slower due to the filtering capacitor.

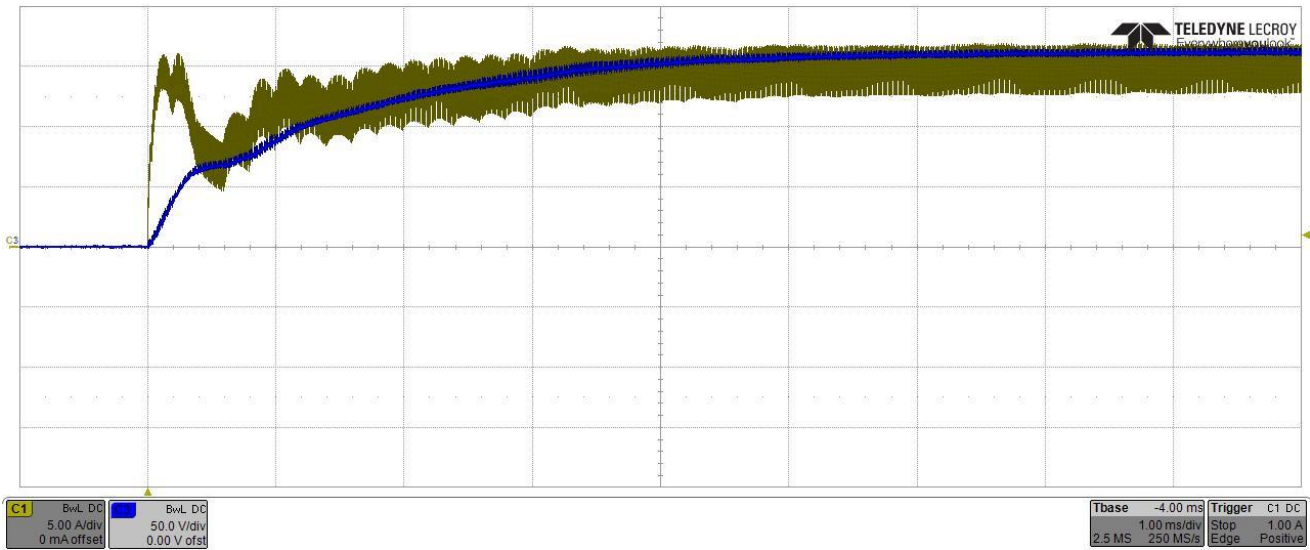


FIGURE 103: TEST OF CURENT CONTROL LOOP FOR THE BUILT DC-DC CONVERTER: STEP RESPONSE TO 16 AMP REFERENCE, INDUCTOR CURRENT (YELLOW), LOAD VOLTAGE (BLUE)

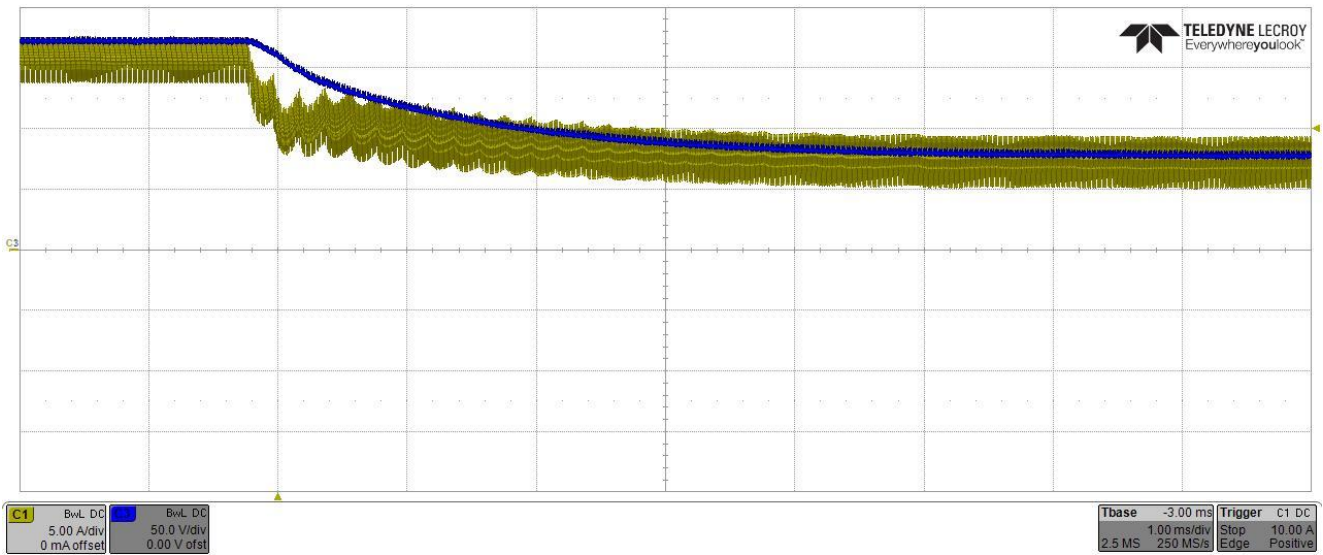


FIGURE 104: TEST OF CURENT CONTROL LOOP FOR THE BUILT DC-DC CONVERTER: STEP RESPONSE TO 16 TO 7 AMP REFERENCE, INDUCTOR CURRENT (YELLOW), LOAD VOLTAGE (BLUE)

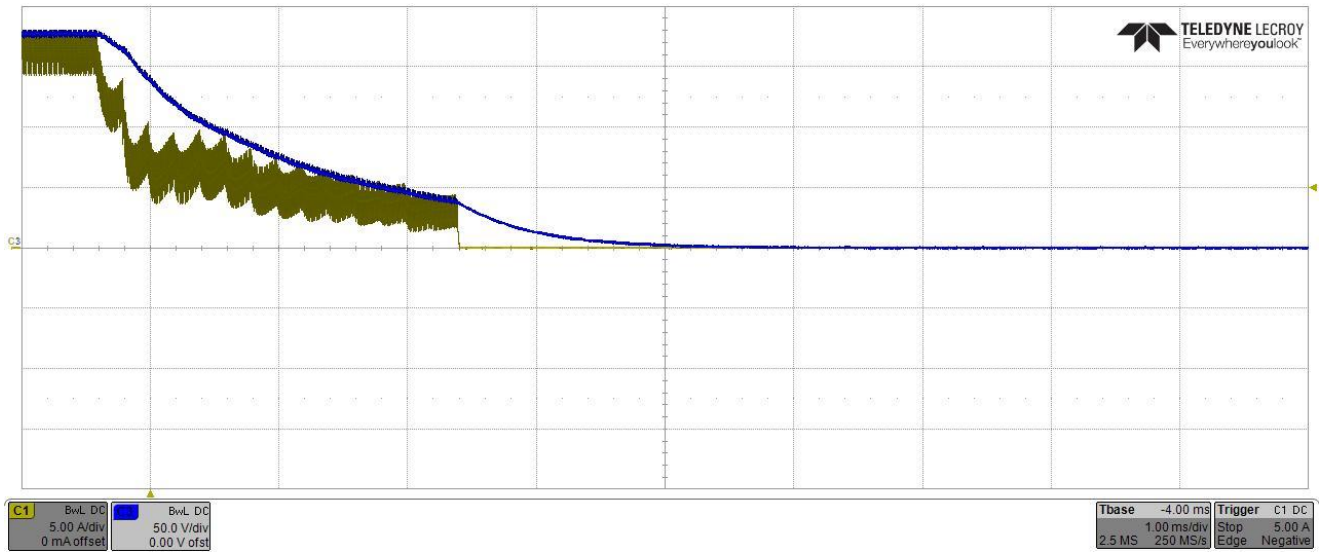


FIGURE 105: TEST OF CURRENT CONTROL LOOP FOR THE BUILT DC-DC CONVERTER: STEP RESPONSE TO 16 TO 0 AMP REFERENCE, INDUCTOR CURRENT (YELLOW), LOAD VOLTAGE (BLUE)

Based on the responses it can be concluded that the current is not affected by the oscillations present in the primary and secondary sides of the transformer, these one only causing EMI noise, which does not interfere with the converter functionality. Also it can be seen that the system is stable and has a very fast step response without having overshoot.

5.4. SYSTEM EXPERIMENTAL RESULTS

For the system functionality test, the grid side AC-DC converter was connected to the DC-DC converter, which was also connected to a resistive load (10 ohm). The results of the measurements can be seen in Figure 106 to Figure 109. Although the grid current is distorted, it can be seen that it is in phase with the voltage maintaining the reactive power to be 0 as this reference was given. The distorted waveform of the current is given by the harmonic current absorbed by the filter, which cannot be fully compensated. As the value of the current increases, the distortion is smaller and it affects less the waveform of the current.

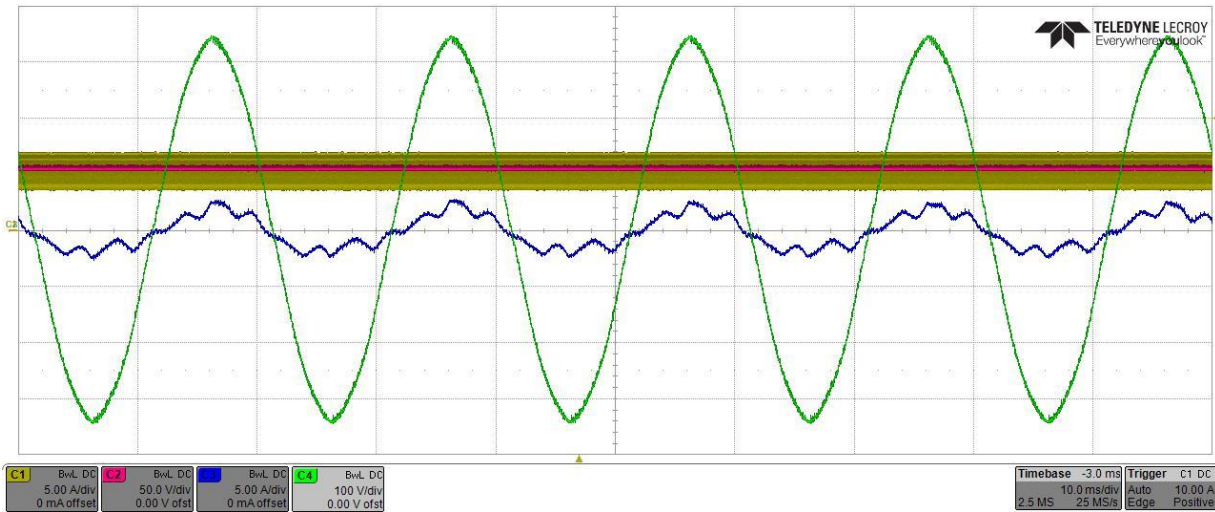


FIGURE 106: SYSTEM FUNCTIONALITY TEST AT 350W LOAD: LOAD CURRENT (YELLOW), LOAD VOLTAGE (RED), GRID PHASE A CURRENT (BLUE) AND GRID PHASE A VOLTAGE (GREEN)

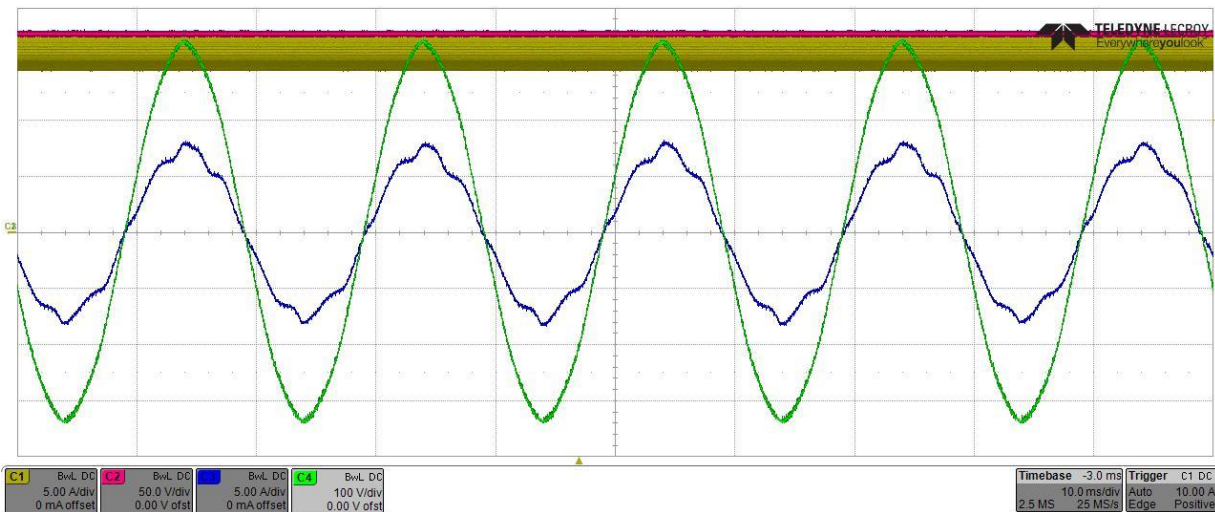


FIGURE 107: SYSTEM FUNCTIONALITY AT 3300W LOAD: LOAD CURRENT (YELLOW), LOAD VOLTAGE (RED), GRID PHASE A CURRENT (BLUE) AND GRID PHASE A VOLTAGE (GREEN)

For the step response it can be seen that interfacing the two converters does not affect their functionality, both responding the same as they did when were tested individually. The DC-link voltage controller for the AC-DC converter (which gives the reference for active current) has a settling time of around 20 ms and a small overshoot which is regulated immediately, and the current controller of the DC-DC converter is much faster, having a response time of 3 ms with no overshoot. The small current that is drawn from the grid when the load current is zero is given by the damping resistors of the LCL filter.

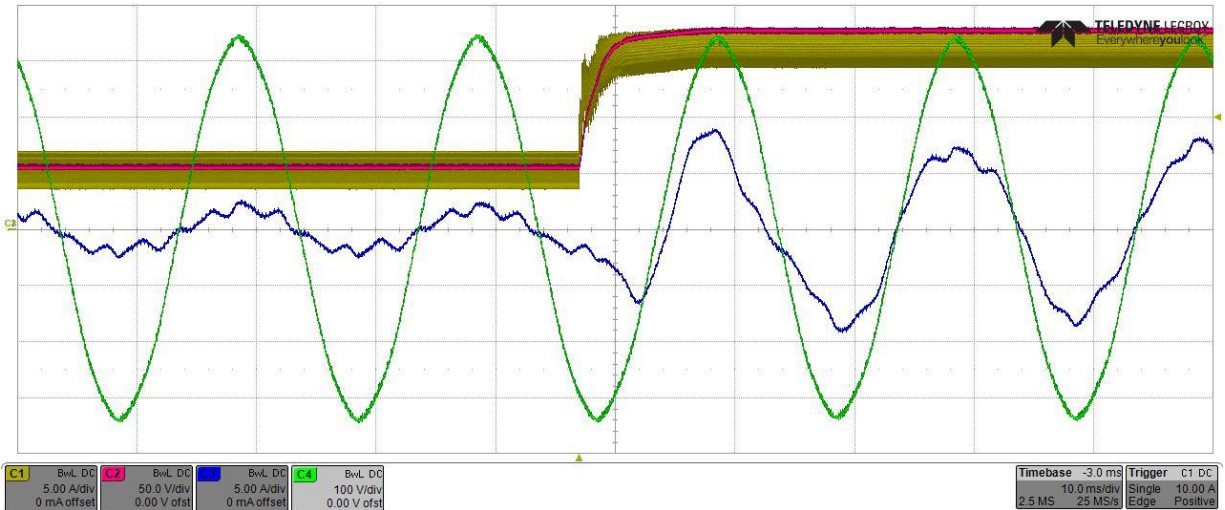


FIGURE 108: SYSTEM STEP RESPONSE FOR A STEP IN LOAD CURRENT FROM 6 TO 16 AMPS: LOAD CURRENT (YELLOW), LOAD VOLTAGE (RED), GRID PHASE A CURRENT (BLUE) AND GRID PHASE A VOLTAGE (GREEN)

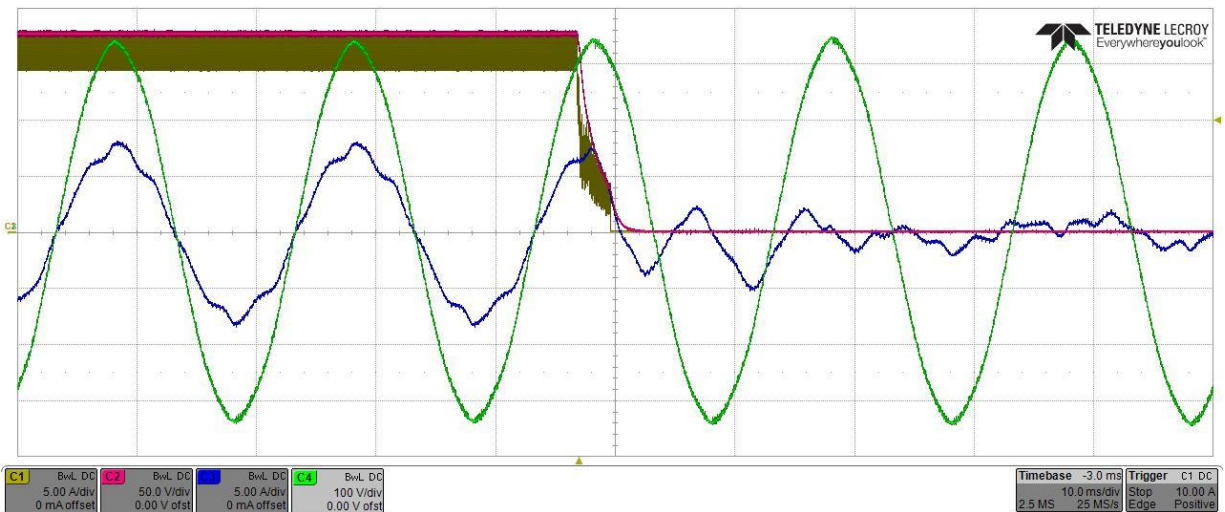


FIGURE 109: SYSTEM STEP RESPONSE FOR A STEP IN LOAD CURRENT FROM 16 TO 0 AMPS: LOAD CURRENT (YELLOW), LOAD VOLTAGE (RED), GRID PHASE A CURRENT (BLUE) AND GRID PHASE A VOLTAGE (GREEN)

5.5. SUMMARY

In this chapter, the results of an experimental setup are presented to validate the simulations done in the previous chapter. Because a physical wind turbine was not available, for the AC side the grid was used. The experimental setup consists in an LCL filter, an active rectifier, and a DC-DC converter with galvanic isolation. In the AC-DC stage only the control was implemented, the hardware being previously developed, but for the DC-DC part everything was designed as mentioned in the previous chapter.

For the AC-DC energy conversion stage, after the scaling of the sensors, the tests were done starting with the PLL, where it has been proven that the converter can synchronize with the grid, only a small oscillation being present most probably due to harmonic content of the grid. After this the current control was presented and the DC-link voltage and reactive power control. As it was mentioned both controller loops respect the requirements, and behave similarly as the model, an oscillation being present in the reactive power controller which could be explained by the grid harmonics content. Also due to harmonics the current drawn by the filter is hard to be compensated which generates a distorted waveform for low amplitude currents. If the current level increases, the harmonic distortion becomes negligible.

For the DC-DC stage, all the converter parts were tested starting with the full bridge inverter, after which the transformer was added, the rectifier and the output filter. After proving the functionality of the converter in open-loop, the current control loop was implemented. The controllers for this one differ from the ones used in simulation due to the filtering of the current, which made the control loop slower. As it can be seen the converter is stable, there is no overshoot and the response time is acceptable. The oscillations of the voltage in the primary and secondary windings of the transformer can cause EMI interference, but do not affect the functionality of the converter.

After the functionality of both converters has been proven, they were connected together, the AC-DC converter having the role of voltage supply for the DC-DC one. As presented, the active rectifier manages to change the active power flow in order to keep the DC-link voltage constant without generating over-currents and without losing the synchronization with the grid.

CHAPTER 6. CONCLUSIONS AND FUTURE WORK

6.1. SUMMARY AND CONCLUSIONS

In the presented thesis a wind powered hydrogen production system has been modeled and analyzed, alongside which a power supply for an electrolysis system is designed. For model verification simulations are done for all the system and also a small scale prototype has been used to validate the simulations of the power electronics stages.

In the beginning of the project multiple topologies are presented for wind turbine, generator, power electronic converters and electrolysis systems. Based on the characteristics for the wind turbine a horizontal axis one was chosen having a PMSG as generator due to its higher efficiency compared to other topologies; for the AC-DC stage a two level active rectifier was chosen in order to be able to fully control the current in the generator and achieve maximum torque per ampere. For the DC-DC converter stage a full bridge connected to a rectifier through a high frequency transformer was used.

After the topologies are selected, the modeling of all the components is presented alongside with the design of the control loops. Simplified models are used for the wind turbine and the generator, but for the power electronics part more complex ones were employed to see also the thermal behavior of the devices. Also in this stage the devices for the DC-DC converter are chosen, based on thermal simulations. A design procedure of the magnetic components is presented here, including the results of the design for the components of a small scale prototype.

With all the components modeled, simulations were employed to verify the models and the controller designs. The simulations were divided into two separate parts, one consisting of wind turbine, generator and AC-DC converter; the second one consisting of the DC-DC converter and electrolysis system. The designed controllers proved to function well and operate according to the design requirements.

For the experimental prototype the tests were done step by step. Instead of using a wind turbine the grid was used for the AC side, and on the DC-DC side a small scale 10 kW prototype is used due to the power limitations of the laboratory. The prototype demonstrated the functionality of the converter, but the final efficiency could not be validated due to the fact that the transformer and the inductor were only made to validate the topology, and were not optimized for losses. Although an efficiency of 91% for the DC-DC converter was measured, it was observed by the heat dissipated that the majority of the losses were present in the inductor and transformer core.

Given the results, the presented system would be a high efficiency hydrogen production system from a wind turbine source. The converters proved to work as specified in the requirements (except the speed controller for the generator which had a higher overshoot than expected) and the prototype built

validated the functionality of such a system. For the current controllers used in the prototype testing, a response time of approx. 3 ms was obtained for AC-DC and DC-DC converters, having an overshoot of less than 10%; the proposed reactive power controllers has a 20 ms response time with an overshoot of 20% during first period; the proposed DC-link voltage controller has a response time of approx. 35 ms and it has no overshoot. Based on the results it can be concluded that all the requirements were met for the prototype regarding the control strategy, the efficiency being evaluated after the full scale DC-DC converter is built. Also, due to the fact that SiC devices were used for the DC-DC converter, high frequency operation has been achieved. In this way the magnetic components were reduced in size without affecting the overall efficiency of the converter.

6.2. FUTURE WORK

For further study the load will be changed in order to be able to test the DC-DC converter at a power up till 10 kW which is the limit in the laboratory. After small scale tests are done, the transformer and an inductor for full scale converter will be built for one DC-DC converter in order to test it at nominal power. Testing the converter at full power will make it possible to evaluate the efficiency and make modifications if needed in the design. For this stage, the tests shall be performed in a different place where it is possible to draw from the grid 85 kW.

Based on the results of the full scale converter, another two will be built and interleaved so full 250 kW desired power is obtained and it will be tested using the electrolysis stack as load. Based on the responses of the converters, the controller parameters might be slightly tuned so best performance is achieved.

As for the AC-DC part, a way to reduce the oscillations in the reactive power will be investigated, one way being eliminating the oscillations in the q-component of the voltage under distorted grid voltages.

APPENDIXES

APPENDIX A DC-DC CONVERTER TEST SETUP

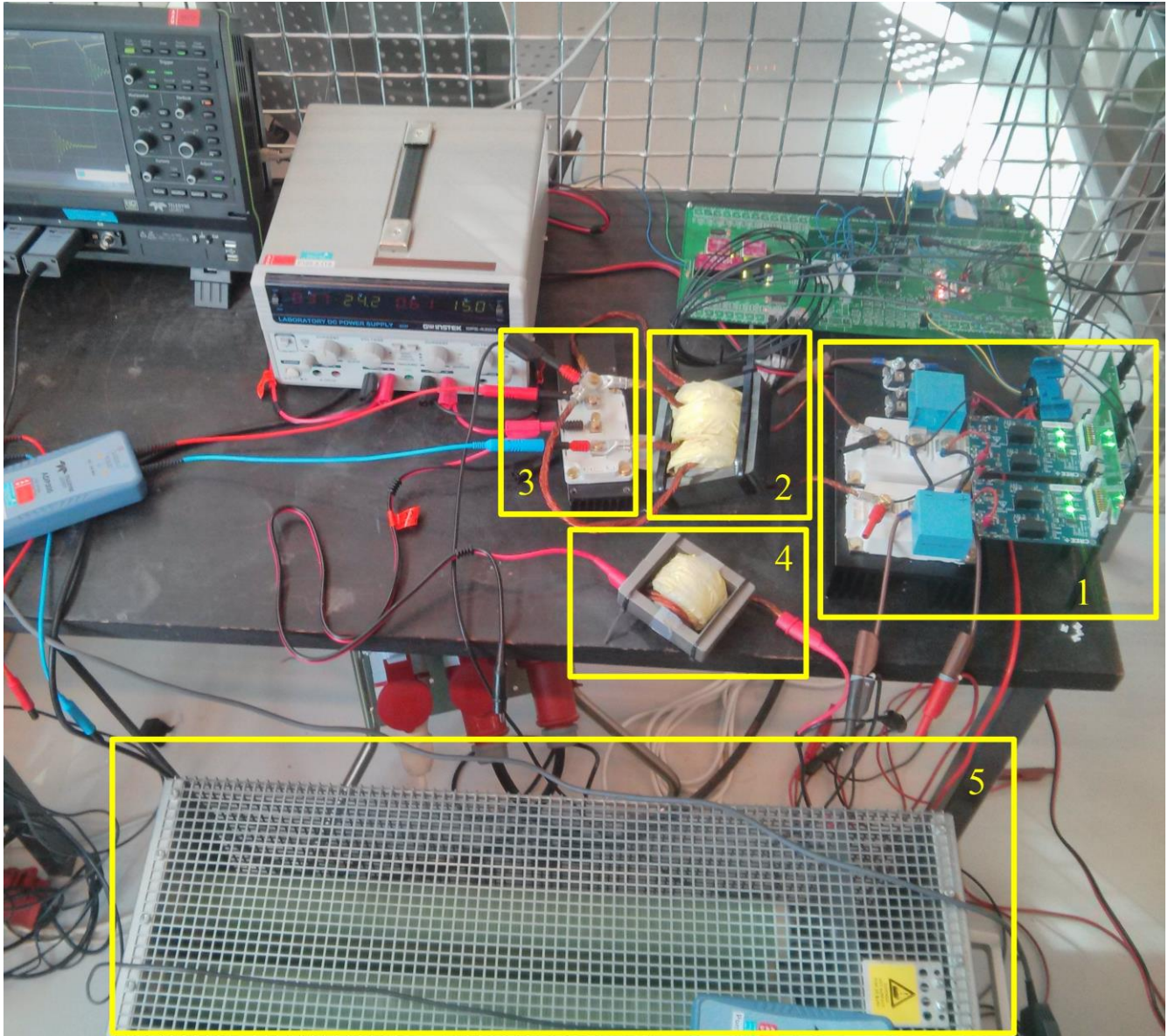


FIGURE 110: DC-DC CONVERTER PROTOTYPE TEST: FULL BRIDGE CONVERTER (1), HIGH FREQUENCY TRANSFORMER (2), RECTIFIER (3), INDUCTOR (4), LOAD RESISTOR (5)

APPENDIX B AC-DC CONVERTER IMPLEMENTED CONTROL STRATEGY

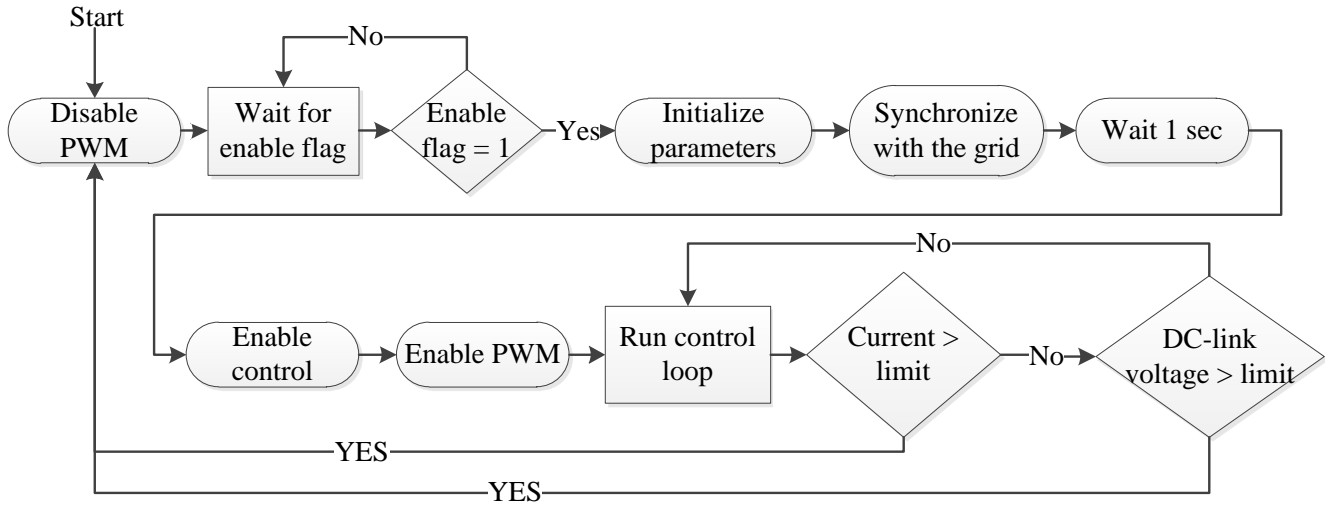


FIGURE 111: BLOCK DIAGRAM OF CONTROL STRATEGY IMPLEMENTED IN THE DSP OF THE GRID CONNECTED AC-DC CONVERTER

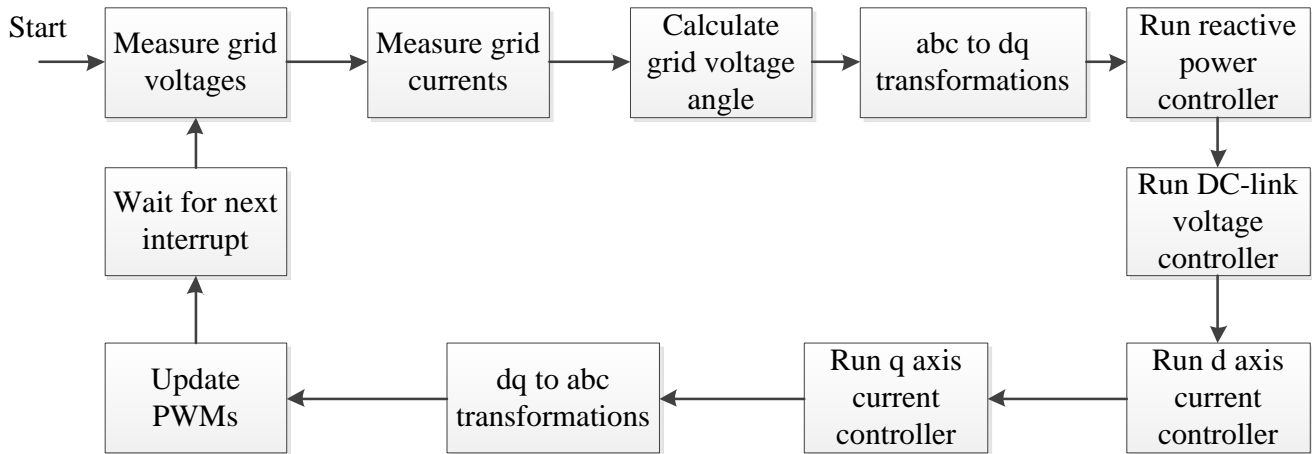


FIGURE 112: BLOCK DIAGRAM FOR CONTROL LOOP FOR THE GRID CONNECTED AC-DC CONVERTER (CONTROL LOOP BLOCK FROM FIGURE 111)

BIBLIOGRAPHY

- [1] T. E. W. E. Association, "Wind energy scenarios for 2030," <http://www.ewea.org/fileadmin/files/library/publications/reports/EWEA-Wind-energy-scenarios-2030.pdf>, 2015.
- [2] T. E. W. E. Association, "Wind in power - 2014 European Statistics," <http://www.ewea.org/fileadmin/files/library/publications/statistics/EWEA-Annual-Statistics-2014.pdf>, 2015.
- [3] A. Ozarslan, "Large-scale hydrogen energy storage in salt caverns," *International journal of hydrogen energy*, vol. 37, pp. 14265-14277, 2012.
- [4] G. Mikhail, D. Ibrahim and A. R. Marc, "Greenhouse gas emissions reduction by use of wind and solar energies for hydrogen and electricity production: Economic factors," *International Journal of Hydrogen Energy*, vol. 32, no. 8, pp. 927-931, 2007.
- [5] N. Mendis, S. Sayeef, K. Muttaqi and S. Perera, "Hydrogen energy storage for a permanent magnet wind turbine generator based autonomous hybrid power system," *Power and Energy Society General Meeting, IEEE, San Diego*, pp. 1-7, 2011.
- [6] K. Koiwa, A. Umemura, R. Takahashi and J. Tamura, "Stand-alone hydrogen production system composed of wind generators and electrolyzer," *Proceedings of Industrial Electronics Society, IECON*, pp. 1873 - 1879, 2013.
- [7] "Raul Sarrias-Mena; Luis M. Fernandez-Ramirez; Carlos Andres Garcia-Vazquez; Francisco Jurado," *International journal of hydrogen energy*, pp. 2927-2938, 2015.
- [8] D. Rekioua, *Wind power electric systems. Modeling, Simulation and control*, London, ISBN 978-1-4471-6424-1: Springer, 2014.
- [9] F. Blaabjerg, M. Liserre and K. Ma, "Power Electronics Converters for Wind Turbine Systems," *IEEE TRANSACTIONS ON INDUSTRY APPLICATIONS*, vol. 48, no. 2, pp. 708-719, 2012.
- [10] D. Vinnikov, H. Hõimoja, A. Andrijanovič, I. Roasto, T. Lehtla and M. Klytta, "An Improved Interface Converter for a Medium-Power Wind-Hydrogen System," *International Conference on Clean Electrical Power*, pp. 426 - 432, 2009.
- [11] M. E. Sahin, H. I. Okumus and M. T. Aydemir, "Implementation of an electrolysis system with DC/DC synchronous buck converter," *International journal of hydrogen energy*, no. 39, pp. 6802-6812, 2014.
- [12] I.-O. Lee, S.-Y. Cho and G.-W. Moon, "Interleaved Buck Converter Having Low Switching Losses and Improved Step-Down Conversion Ratio," *IEEE Transactions on Power Electronics*, vol. 27, no. 8, pp.

3664-3675, 2012.

- [13] N. Mohan, T. M. Undeland and W. P. Robbins, *Power electronics. Converters, Applications and Design* second edition, John Wiley & Sons, Inc., 1995.
- [14] N. Mohan, *First course on power electronics and drives*, Minneapolis: MNPERE ISBN 0-9715292-2-1, 2003.
- [15] Y. Errami, M. Maaroufi and M. Ouassaid, "Modelling and control strategy of PMSG based variable speed wind energy conversion system," *International Conference on Multimedia Computing and Systems (ICMCS)*, pp. 1-6, 2011.
- [16] J. Liang and B. Whitby, "Field Oriented Control of a Permanent Magnet Synchronous Generator for use in a Variable Speed Tidal Stream Turbine," *Proceedings of UPEC · 46th International Universities Power Engineering Conference*, pp. 1-6, 2011.
- [17] M. Ni, D. Y. Leung and M. K. Leung, "A review on reforming bio-ethanol for hydrogen production," *International Journal of Hydrogen Energy*, vol. 32, p. 3238 – 3247, 2007.
- [18] M. Carmo, D. L. Fritz, J. Mergel and D. Stolten, "A comprehensive review on PEM water electrolysis," *International journal of hydrogen energy*, vol. 38, pp. 4091-4934, 2013.
- [19] Z. Wang, K. Lu and F. Blaabjerg, "A Simple Startup Strategy Based on Current Regulation for Back-EMF-Based Sensorless Control of PMSM," *Power Electronics, IEEE Transactions on power electronics*, vol. 27, no. 8, pp. 3817 - 3825, 2012.
- [20] D. Zhou, F. Blaabjerg, T. Franke, M. Tønnes and M. Lau, "Comparison of Wind Power Converter Reliability With Low-Speed and Medium-Speed Permanent-Magnet Synchronous Generators," *IEEE Transactions on Industrial Electronics*, vol. 62, no. 10, pp. 6575-6584, 2015.
- [21] I. Trintis, "Grid Converters for Stationary Battery Energy Storage Systems, PhD. Thesis," Department of Energy Technology, Aalborg University, 2011.
- [22] R. Teodorescu, M. Lissere and P. Rodriguez, *Converters for Photovoltaic and Wind Power Systems*, Ltd. ISBN: 978-0-470-05751-3: Wiley, 2011.
- [23] R. W. Erickson and D. Maksimovic, *Fundamentals of Power electronics*, second edition, New York: Kluwer Academic/Plenum Publishers, 2004.
- [24] R. Sarrias-Mena, L. M. Fernandez-Ramirez, C. A. Garcia-Vazquez and F. Jurado, "Electrolyzer models for hydrogen production from wind energy systems," *International journal of hydrogen energy*, vol. 40, no. 7, pp. 2927-2938, 2015.
- [25] W. T. McLyman, *Transformer and Inductor Design Handbook*, Third Edition, Revised and Expanded, Idyllwild, California: Marcel Dekker, Inc., 2004.

- [26] L. Mathe, F. Iov, D. Sera, L. Torok and R. Teodorescu, "Implementation of PLL and FLL trackers for signals with high harmonic content and low sampling frequency," *Proceedings of International Conference on Optimization of Electrical and Electronic Equipment (OPTIM)*, pp. 633 - 638, 2014.
- [27] T. Instruments, "Webench Design Center," Texas Instruments, 2016. [Online]. Available: http://www.ti.com/lstds/ti/analog/webench/overview.page?DCMP=analog_power_mr&HQS=webench-pr.
- [28] M. Liserre, F. Blaabjerg and S. Hansen, "Design and Control of an LCL-Filter-Based Three-Phase Active Rectifier," *IEEE TRANSACTIONS ON INDUSTRY APPLICATIONS*, vol. 41, no. 5, pp. 1281-1291, 2005.